The Pennsylvania State University

The Graduate School

Department of Mechanical Engineering

THERMO-ELASTO-VISCO-PLASTIC MODELLING OF

FRICTION STIR WELDING IN AN EULERIAN REFERENCE

FRAME

A Dissertation in

Mechanical Engineering

by

Xiaoliang Qin

Submitted in Partial Fulfillment
of the Requirements
for the Degree of

Doctor of Philosophy

May 2009

The dissertation of Xiaoliang Qin was reviewed and approved* by the following:

Panagiotis Michaleris
Associate Professor of Mechanical Engineering
Dissertation Advisor
Chair of Committee

Ashok D. Belegundu
Professor of Mechanical Engineering

Francesco Costanzo
Associate Professor of Engineering Science and Mechanics

Eric Mockensturm
Associate Professor of Mechanical Engineering

Karen A. Thole
Professor of Mechanical Engineering
Head of the Department of Mechanical Engineering

*Signatures are on file in the Graduate School.

Abstract

Two sets of stabilized, Galerkin finite element formulations for modeling elasto-visco-plastic material response of quasi-steady state processes in Eulerian frames are presented. One set is based on the rate equilibrium equation, and the other set is based on the true equilibrium equation. The rate equilibrium formulation couples the velocity ($\mathbf{V}$), stress ($\boldsymbol{\sigma}$), deformation gradient ($\mathbf{F}$) and internal variable ($\mathbf{s}$) together. While, the true equilibrium formulation solves the velocity ($\mathbf{V}$), deformation gradient ($\mathbf{F}$), viscoplastic part of deformation gradient ($\mathbf{F}^{vp}$) and internal variable ($\mathbf{s}$) simultaneously. The streamline upwind Petrov-Galerkin (SUPG) method is introduced to eliminate spurious oscillations which may be caused by the convection of stress, deformation gradient, viscoplastic deformation gradient and internal variable evolution. A progressively stiffening solution strategy is proposed to improve the convergence of the Newton-Raphson solution procedure. These formulations have been implemented in a 4 node quadrilateral element. Three numerical examples (radial flow, strip drawing and gas metal arc welding) have been modeled to verify the accuracy of these Eulerian methods.

A coupled 2-dimensional Eulerian thermo-elasto-visco-plastic model has been developed for modeling the Friction Stir Welding process. First, a coupled thermo-visco-plastic analysis is performed to determine the temperature distribution in the full domain and the incompressible material flow around the spinning tool. Next, an elasto-visco-plastic analysis based on the true equilibrium is performed outside the visco-plastic region to comput the residual stress. Both frictional heat and plastic deformation heat generation are considered in the model. Furthermore, this is the only known model computing residual stress accounting for plasticity caused by both thermal expansion and mechanical deformation due to material spinning. The computed residual stress is verified by comparing to experimentally measured data.

Table of Contents

List of Tables

List of Figures

Acknowledgments

Chapter 1

Introduction

Friction stir welding (FSW) is a novel solid-state welding technology invented in 1991 by The Welding Institute (TWI) in the United Kingdom. It represents one of the most significant developments in joining technology over the last half century. A schematic of a FSW operation for joining two flat plates is shown in Figure 1.1.
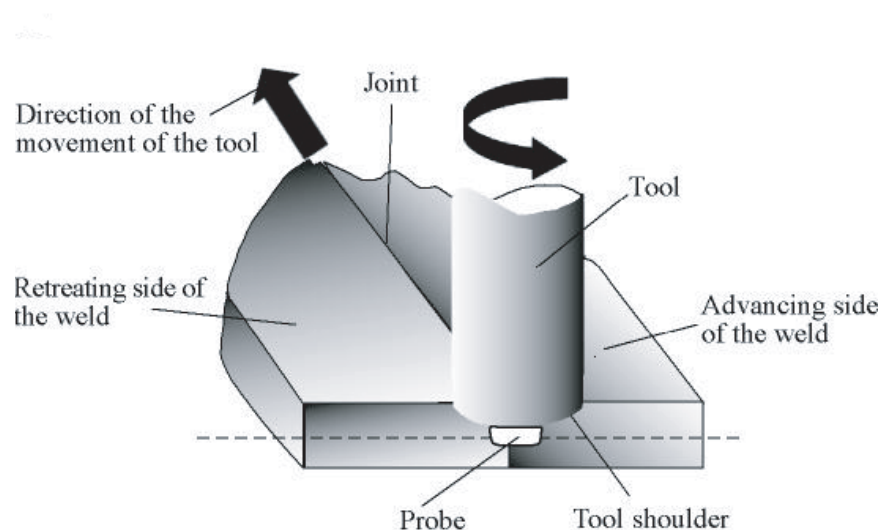
Fig. 1.1. A schematic of friction stir welding operation

In friction stir welding, the parts to be jointed are aligned and clamped together. A non-consumable fast spinning welding tool is plunged into the joint line and traversed along the joint. Heat, which softens the material, comes from two sources: (1) friction between the tool and parts, and (2) heat generated by the plastic deformation of the parts. By the spinning effect of the rotating pin, the plasticized material flows from the leading edge of the tool to the trailing edge, which creates a solid state weld between the two pieces.

Friction stir welding makes high-strength joints of some aerospace aluminum alloys, which are non-weldable for traditional welding technology, possible. Since no flux and filler metal are used in friction stir welding, the process is environmentally friendly. FSW is also reported to provide significant reduction in residual stress over conventional welding technology. Because of its advantages, several successful applications of FSW have been developed in the relatively short period after invention.

Because complicated temperature increase, plastic deformation, material flow and microstructural evolution are involved in FSW, understanding of thermal and mechanical processes during FSW is necessary for the improving quality of welds. Both experimental and numerical investigations have been carried out to explain this new technology, especially on: temperature distribution, material flow around the tool pin and residual stress.

1.1   Experimental investigations

Since the temperature distribution of FSW influences the distribution of residual stress and the microstructure of the welds, it is important to study the temperature

distribution during FSW. However, temperature measurements around the rotating tool pin are very difficult due to the translation of the tool. Thus the temperature within the stir zone during FSW can only be estimated by the microstructure of the weld [1] or recorded by embedding thermocouples. Using thermocouples in the welding region, Tang *et al.* [2] measured the heat input and temperature distribution within friction stir welding, and concluded that: (1) the peak temperature is recorded at the weld center line, and (2) temperature gradient within the stirzone is relatively small.

How the material flows from the leading edge of the tool pin to the trailing edge is still a mystery. This has led to numerous investigations of the material flow during FSW. Reynolds *et al.* [3] investigated the material flow pattern by inserting markers into the plates to be welded. Guerra *et al.* [4] and Colligan [5] studied the material movement by the tracer technique and the "stop action" technique.

The existence of high value of residual stress has a significant effect on the postweld mechanical properties. Therefor, it is of practical importance to investigate the residual stress of friction stir welding. Some recent work measured the residual stress in friction stir welded plates [6, 7, 8, 9, 10]. In general, it is expected that the residual stress in a FSW welded plate is lower than in a plate welded by traditional welding technology, because the highest temperature in FSW is lower. However, recent publications indicate the residual stress in FSW may be comparable to those of Gas Metal Arc Welding [11, 12].

1.2 Numerical Simulation

Because of the limitation of experimental measurements, numerical simulations have been carried out to model FSW. The finite element method has been successfully

implemented to model history dependent problems such as forming, welding, rolling and extrusion for nearly thirty years [13, 14, 15, 16, 17, 18, 19, 20, 21, 22].

With the exception of the work of Brown *et al.* [23], most investigators assume that the deformation has very small effect on the temperature distribution during welding process. Therefore a heat transfer analysis is performed first, followed by a mechanical analysis using the temperature results as a thermal loading. When simulating thermal and mechanical process of welding, two approaches are usually used: Lagrangian and Eulerian, as shown in Figure 1.2.

In Lagrangian analysis, the reference frame is fixed with the material and the welding tool moves in time. Time increment Lagrangian formulations with elasto-plastic constitutive law are algorithmically easy to implement and have been shown to be robust for many applications. However, this method may become computationally demanding in 3D models when several thousand time increments are needed such as in the case of laser or arc welding of large structures [24].

Nguyen et al. [25] showed that the welding process can be treated as a quasi-steady state process in an Eulerian frame, with reference frame located in a fixed spacial point, such as the welding tool, as shown in the case B in Figure 1.2. In Eulerian analysis, the material status is solved over a fixed spacial domain, as it enters form the inlet surface and exits through the outlet surface. Since the Eulerian analysis is a steady steady analysis, models can be solved at once. Thus it has potential to reduce computational cost in modelling welding process, as compared to the time incremental Lagrangian analysis.
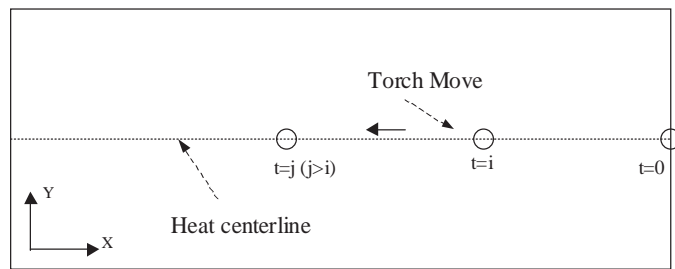
A. Lagrangian Frame
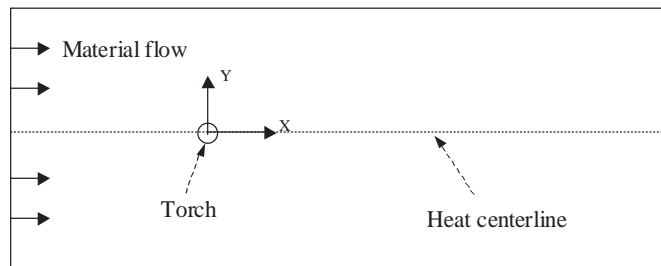
B. Eulerain Frame

Fig. 1.2.   Lagrangian and Eulerian Reference Frame

An Eulerian analysis is more advantageous in modelling material movement in FSW, since it does not need to consider mesh distortion and re-meshing which are issues encountered in Lagrangian analysis. Due to the difficulty of dealing with mesh distortion and developing Eulerian method, most investigators using a Lagrangian modeling approach ignore the material flow and instead assume that residual stress and distortion in FSW are caused by thermal expansion only [26, 27, 28, 29, 12, 30]. The temperature distribution is provided by either a pure conduction analysis using a distributed heat input model [26, 27, 28, 29, 12, 30] or a thermal transport analysis [31] which may account for the effect of material flow on temperature distribution. The limitations are: (1) they omit the heat generated by plastic deformation of the material which may lower the peak temperature, and (2) they neglect the contribution of spinning material flow in the residual stress formation which produces an unsymmetric residual stress distribution [11, 12].

To predict residual stress, it is necessary to compute the deformation history of each particle in order to determine stress and strain. This can be accomplished by either computing the streamline of each particle [32] or by computing material evolution in a weak FEA (mixed) formulation [32, 33, 34]. The streamline integration methods for elasto-plastic or elaso-visco-plastic models do not allow for the computation of global algorithmic tangent stiffness leading to convergence difficulties, while the mixed FEA formulations lead to systems with large number of degrees of freedom. Due to these modeling difficulties most investigators neglect history evolution in Eulerian models by assuming visco-plastic material response [33]. Such material models may be sufficient

at the high temperatures near the stirring zone. However, they are not appropriate for lower temperatures and result into zero residual stress distortion.

In this work, two Eulerian elasto-viscoplastic formulations are presented to simulate FSW and predict residual stress.

1.2.1 Rate equilibrium Eulerian formulation

A four-field (velocity $\mathbf{V}$, stress $\boldsymbol{\sigma}$, deformation gradient $\mathbf{F}$ and internal variable $\mathbf{s}$) rate-dependent Eulerian formulation based on the rate of equilibrium equation [35] is proposed to predict residual stresses. Elasto-plastic formulations using displacement as a primary variable have been proposed in Reference [36]. The approach is applicable to rate independent problems and is capable of computing residual stress. However, the method exhibits convergence difficulties due to the abrupt transition of elastic to plastic response. Therefore, the Anand's [37] rate dependent constitutive law, with smooth transition from elastic stage to plastic stage, is introduced to improve convergence. The deformation gradient is integrated throughout the analysis domain to determine stress and strain. The material and deformation gradient evolution partial differential equations have convection terms which may result in nonphysical oscillations in the solution. The streamline Upwind Petrov-Galerkin (SUPG) method with an additional mesh-dependent term in the weighting function [38, 39, 40, 41] is used to stabilize these equations.

Three 2-D numerical models with 4-node quadrilateral elements have been implemented to show the validity and accuracy of the rate equilibrium Eulerian formulation.

1.2.2   True equilibrium Eulerian formulation

Although the formulation based on the rate equilibrium equation is easy to implement, it can not account for the temperature variation of Young's modules and thermal enpension. Also the application of traction rate boundary condition is complicated. Thus, a mixed Eulerian formulation based directly on the true equilibrium equation is developed. In this formulation, velocity ($\mathbf{V}$), total deformation gradient ($\mathbf{F}$), viscoplastic part of deformation gradient ($\mathbf{F}^{vp}$) and internal variable ($\mathbf{s}$) are solved simultaneously. The streamline Upwind Petrov-Galerkin (SUPG) method is also employed to stabilize the evolution equation of total deformation gradient, viscoplastic part of deformation gradient and internal variable. The true equilibrium Eulerian formulation has been implemented in a 2D reference frame and has been verified by comparing Lagrangian elasto-plastic and Eulerian elasto-visco-plastic results in arc welding.

1.2.3   Simulation of FSW

In the present work, a coupled thermo-elasto-viscoplastic Eulerian model is developed to model friction stir welding and predict residual stress. The model accounts for plasticity caused by both thermal expansion and mechanical deformation due to material spinning. Because the temperature of the material near the tool pin is close to its melting temperature, the material in this region can be treated as an incompressible visco-plastic flow. Thus, a coupled thermo-visco-plastic analysis is performed in this region to predict temperature distribution over the analysis domain and material flow around the tool pin. In the region outside the tool shoulder, the material response is

treated as elasto-visco-plastic and is modeled by the Anand's constitutive law. The thermal and velocity boundary conditions for the elasto-visco-plastic analysis are obtained from the previous coupled thermo-visco-plastic analysis. The true equilibrium Eulerian elasto-visco-plastic formulation [42] is used in this work to predict the residual stress of FSW.

1.3 Dissertation Layout

The following dissertation consists of four main chapters. Chapter 2 describes the rate equilibrium based Elasto-visco-plastic mixed Eulerian formulation. Chapter 3 verifies the rate equilibrium Eulerian formulation and Anand's constitutive law by comparing the results with Lagrangian elasto-plastic analysis results in gas metal arc welding. Chapter 4 presents the true equilibrium based Elasto-visco-plastic Eulerian formulation. In chapter 5, a coupled thermo-elasto-viscoplastic Eulrian friction stir welding model is present and implemented to model the temperature distribution, material flow and residual stress of FSW. Finally, chapter 6 outlines the results achieved in this research and concludes this thesis.

Chapter 2

Eulerian Elasto-Visco-Plastic Formulations for Residual Stress Prediction

2.1 Introduction

The finite element method has been successfully implemented to model history dependent problems such as forming, welding, rolling and extrusion for nearly thirty years [13, 14, 15, 16, 17, 18, 19, 20, 21, 22]. The formulations follow either the small deformation or the Updated Lagrangian theory. The material evolution in a Lagrangian reference frame becomes an initial value ordinary differential equation for each Gauss point which is solved by a time incremental scheme. Although Lagrangian formulations have been algorithmically easier to implement and have been proven robust for many applications, they may become computationally demanding in 3D models when several thousand time increments are needed such as in the case of laser or arc welding of large structures [24]. Lagrangian formulations can also lead to mesh distortion when the process exhibits very large deformations such as the case of friction stir welding.

Arbitrary Lagrangian Eulerian formulations with re-meshing have been used in these problems; however, numerical errors may develop and propagate over time [43].

For steady processing conditions, some manufacturing processes, such as welding, rolling and extrusion, can be treated as quasi-steady state in an Eulerian reference frame. This concept was proposed by Nguyen et al. [25]. For quasi-steady state processes, when the material flows through a fixed region in space, the state and properties of the material will not change in time. Therefore, in an Eulerian frame the time derivative terms are transformed to spacial gradient terms. The Eulerian analysis solves the problem at once rather than taking several time increments as in the Lagrangian. However, modeling the material evolution results into a boundary value partial differential equation coupled with the governing equation. The problem can be solved either as a mixed formulation or by using streamline integration methods [32].

In a mixed formulation, the material evolution partial differential equations have convection terms which may result in nonphysical oscillations in the solution. The most common method used to handle these convection-dominated problems is the Streamline Upwind Petrov-Galerkin (SUPG) method [38, 39, 40, 41]. In the SUPG method, the weighting function is the interpolation terms plus an additional mesh-dependent term.

In the streamline method, a sequential iterative approach is used, where, the velocity field is solved first from the governing equation. Then, streamlines are computed from the velocity field along which the constitutive equation is integrated to obtain the stress and strain [44]. In this method, an analytical element tangent matrix can not be obtained. The global tangent matrix can be computed by the finite difference method, but the matrix is full and the computational cost is increased dramatically.

Elasto-plastic formulations using displacement as a primary variable have been proposed in Reference [36]. The approach is applicable to rate independent problems and is capable of computing residual stress. However, the method exhibits convergence difficulties due to the abrupt transition of elastic to plastic response. Most other Eulerian analyses use the velocity field as the primary field. However, computing stress from the velocity field poses a new problem. One solution approach is to directly set the relationship between stress and strain rate by assuming the material is incompressible [45, 46, 47, 48]. This method treats the material as an incompressible fluid. Because the rate of strain can be derived directly from the velocity field, this method avoids complicated strain integration procedures. However, this approach can not predict residual stress. The other approach is to integrate strain from the velocity field [32]. Based on this concept, Maniatty, Dawson and Weber presented an elasto-visco-plastic Eulerian method [44], which can predict residual stress. However, this method can not handle low strain rate conditions. Thompson and Yu [35] have also proposed an Eulerian method using a rate equilibrium equation which can solve a pure elastic case. However, for the elasto-plastic condition, they simply reduced the maximum effective stress to a certain yield stress instead of considering the plastic material flow.

Stuart B. Brown, Kwon H. Kim and L. Anand [37] proposed a rate-dependent constitutive equation by introducing an internal variable to describe the plastic evolution. Unlike the rate independent elasto-plastic model, Anand's model does not have a yield stress and the plastic evolution is always on. Therefore, the transition from the pure elastic stage to the plastic stage is smoother than the elasto-plastic model. Weber and

Anand implemented their constitutive model in a Lagrangian reference frame using a time incremental method [49, 50].

In this paper, a Galerkin formulation with four field variables (velocity, stress, deformation gradient and internal variable) is developed for determining deformation, material state, and residual stress for quasi-steady processes. The material in the control domain is assumed to satisfy the rate of equilibrium equation. The Galerkin strain integration method is used to integrate the deformation gradient from the primary velocity filed. The rate-dependent Anand's constitutive equation is used and the SUPG method is applied to stabilize the convection term in the stress, deformation gradient and internal variable evolution equations.

2.2   Eulerian Formulations

In our analysis we seek a steady state Eulerian solution of an isotropic, homogeneous, elasto-visco-plastic material flowing through a two-dimensional spatial domain B with boundary ∂B.

A rate-dependent constitutive law, called Anand model [37], is used to describe elasto-visco-plastic material response. The plastic evolution of Anand model is always on and these is a smooth evolution of equivalent strain during the transition from mostly elastic to actively yielding response. A mixed Galerkin formulation is developed where four field variables are solved simultaneously, namely velocity, stress, deformation gradient and the internal variable. The governing equations for the boundary value problem on B are listed in Section 2.2.1.

2.2.1 Governing Equations

2.2.1.1 Rate Equilibrium Equation

The material derivative of the equilibrium equation can be written as [35]:

$$\frac{d}{dt}\left[\frac{\partial \sigma_{ij}}{\partial x_i}\right] = \frac{\partial P_{ij}}{\partial x_i} = 0 \tag{2.1}$$

where σ_{ij} is the Cauchy stress tensor and P_{ij} can be expressed as:

$$P_{ij} \equiv v_k \frac{\partial \sigma_{ij}}{\partial x_k} - \frac{\partial v_i}{\partial x_k}\sigma_{kj} + \frac{\partial v_k}{\partial x_k}\sigma_{ij} \tag{2.2}$$

with v_i is the velocity vector.

2.2.1.2 Galerkin Strain integration formulation

To integrate strain from the velocity field, the Galerkin strain integration formulation presented in Reference [32] is implemented. The evolution equation for the deformation gradient F_{ij} is:

$$\dot{F}_{ij} = v_k \frac{\partial F_{ij}}{\partial x_k} = L_{ik}F_{kj} \tag{2.3}$$

where the velocity gradient L_{ij} is:

$$L_{ij} = \frac{\partial v_i}{\partial x_j} \tag{2.4}$$

2.2.1.3 Internal variable evolution formulation

To calculate the visco-plastic rate of deformation tensor, the internal variable evolution formulation is implemented [49]:

$$\dot{s} = v_k \frac{\partial s}{\partial x_k} = g(\tilde{\sigma}, s) \tag{2.5}$$

where, s is the internal variable, $g(\tilde{\sigma}, s)$ is a constitutive function defined in Section 2.4.2, and the equivalent tensile stress $\tilde{\sigma}$ is defined by:

$$\tilde{\sigma} = \sqrt{\frac{3}{2} \sigma'_{ij} \sigma'_{ij}} \tag{2.6}$$

where, the Cauchy stress deviator σ'_{ij} is:

$$\sigma'_{ij} = \sigma_{ij} - \frac{1}{3} \sigma_{kk} \delta_{ij} \tag{2.7}$$

2.2.1.4 Stress Strain Relationship

The time derivative of the stress strain equation is added to the formulation. In this analysis, we only consider cases that the elastic modulus and Poisson's ratio are constant throughout the process. Therefore, the rate of the elasticity tensor term is zero.

$$\dot{\sigma}_{ij} = v_k \frac{\partial \sigma_{ij}}{\partial x_k} = C_{ijkl} \dot{E}^e_{kl} \tag{2.8}$$

where, C_{ijkl} is the fourth order isotropic elasticity tensor and $\dot{E}^e_{kl}$ is the rate of elastic strain tensor (see Appendix A):

$$\dot{E}^e_{ij} = \frac{1}{2}(L^a_{ji} + L^a_{ij})$$

with,

$$L^a_{ij} = F^{-1}_{ki} F^{-1}_{kl} L^e_{lj} \tag{2.9}$$

$$L^e_{ij} = L_{ij} - L^{th}_{ij} - L^{vp}_{ij} \tag{2.10}$$

L^e_{ij}, L^{th}_{ij} and L^{vp}_{ij} are the elastic, thermal and visco-plastic component of the velocity gradient respectively. In Reference [51], the authors show that the choice of zero thermal and plastic spinning tensor $(W^p_{ij} = W^{th}_{ij} = 0)$ can be used to solve finite strain plasticity problems, which leads to:

$$L^{th}_{ij} = D^{th}_{ij} \tag{2.11}$$

$$L^{vp}_{ij} = D^{vp}_{ij} \tag{2.12}$$

D^{th}_{ij}, D^{vp}_{ij} are the thermal and visco-plastic part of the rate of deformation tensor, which can be calculated as:

$$D^{th}_{ij} = \alpha\, v_k\, \frac{\partial T}{\partial x_k}\, \delta_{ij} \tag{2.13}$$

$$D^{vp}_{ij} = \sqrt{\frac{3}{2}}\dot{\varepsilon}^{vp} N_{ij} \tag{2.14}$$

where, $\dot{\bar{\varepsilon}}^{vp}$ is the equivalent visco-plastic strain rate defined by the constitutive function $f(\tilde{\sigma}, s)$ in Section 2.4.2, and N_{ij} is the direction of plastic flow tensor derived by:

$$\dot{\bar{\varepsilon}}^{vp} = f(\tilde{\sigma}, s) \tag{2.15}$$

$$N_{ij} = \sqrt{\frac{3}{2}} \frac{\sigma'_{ij}}{\tilde{\sigma}} \tag{2.16}$$

The corresponding boundary conditions are:

$$v_i = v_i^p \ \ on \ \ \partial B_v \tag{2.17}$$

$$n_i \cdot P_{ij} = t_j^p \ \ on \ \ \partial B_P \tag{2.18}$$

$$\sigma_{ij} = \sigma_{ij}^p \ \ on \ \ \partial B_\sigma \tag{2.19}$$

$$F_{ij} = F_{ij}^p \ \ on \ \ \partial B_F \tag{2.20}$$

$$s = s^p \ \ on \ \ \partial B_s \tag{2.21}$$

where v^p_i, σ^p_{ij}, F^p_{ij}, $\hat{s}^p$ and $\dot{t}^p_i$ are the velocity, stress, deformation gradient, internal variable and rate of traction specified on the boundary, respectively; n_i is the unit outward normal vector on the boundary ∂B. The boundary conditions (2.17) and (2.18) must be specified on the the entire boundary without overlap. Therefore, $\partial B_v \cup \partial B_P = \partial B$ and $\partial B_v \cap \partial B_P = \oslash$ should be satisfied. Because the state of the material entering the control volume must be known, the boundary conditions equations (2.19)-(2.21) need to be specified on the inlet boundary.

2.3 Weak Formulations

The boundary value problem defined in Section 2.2.1 is solved by expressing the problem in a weak form and then using the finite element method to solve the resulting system. The convection terms in Equation (2.3), (2.5) and (2.8) are known to sometimes become instable and cause spurious node-to-node oscillations in the solution. The cause of this numerical instability is discussed in References [52, 53], and the streamline upwind Petrov-Galerkin method [54] is shown to effectively suppress the oscillation by adding discontinuous weighting functions to the traditional Galerkin weighting functions. In this paper, Equations (2.3), (2.5) and (2.8) are stabilized using Petrov-Galerkin-type formulations. The stabilized weak formulations are:

$$\int_V \frac{\partial \hat{v}_i}{\partial x_j} \, P_{ij} \, dV - \int_S \hat{v}_j \, n_i \, P_{ij} \, dS = 0 \tag{2.22}$$

$$\int_V \left(v_k \frac{\partial \sigma_{ij}}{\partial x_k} - C_{ijkl} \, \dot{E}^e_{kl} \right) \left(\hat{\sigma}_{ij} + \tau_e \, v_k \frac{\partial \hat{\sigma}_{ij}}{\partial x_k} \right) dV = 0 \tag{2.23}$$

$$\int_V \left(v_k \frac{\partial F_{ij}}{\partial x_k} - L_{ik} F_{kj} \right) \left(\hat{F}_{ij} + \tau_e v_k \frac{\partial \hat{F}_{ij}}{\partial x_k} \right) dV = 0 \tag{2.24}$$

$$\int_V \left(v_k \frac{\partial s}{\partial x_k} - g(\tilde{\sigma}, s) \right) \left(\hat{s} + \tau_e v_k \frac{\partial \hat{s}}{\partial x_k} \right) dV = 0 \tag{2.25}$$

The stabilization factor τ_e is chosen to be

$$\tau_e = \beta \frac{h_e}{2|\mathbf{v}|} \tag{2.26}$$

where β is a non-dimensional, non-negative stability parameter, and h_e is the characteristic element length.

2.4 Numerical Implementations

Now the resulting problem is to find $(\mathbf{v}, \sigma, \mathrm{F}, \mathrm{s})$ lying in the space $V \times \boldsymbol{\sigma} \times \mathbf{F} \times \mathbf{S}$ that satisfies Equations (2.22)-(2.25). The Newton-Raphson method with a progressive solution procedure is used to solve this non-linear problem.

2.4.1 Finite Element Formulation

Two dimensional finite element discretization is applied to equations (2.22)-(2.25) to obtain the element residual and stiffness equations. Because the four unknown fields (velocity, stress, deformation gradient and internal variable) are solved simultaneously, each node of a four-node quadrilateral element contains of eleven degrees of freedom which are shown in Figure 2.1.

Degrees of Freedom at each node: Total

1: $V_x, V_y, \sigma_{xx}, \sigma_{yy}, \sigma_{zz}, \sigma_{xy}, F_{xx}, F_{xy}, F_{yx}, F_{yx}, S$ 11

2: $V_x, V_y, \sigma_{xx}, \sigma_{yy}, \sigma_{zz}, \sigma_{xy}, F_{xx}, F_{xy}, F_{yx}, F_{yx}, S$ 11

3: $V_x, V_y, \sigma_{xx}, \sigma_{yy}, \sigma_{zz}, \sigma_{xy}, F_{xx}, F_{xy}, F_{yx}, F_{yx}, S$ 11

4: $V_x, V_y, \sigma_{xx}, \sigma_{yy}, \sigma_{zz}, \sigma_{xy}, F_{xx}, F_{xy}, F_{yx}, F_{yx}, S$ 11

                                                      44
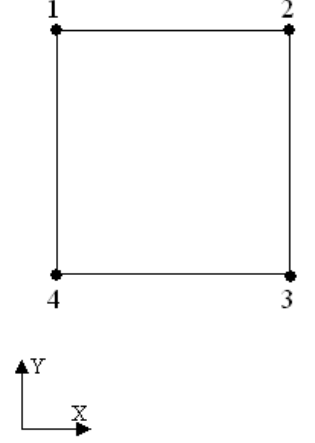
Fig. 2.1.   Mixed four-node quadrilateral element

2.4.1.1   Matrix Vector Transformation

In Section 2.2.1, the variables, such as, the stress σ_{ij}, rate of strain $\dot{E}_{ij}$ and deformation gradient F_{ij} are expressed in a tensor form. They need to be transformed to vector forms before computing the element residual vector and the element tangent matrix. In this paper, we define two matrix-vector transformation types. One of them is the bar ($^{-}$) transformation, which can transform symmetric tensors to engineering format vectors. The stress tensor σ_{ij}, stress deviator tensor σ'_{ij} and the rate of elastic strain tensor $\dot{E}^e_{ij}$ are symmetric tensors, and they can be transformed to their vector

forms by the bar transformation as:

$$
\bar{\boldsymbol{\sigma}} = \begin{bmatrix} \sigma_{xx} \\ \sigma_{yy} \\ \sigma_{zz} \\ \sigma_{xy} \end{bmatrix} \quad ; \quad \bar{\boldsymbol{\sigma}}' = \begin{bmatrix} \sigma'_{xx} \\ \sigma'_{yy} \\ \sigma'_{zz} \\ \sigma'_{xy} \end{bmatrix} \quad ; \quad \dot{\bar{\mathbf{E}}}^e = \begin{bmatrix} \dot{E}^e_{xx} \\ \dot{E}^e_{yy} \\ \dot{E}^e_{zz} \\ \dot{E}^e_{xy} \end{bmatrix} \tag{2.27}
$$

The other transformation type is tilde ($\tilde{\ }$) transformation, which can transform unsymmetrical tensors to their vector form. The deformation gradient F_{ij}, the material derivative of the first Piola-Kirchhoff stress P_{ij} and the velocity gradient L_{ij} are unsymmetrical tensors, their tilde transformations are:

$$
\tilde{\mathbf{F}} = \begin{bmatrix} F_{xx} \\ F_{yx} \\ F_{xy} \\ F_{yy} \end{bmatrix} \quad ; \quad \tilde{\mathbf{P}} = \begin{bmatrix} P_{xx} \\ P_{yx} \\ P_{xy} \\ P_{yy} \end{bmatrix} \quad ; \quad \tilde{\mathbf{L}} = \begin{bmatrix} L_{xx} \\ L_{yx} \\ L_{xy} \\ L_{yy} \end{bmatrix} \tag{2.28}
$$

The stress strain relation equation (2.8) can be expressed in the vector format as:

$$
\dot{\bar{\sigma}}_i = \bar{C}_{ij} \dot{\bar{E}}^e_j \tag{2.29}
$$

where, $\bar{C}_{ij}$ is the fourth order isotropic elasticity tensor written in the matrix form:

$$\bar{\mathbf{C}} = \frac{E}{(1+\nu)(1-2\nu)} \begin{bmatrix} (1-\nu) & \nu & \nu & 0 \\ \nu & (1-\nu) & \nu & 0 \\ \nu & \nu & (1-\nu) & 0 \\ 0 & 0 & 0 & .5-\nu \end{bmatrix} \qquad (2.30)$$

Based on the two types of transformation, the vector form of the definition of the material derivative of the first Piola-Kirchhoff stress P_{ij} in Equation (2.2) is:

$$\tilde{P}_i = G_{ij}\bar{C}_{jk}\dot{\bar{E}}^e_k - G_{ij}L^M_{jk}\bar{\sigma}_k + H_{mn}L^M_{mn}G_{ij}\bar{\sigma}_j \qquad (2.31)$$

where, the transformation matrices G and H are defined as:

$$\mathbf{G} = \begin{bmatrix} 1 & 0 & 0 & 0 \\ 0 & 0 & 0 & 1 \\ 0 & 0 & 0 & 1 \\ 0 & 1 & 0 & 0 \end{bmatrix} ; \quad \mathbf{H} = \begin{bmatrix} 1 & 0 & 0 & 0 \\ 0 & 1 & 0 & 0 \\ 0 & 0 & 0 & 0 \\ 0 & 0 & 0 & 0 \end{bmatrix} ; \qquad (2.32)$$

with the velocity gradient tensor L_{ij} rewritten in the following matrix form L_{ij}^M:

$$
\mathbf{L}^M = \begin{bmatrix} L_{11} & L_{12} & 0 & 0 \\ L_{21} & L_{22} & 0 & 0 \\ 0 & 0 & L_{11} & L_{12} \\ 0 & 0 & L_{21} & L_{22} \end{bmatrix}
\tag{2.33}
$$

The traction rate vector $\dot{t}^p$ can be obtained as:

$$
\dot{\mathbf{t}}^p = \begin{bmatrix} n_1 & n_2 & 0 & 0 \\ 0 & 0 & n_1 & n_2 \end{bmatrix} \cdot \begin{bmatrix} P_{xx} & P_{yx} & P_{xy} & P_{yy} \end{bmatrix}^T
\tag{2.34}
$$

2.4.1.2 Finite Element Residual Equations

An isoparametric four-node quadrilateral finite element discretization is applied to the weak formulations (2.22)-(2.25) to obtain the expressions for the element residual vector and the element Jacobian matrix. The same shape functions are used to interpolate the coordinate, velocity, stress, deformation gradient and internal variables of a point within the element from these values of nodes. Matrices $\mathbf{N}^{v,\sigma,F,s}$ and $\mathbf{B}^{v,\sigma,F,s,L}$ are shape functions and gradient interpolators which are developed in Appendix B. w is the Gaussian weighting function. J and j are the volume and area determinant of the Jacobian matrices respectively. The assembly of the element residual vector $\mathbf{R}$ and

nodal field vector $\mathbf{U}$ is obtained as follows:

$$
\mathbf{R} = \left\{ \begin{array}{c} \mathbf{R}^{\upsilon} \\ \mathbf{R}^{\sigma} \\ \mathbf{R}^{F} \\ \mathbf{R}^{s} \end{array} \right\} ; \quad \mathbf{U} = \left\{ \begin{array}{c} \mathbf{U}^{\upsilon} \\ \mathbf{U}^{\sigma} \\ \mathbf{U}^{F} \\ \mathbf{U}^{s} \end{array} \right\} \tag{2.35}
$$

The expressions of the components of the element residual are:

$$
R_i^{\upsilon} = \sum_{VGaussPoint} \left[B_{ji}^{\upsilon} \tilde{P}_j \right] \omega J - \sum_{AtGaussPoint} \left[N_{ji}^{\upsilon} t_j^{P} \right] \omega j \tag{2.36}
$$

$$
R_i^{\sigma} = \sum_{VGaussPoint} \left[N_{mi}^{\sigma} + \tau_e \upsilon_k B_{mik}^{\sigma} \right] \left[B_{mjk}^{\sigma} \upsilon_k U_j^{\sigma} - \bar{C}_{mj} \dot{\bar{E}}_j^{e} \right] \omega J \tag{2.37}
$$

$$
R_i^{F} = \sum_{VGaussPoint} \left[N_{mi}^{F} + \tau_e \upsilon_k B_{mik}^{F} \right] \left[B_{mjk}^{F} \upsilon_k U_j^{F} - L_{ml}^{M} N_{lj}^{F} U_j^{F} \right] \omega J \tag{2.38}
$$

$$
R_i^{s} = \sum_{VGaussPoint} \left[N_i^{s} + \tau_e \upsilon_k B_{ki}^{s} \right] \left[B_{kj}^{s} \upsilon_k U_j^{s} - g(\tilde{\sigma}, s) \right] \omega J \tag{2.39}
$$

2.4.1.3   Element Stiffness matrix

Linearization of equations (2.36)-(2.39) leads to the following element tangent matrix:

$$\frac{\partial \mathbf{R}}{\partial \mathbf{U}} = \begin{bmatrix} \dfrac{\partial \mathbf{R}^v}{\partial \mathbf{U}^v} & \dfrac{\partial \mathbf{R}^v}{\partial \mathbf{U}^\sigma} & \dfrac{\partial \mathbf{R}^v}{\partial \mathbf{U}^F} & \dfrac{\partial \mathbf{R}^v}{\partial \mathbf{U}^s} \\[2em] \dfrac{\partial \mathbf{R}^\sigma}{\partial \mathbf{U}^v} & \dfrac{\partial \mathbf{R}^\sigma}{\partial \mathbf{U}^\sigma} & \dfrac{\partial \mathbf{R}^\sigma}{\partial \mathbf{U}^F} & \dfrac{\partial \mathbf{R}^\sigma}{\partial \mathbf{U}^s} \\[2em] \dfrac{\partial \mathbf{R}^F}{\partial \mathbf{U}^v} & \dfrac{\partial \mathbf{R}^F}{\partial \mathbf{U}^\sigma} & \dfrac{\partial \mathbf{R}^F}{\partial \mathbf{U}^F} & \dfrac{\partial \mathbf{R}^F}{\partial \mathbf{U}^s} \\[2em] \dfrac{\partial \mathbf{R}^s}{\partial \mathbf{U}^v} & \dfrac{\partial \mathbf{R}^s}{\partial \mathbf{U}^\sigma} & \dfrac{\partial \mathbf{R}^s}{\partial \mathbf{U}^F} & \dfrac{\partial \mathbf{R}^s}{\partial \mathbf{U}^s} \end{bmatrix} \tag{2.40}$$

Where,

$$\frac{\partial R^v_j}{\partial U^v_n} = \sum_{VGaussPoint} B^v_{ij} \left[G_{ip}\bar{C}_{pk}\frac{\partial \dot{E}^e_k}{\partial U^v_n} - G_{il}B^L_{lkn}\bar{\sigma}_k + G_{ik}\bar{\sigma}_k H_{ml}B^L_{mln} \right] \omega J \tag{2.41}$$

$$\frac{\partial R^v_j}{\partial U^\sigma_p} = \sum_{VGaussPoint} B^v_{ij} \left[-G_{il}L^M_{lk}N^\sigma_{kp} + H_{mn}L^M_{mn}G_{il}N^\sigma_{lp} \right] \omega J \tag{2.42}$$

$$\frac{\partial R^v_j}{\partial U^F_n} = \sum_{VGaussPoint} B^v_{ij} \left[G_{ip}\bar{C}_{pk}\frac{\partial \dot{E}^e_k}{\partial U^F_n} \right] \omega J \tag{2.43}$$

$$\frac{\partial R^v_j}{\partial U^s_n} = \sum_{VGaussPoint} B^v_{ij} \left[G_{ip}\bar{C}_{pk}\frac{\partial \dot{E}^e_k}{\partial U^s_n} \right] \omega J \tag{2.44}$$

$$\frac{\partial R^\sigma_m}{\partial U^v_p} = \sum_{VGaussPoint} \left[N^\sigma_{im}B^\sigma_{ijk}N^v_{kp}U^\sigma_j + \tau_e B^\sigma_{imk}N^v_{kp}\left(2B^\sigma_{ijk}v_k U^\sigma_j - \bar{C}_{ij}\dot{E}^e_j \right) \right] \omega J -$$
$$\left[\left(N^\sigma_{im} + \tau_e v_k B^\sigma_{imk} \right) \cdot \bar{C}_{ij}\frac{\partial \dot{E}^e_j}{\partial U^v_p} \right] \omega J \tag{2.45}$$

$$\frac{\partial R^{\sigma}_{m}}{\partial U^{\sigma}_{j}} = \sum_{VGaussPoint} \left[N^{\sigma}_{im} + \tau_e v_k B^{\sigma}_{imk} \right] \left[B^{\sigma}_{ijk} v_k \right] \omega J \tag{2.46}$$

$$\frac{\partial R^{\sigma}_{m}}{\partial U^{F}_{p}} = \sum_{VGaussPoint} \left[N^{\sigma}_{im} + \tau_e v_k B^{\sigma}_{imk} \right] \left[\bar{C}_{ij} \frac{\partial \dot{E}^e_{j}}{\partial U^{F}_{p}} \right] \omega J \tag{2.47}$$

$$\frac{\partial R^{\sigma}_{m}}{\partial U^{s}_{p}} = \sum_{VGaussPoint} \left[N^{\sigma}_{im} + \tau_e v_k B^{\sigma}_{imk} \right] \left[\bar{C}_{ij} \frac{\partial \dot{E}^e_{j}}{\partial U^{s}_{p}} \right] \omega J \tag{2.48}$$

$$\frac{\partial R^{F}_{m}}{\partial U^{v}_{p}} = \sum_{VGaussPoint} \left[N^{F}_{im} B^{F}_{ijk} N^{v}_{kp} U^{F}_{j} + \tau_e B^{F}_{imk} N^{v}_{kp} \left(2B^{F}_{iqk} v_k U^{F}_{q} - L^{M}_{il} N^{F}_{lj} U^{F}_{j} \right) \right] \omega J$$
$$- \left[(N^{F}_{im} + \tau_e v_k B^{F}_{imk}) \cdot B^{L}_{ilp} N^{F}_{lj} U^{F}_{j} \right] \omega J \tag{2.49}$$

$$\frac{\partial R^{F}_{i}}{\partial U^{\sigma}_{j}} = 0 \tag{2.50}$$

$$\frac{\partial R^{F}_{m}}{\partial U^{F}_{j}} = \sum_{VGaussPoint} \left[N^{F}_{im} + \tau_e v_k B^{F}_{imk} \right] \left[B^{F}_{ijk} v_k - L^{M}_{il} N^{F}_{lj} \right] \omega J \tag{2.51}$$

$$\frac{\partial R^{F}_{i}}{\partial U^{s}_{j}} = 0 \tag{2.52}$$

$$\frac{\partial R^{s}_{i}}{\partial U^{v}_{p}} = \sum_{VGaussPoint} \left[N^{s}_{i} B^{s}_{kj} N^{v}_{kp} U^{s}_{j} \right] \omega J$$
$$+ \tau_e B^{s}_{ki} N^{v}_{kp} \left[2B^{s}_{mj} v_m U^{s}_{j} - g(\tilde{\sigma}, s) \right] \omega J \tag{2.53}$$

$$\frac{\partial R^{s}_{i}}{\partial U^{\sigma}_{j}} = \sum_{VGaussPoint} \left[N^{s}_{i} + \tau_e v_k B^{s}_{ki} \right] \left[-\frac{\partial g(\tilde{\sigma}, s)}{\partial U^{\sigma}_{j}} \right] \omega J \tag{2.54}$$

$$\frac{\partial R^{s}_{i}}{\partial U^{F}_{j}} = 0 \tag{2.55}$$

$$\frac{\partial R^s_i}{\partial U^s_j} = \sum_{V\,Gauss\,Point} \left[N^s_i + \tau_e v_k B^s_{ki} \right] \left[B^s_{kj} v_k - \frac{\partial g(\tilde{\sigma}, s)}{\partial U^s_j} \right] \omega J \qquad (2.56)$$

The details of expression $\frac{\partial \dot{\tilde{E}}_i}{\partial U_j}$ in the above equations are shown in Appendix C.

2.4.2 Constitutive Law and Material Properties

The constitutive law implemented in this paper is a rate dependent elasto-visco-plastic model originally presented in Reference [37]. The function $f(\tilde{\sigma}, s)$ in Equation (2.15) is taken to be

$$\dot{\varepsilon}^{vp} = f(\tilde{\sigma}, s) = A \left(sinh \left(\xi \frac{\tilde{\sigma}}{s} \right) \right)^{\frac{1}{m}} \qquad (2.57)$$

where $A = A_0 \cdot exp(-Q/RT)$, Q is the thermal activation energy, R is the ideal gas constant, and T is the absolute temperature. A_0, ξ and m are the material parameters listed in Table 2.1.

The internal variable evolution Equation (2.5), defined by the function g, is chosen to be:

$$g(\tilde{\sigma}, s) = h_0 \left| \left(1 - \frac{s}{s^*} \right) \right|^a \; sign \left(1 - \frac{s}{s^*} \right) \cdot A \left(sinh \left(\xi \frac{\tilde{\sigma}}{s} \right) \right)^{\frac{1}{m}} \qquad (2.58)$$

with,

$$s^* = \tilde{s} \left(\frac{\dot{\varepsilon}^{vp}}{A} \right)^n \qquad (2.59)$$

where h_0, a s and n are the material parameters listed in Table 2.1.

Material Parameter	Value	Material Parameter	Value
A_0	$6.34 * 10^{11} sec^{-1}$	Q	312.35 KJ/mole
ξ	3.25	R	8.314
m	0.1956	a	1.5
n	0.06869	$\tilde{s}$	125.1 MPa
s_0	80 MPa	h_0	3093.1 MPa

Table 2.1. Material Parameters for HSLA-65 steel

HSLA-65 steel with strain rate between $1 * 10^{-3}$ and $1 * 10^{-4}$ is considered in this work. The material properties of the HSLA-65 steel are listed in Table 2.1. These material parameters are determined based on the experimental stress-strain plot of the HSLA-65 steel shown in Reference [55]. Using the radial-return algorithm presented in Reference [56], the computed stress-strain relationships of the HSLA-65 under different temperatures are shown in Figure 2.2.

2.4.3   Solution Method

For pure elastic cases with $\dot{\tilde{\varepsilon}}^{vp} = 0$, the problems defined by Equations (2.22)-(2.25) can converge steadily using Newton-Raphson method. However, for plastic problems, the finite element solution will encounter convergence problems, even though the transition between the elastic and plastic states is smooth for the Anand model. The cause of the convergence difficulty is the constitutive law in Equation (2.57), which uses
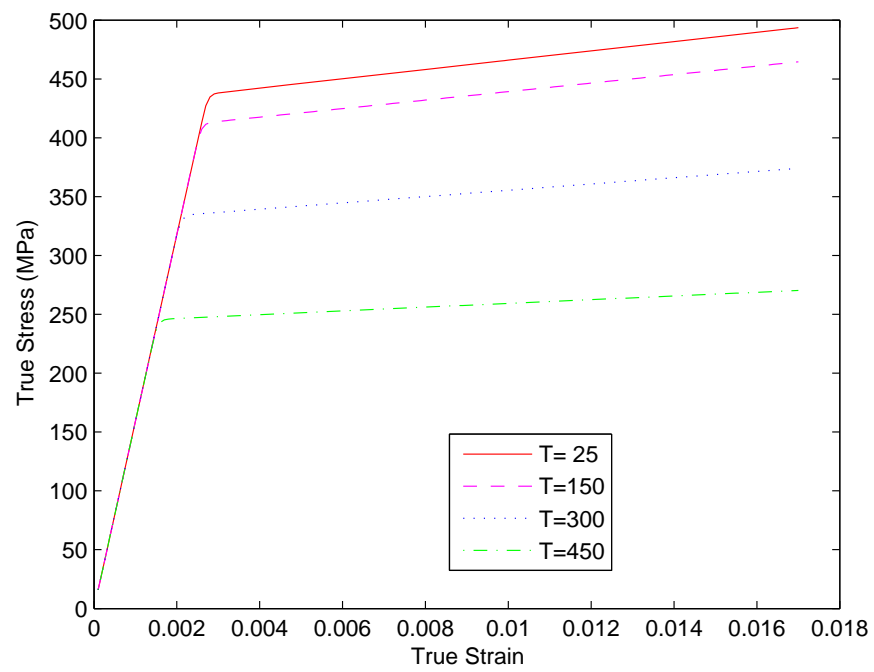
Fig. 2.2. Stress-Strain Curves of HSLA-65 Steel Under Different Temperature

the highly nonlinear *sinh* function to indicate if the internal variable begins to develop or not. Thus, it is difficult to obtain a trial solution within the radius of convergence of the Newton-Raphson method.

In this work, we implement a progressive stiffening algorithm to obtain robust convergence for elasto-visco-plastic problems. We begin with a smoother exponential function and gradually switch the function over to the final *sinh* function, as shown in Figure 2.3. In this procedure, Equation (2.57) is replaced by:

$$f_p(k) = f_{begin} * (1 - k) + f \cdot k^3 \qquad (2.60)$$

where, k is a control variable ranging from 0 to 1, $f_p(k)$ is a progressively stiffened function of the visco-plastic strain rate $\dot{\tilde{\varepsilon}}^{vp}$, f_{begin} is the starting function of $\dot{\tilde{\varepsilon}}^{vp}$ defined by:

$$f_{begin} = \left(exp\left(\frac{\tilde{\sigma}}{s}\right) - 1 \right) * \alpha_{begin} \qquad (2.61)$$

where the parameter α_{begin} can be determined by:

$$\alpha_{begin} = exp\left(\frac{1}{\xi} \cdot asinh\left(\left(\frac{\beta}{A}\right)^m \right) - 1 \right) \cdot \frac{1}{\beta} \qquad (2.62)$$

At the first iteration, k is set to 0 and $f_p = f_{begin}$. Because f_{begin} is closer to the pure elastic condition ($\dot{\tilde{\varepsilon}}^{vp} = 0$), only a small amount of plasticity is developed in this step, thus the problems can converge steadily at this step. Upon convergence with $k = 0$, k is progressively increased and the iterations are repeated for each increase of k using
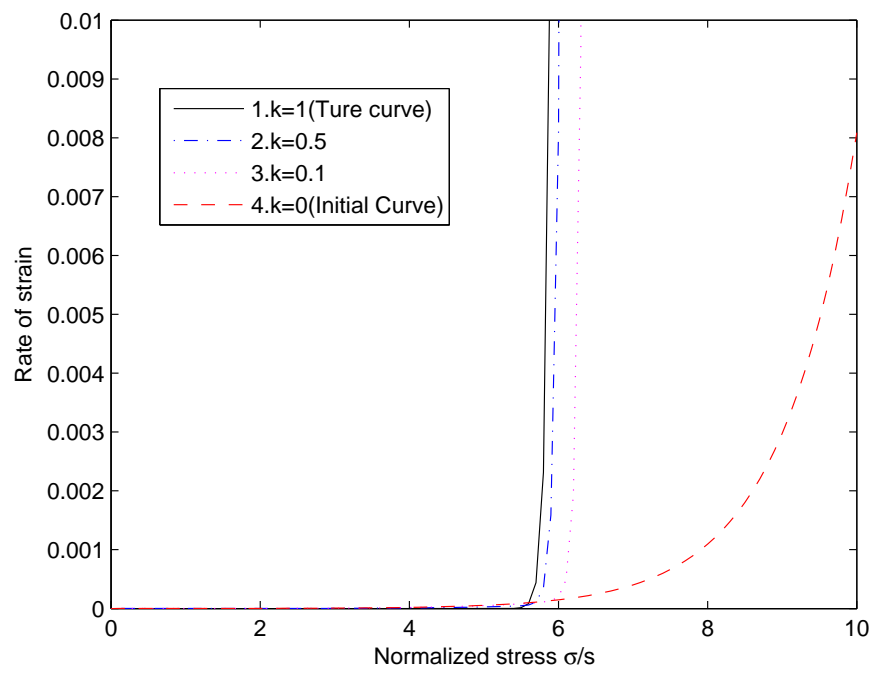
Fig. 2.3.   Progressive Stiffening Procedure

the solutions of previous k value as a starting point for the Newton-Raphson's method. The parameter β in Equation (2.62) is used to define how much plasticity is developed at the beginning step. In this paper, β is set to be 10^{-4}. If a larger value of β is used, it is hard to converge at the first step, for the beginning state is more nonlinear. On the other hand, if a smaller β is considered, the total computational time will increase, because more k steps need to be performed before the procedure reaches the final step $k = 1$.

2.5 Numerical Examples

An OMP FORTRAN 90 computer program of the above stabilized formulation has been developed for a four-node quadrilateral element. Two examples are investigated to verify the validity of the formulations. In the first example, the same radial flow example with a given velocity field as in Reference [32] is used in order to compare with an analytical solution. The second example is a strip drawing example, which is similar to the test problem in Reference [35], from which we can verify the pure elastic and elasto-visco-plastic behavior of the formulations.

2.5.1 Radial Flow Example

Figure 2.4 shows the geometry of the annular region of the radial flow. The annular region has inner radius $R_{in} = 1m$ and outer radius $R_{out} = 2m$. The angle a between the side surface and the center line of the annular region is 10°. Material enters the inlet surface A with a velocity $v_{in} = 0.1m/s$ and leaves the control volume from the outlet surface B. Only elastic deformation is considered in this example, therefore
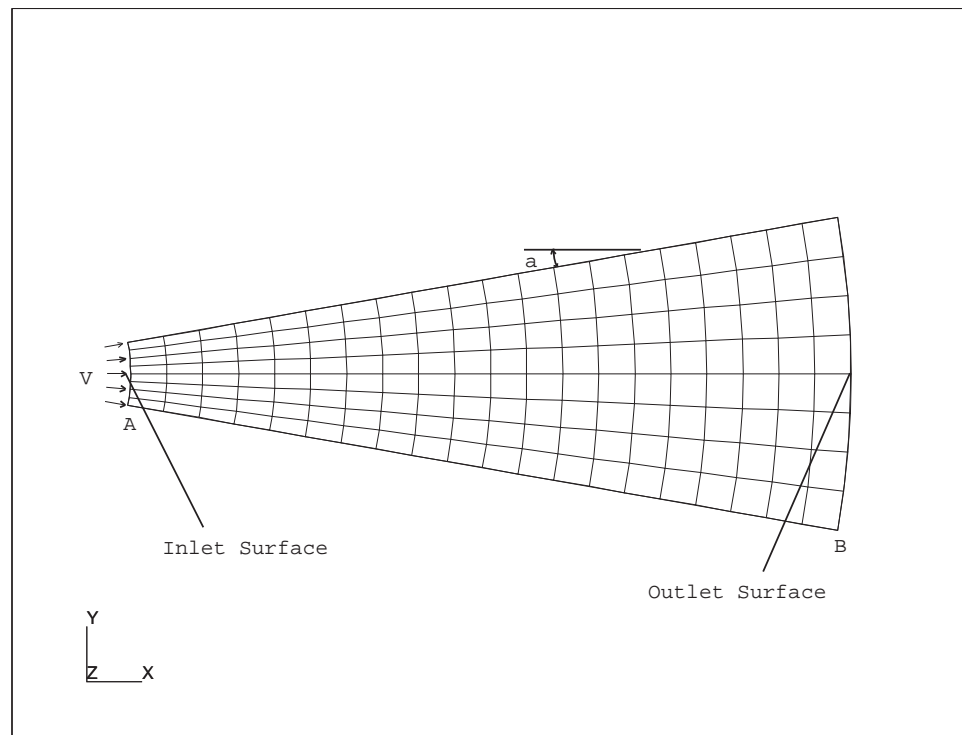
Fig. 2.4.   Radial flow model

the internal variable evolution equation is constrained and a small elastic modulus, $E = 1000MPa$, is used. To simulate the incompressible condition, the Possion's ratio of this example is $\nu = 0.499$. Because the material is incompressible and the flow is one dimensional (in cylindrical coordinates), the velocity field is known within the entire control volume, which is given as:

$$v_r = \frac{v_{in} * r_{in}}{r} \tag{2.63}$$

$$v_x = v_r * \cos a \tag{2.64}$$

$$v_y = v_r * \sin a \tag{2.65}$$

The given velocity field constrains the rate equilibrium equation, and the elastic condition inactivates the internal variable evolution equation. Therefore only stress and deformation gradient equations are activated in this example. The boundary conditions of these two fields are: $\boldsymbol{\sigma} = 0$ and $F = I$ at the inlet surface, which indicates there is no force applied on the inlet boundary and the material entering the region is undeformed. The given annular region is discretized into 160 four-node quadrilateral elements. The F_{xy} and F_{yx} components of deformation gradient results for this model are zero. Contour plots for the F_{xx} and F_{yy} components of deformation gradient and the Mises stress of the radial flow are shown in Figures 2.5, 2.6 and 2.7 respectively.

Both the stress and deformation gradient equations have convection terms which are known to cause numerical instability. There are very small oscillations that can be observed from the contour plots of both F_{xx} and F_{yy} component results. Especially for
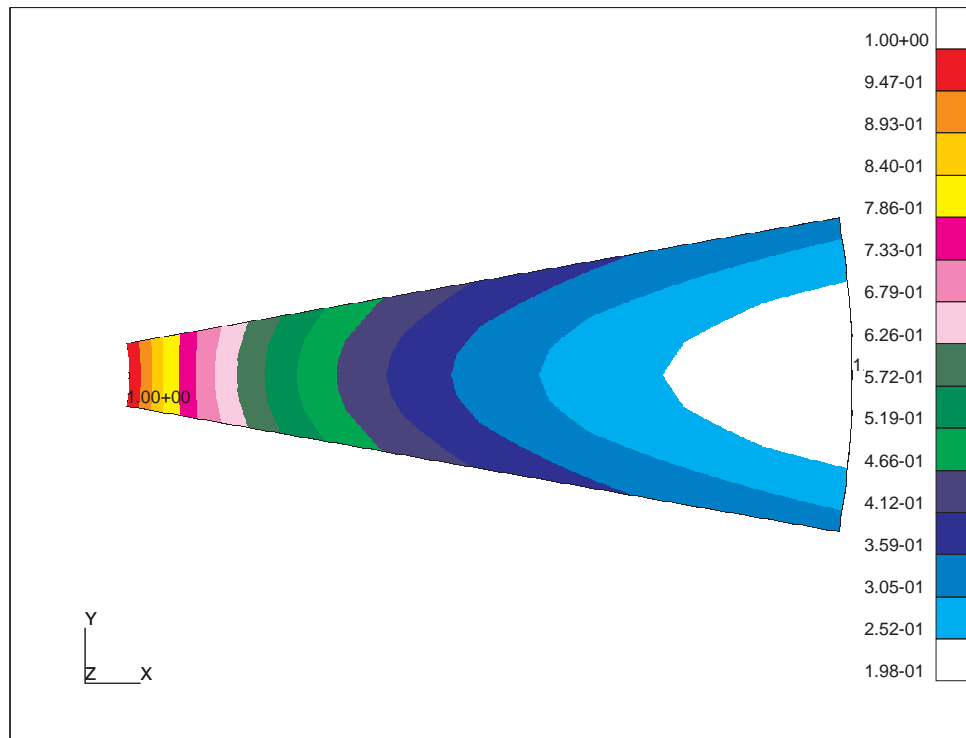
Fig. 2.5. F_{xx} component of deformation gradient $\mathbf{F}$
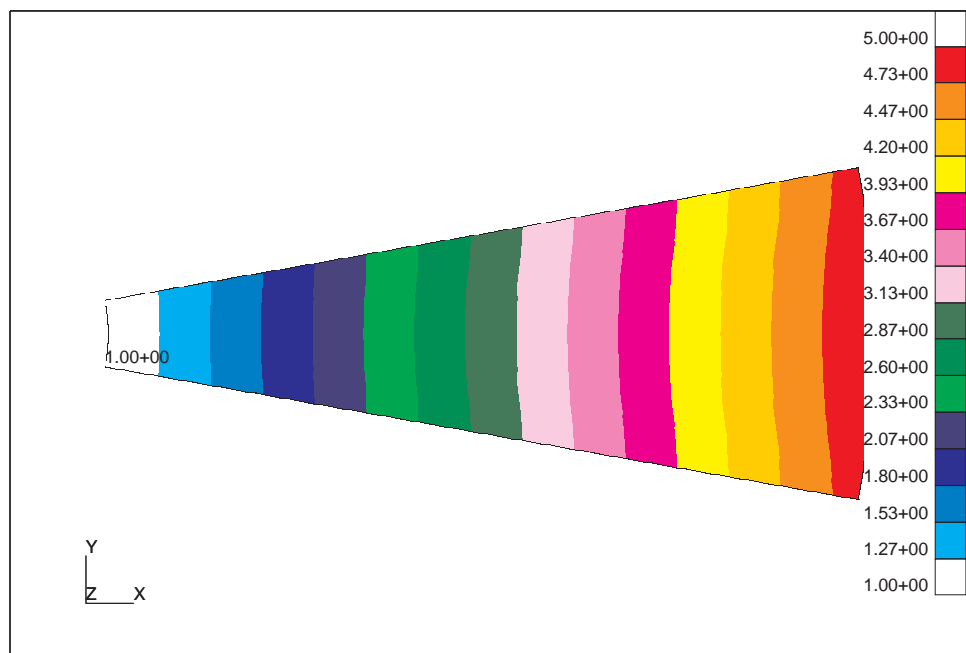
Fig. 2.6. F_{yy} component of deformation gradient $\mathbf{F}$
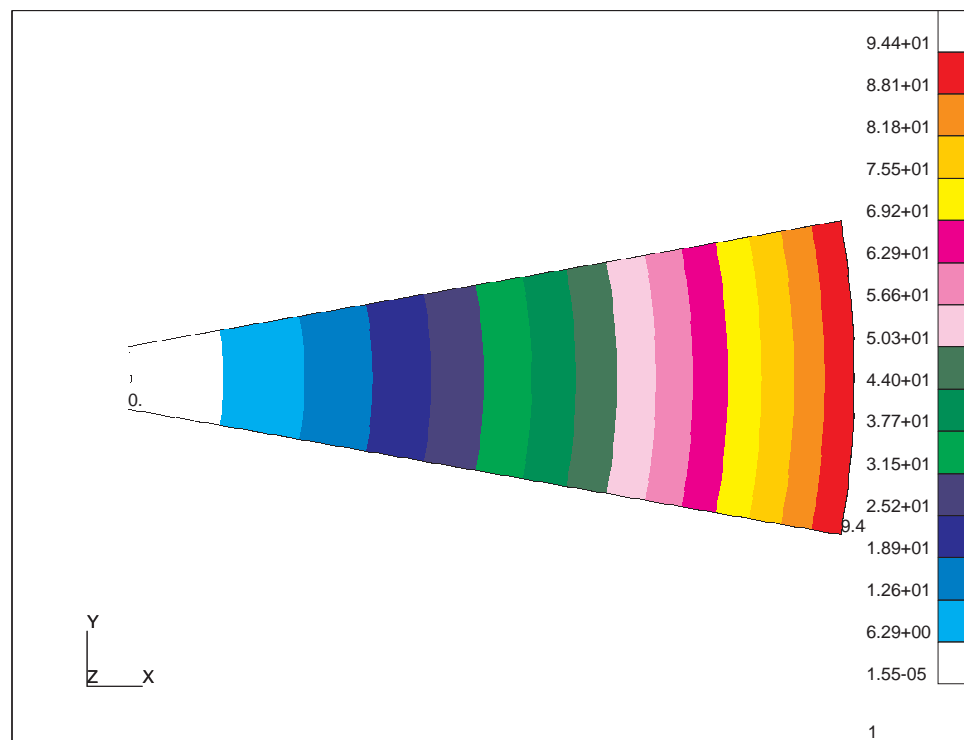
Fig. 2.7. von Mises Stress results of radial flow

the F_{yy} component, when the value is increased form 1 to 5, the oscillation near the outlet boundary is hard to be found. Therefore the stabilization method works very well with this kind of mesh size.

A coarser mesh size model with only 20 elements is also studied. Figures 2.8 , 2.9 and 2.10 show comparison plots of F_{xx}, F_{yy} and the Mise stresses along the center line of the domain. Lines 1, 2, 3 show the exact solution, 20 element mesh results and 160 element mesh results, respectively. The 160 elements F_{xx} component results are almost the same as the exact solution. The error of the coarse mesh results is larger than the 160 element mesh results, but there is no oscillation, which indicates when the mesh becomes coarse the solution is still stable. The same observation can also be made from the results of F_{yy} component and Mises stress.

For this simple elastic one-dimensional flow problem, the stabilized mix finite element method yields accurate solutions for both the deformation gradient field and the stress field. For coarse meshes, the solution remains stable, only the computational errors due to discretization are increased.

2.5.2   Strip Drawing Example

A strip drawing through a frictionless die is used to test the mixed finite element formulation. Figure 2.11 shows the geometry of the strip drawing example. The model is discretized into 300 mixed four-node quadrilateral elements. Surface A is the inlet surface where the material enters the control volume and surface B is the outlet surface where the material leaves the control volume. Due to symmetry, only a half of the model is considered, the surface C is the symmetric boundary. A fourth order polynomial
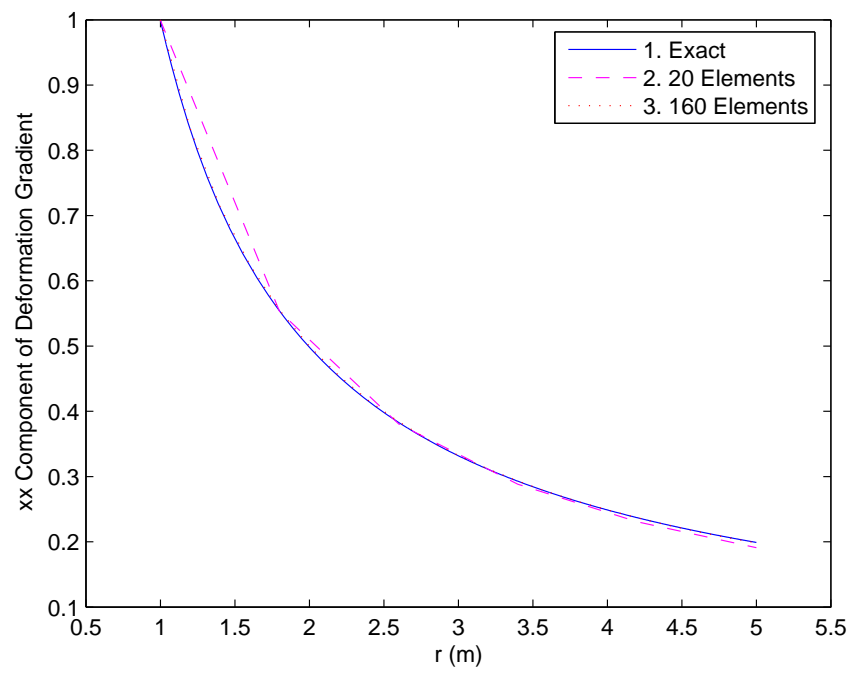
Fig. 2.8. Computed F_{xx} along the center line compared with the exact solution
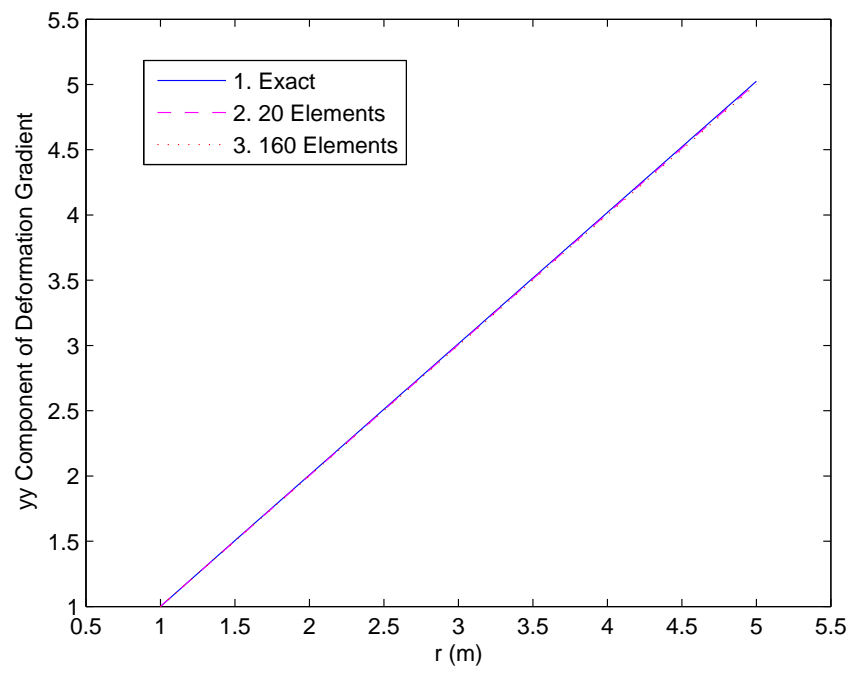
Fig. 2.9. Computed F_{yy} along the center line compared with the exact solution
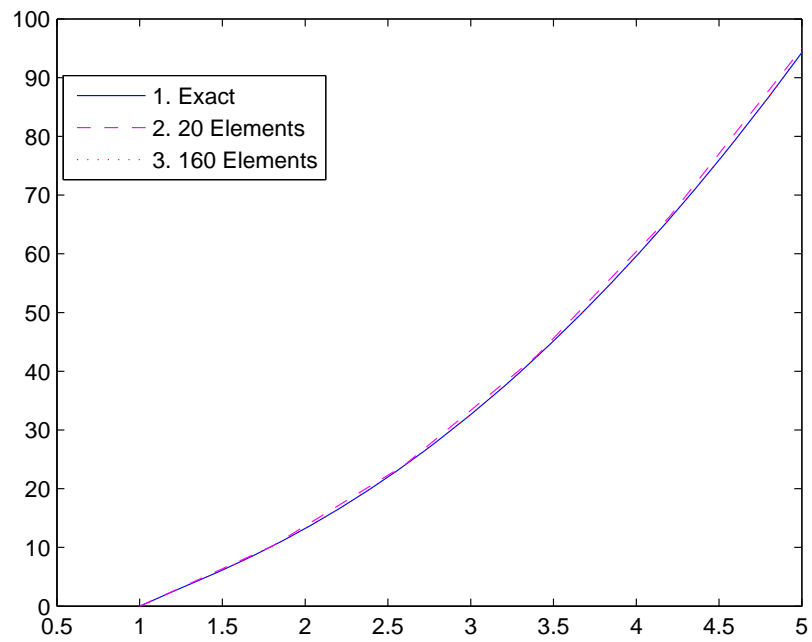
Fig. 2.10.   Computed stress along the center line compared with the exact solution
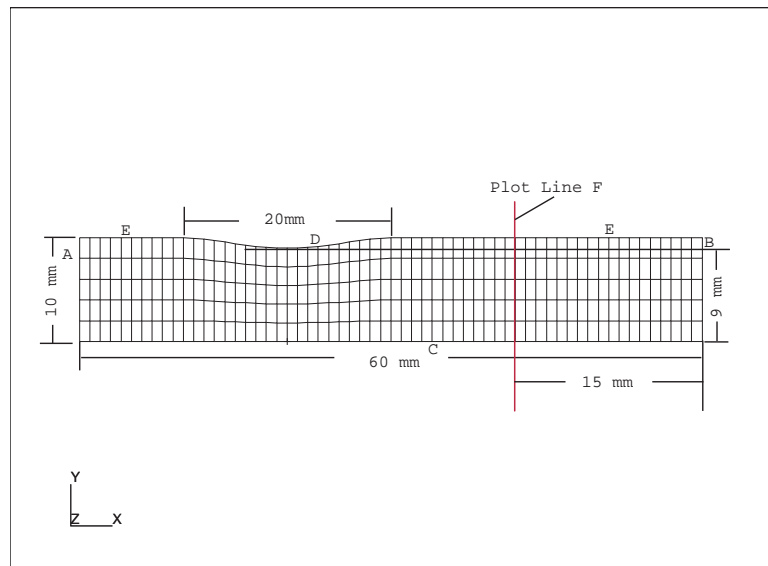
Fig. 2.11.   Strip Drawing Model in Eulerian Frame

function is used to describe the die curvature such that the slope is zero at both ends and midpoint of the die surface D. The material is reduced 10 percent as it goes thought the die. The temperature is assumed to be 20 $^\circ$C everywhere and the Poisson's ratio of this example is 0.3.

The boundary conditions for this model are:

- Inlet Surface A

$$v_x = v_{in} = .1mm/s \tag{2.66}$$

$$v_y = 0 \tag{2.67}$$

$$\sigma_{ij} = 0 \tag{2.68}$$

$$F_{ij} = \delta_{ij} \tag{2.69}$$

- Symmetric Surface C

$$v_y = 0 \tag{2.70}$$

- Die Surface A

$$v_y = f' v_x \tag{2.71}$$

$$\dot{t}_n = \frac{u_t}{\rho} t_n \tag{2.72}$$

To simulate the frictionless die surface, the proper boundary conditions need to be applied to the die surface. Equation (2.71) constrains only the Y direction of velocity on the die surface, and forces the flow to go along the tangent direction of the die surface. Although the traction in the tangent direction of the die surface is zero, the tangent traction rate is not zero, which can be derived by Equation (2.72). For details see Reference [35].

2.5.2.1 Elastic case
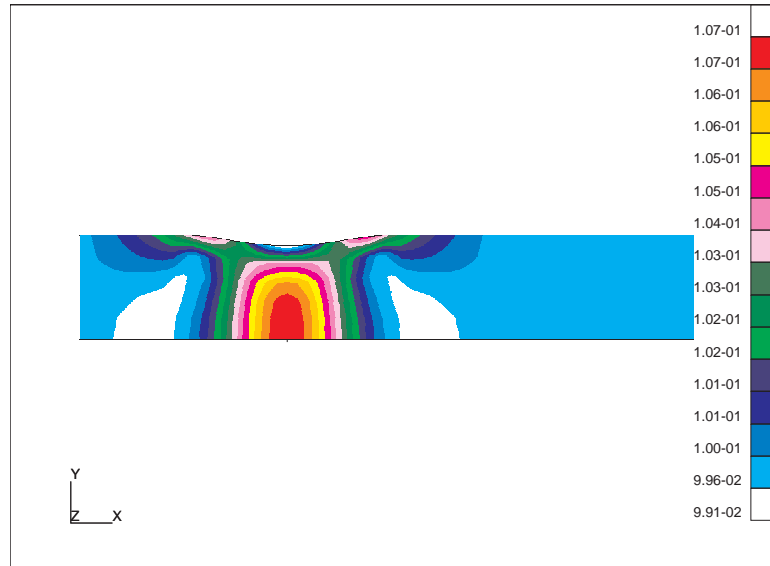
Fig. 2.12. X Component Velocity of Strip Drawing (Elastic Case): Unit[mm/s]

The strip drawing model with pure elastic response is firstly studied. In this case, the internal variable evolution equation is constrained to be 80MPa throughout
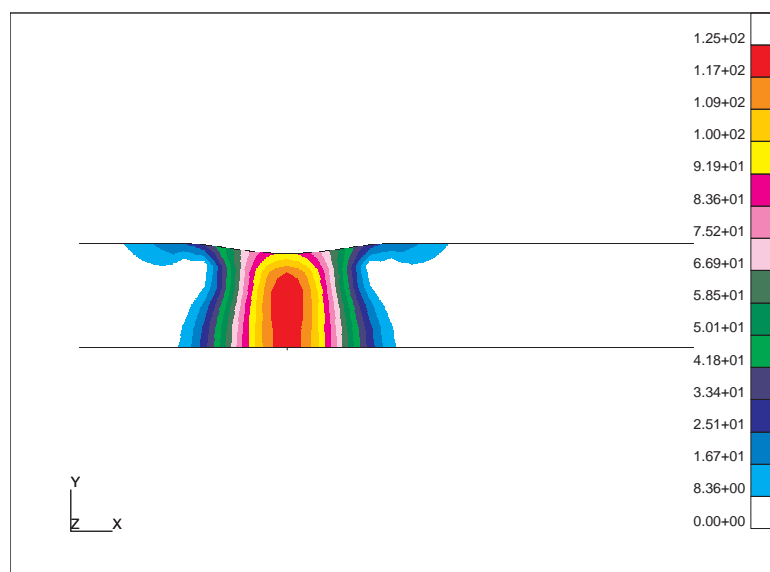
Fig. 2.13.   Von Mises Stress of Strip Drawing (Elastic Case): Unit[MPa]

the domain, and a small Young's modulus $E = 1000MPa$ is applied to the material. Because the mass and energy are conserved when the elastic material goes through the frictionless die, the velocity and stress state at the outlet boundary should be the same as the inlet boundary.

Figures 2.12 and 2.13 show the contour plots of the velocity and Mises stress results. On the outlet surface, the velocity recovers to the same value as the inlet boundary, and the stress also returns to zero. Thus, the equilibrium condition is satisfied on the outlet surface.

2.5.2.2 Elasto-visco-plastic case

The elasto-visco-plastic analysis of the strip drawing model is performed in this section. The internal variable evolution equation is activate in this case and the Young's modulus $E = 2.06 * 10^5 MPa$ is used to represent HSLA-65 steel. The material properties of the HSLA-65 steel are listed in Section 2.4.2. When the material goes through the die, permanent plastic deformations will occur in the material and make the plate thinner. To avoid finding the thickness of the plate exiting the die, the following boundary condition for the side surface E is applied for the plastic case:

- Side Surface E

$$v_y = 0 \tag{2.73}$$

Figures 2.14, 2.15 and 2.16 show the velocity, stress and internal variable results of the elasto-visco-plastic case of the strip drawing model. Because plasticity is considered
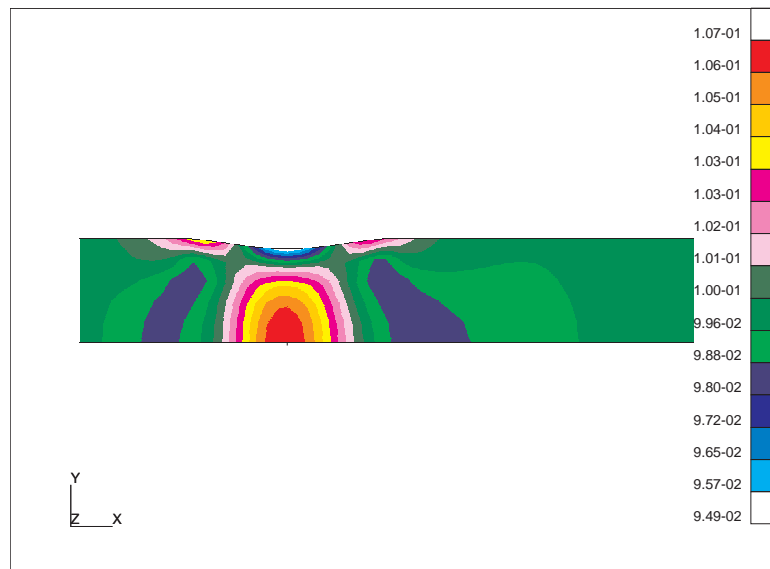
Fig. 2.14.   X Component Velocity of Eulerian Analysis (Plastic Case): Unit[mm/s]
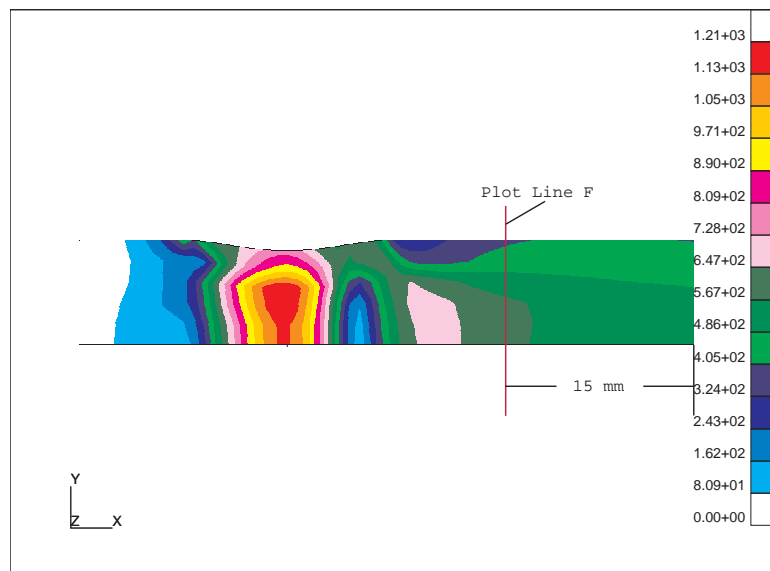
Fig. 2.15.   Von Mises Stress of Eulerian Analysis (Plastic Case): Unit[MPa]
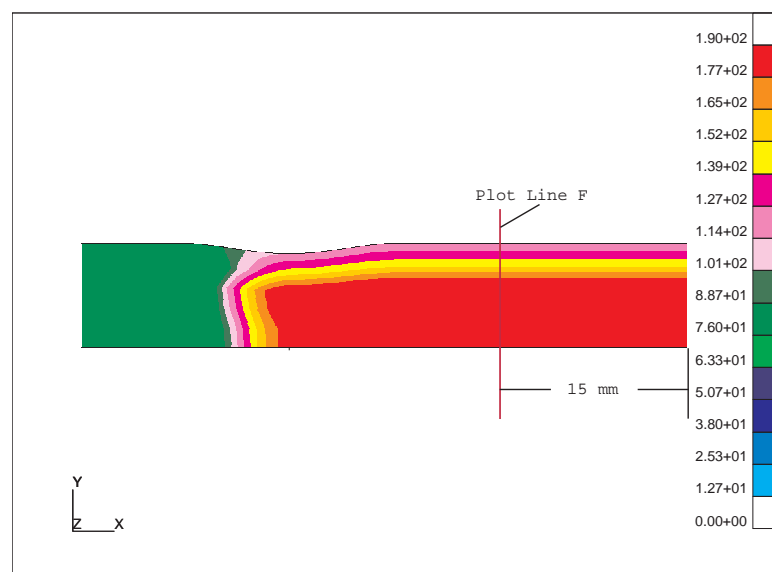
Fig. 2.16.   Internal Variable of Eulerian Analysis (Plastic Case): Unit[MPa]

in this case, the material does not rebound to it's ordinal configuration and stress state on the outlet boundary. So the velocity and stress results on the outlet boundary are different from the inlet boundary.
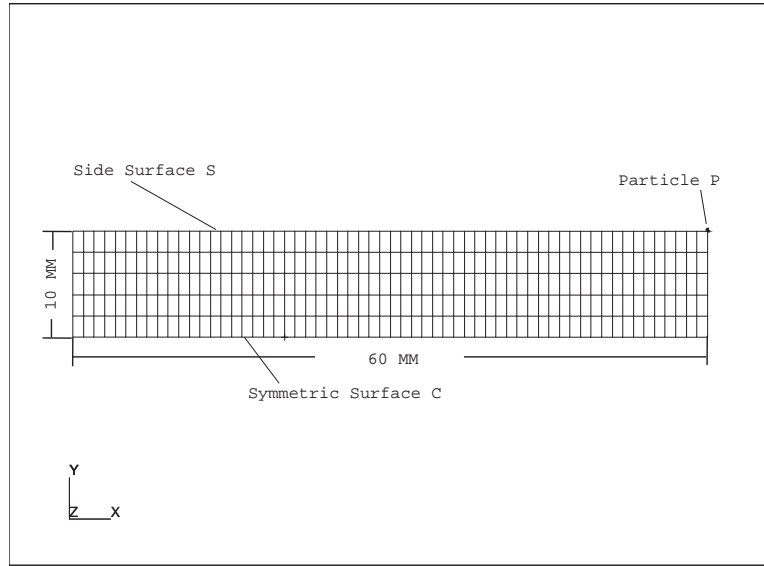
Fig. 2.17. Strip Drawing Model In Lagrangian Frame

To verify the elasto-visco-plastic results in the Eulerian frame, we can also simulate the strip drawing model in the Lagrangian frame with small time increments and compare the results with those form the Eulerian frame. Figure 2.17 shows the Lagrangian strip drawing model, the material has the same length, thickness and material properties as in the Eulerian model. The Material moves along the X direction. The Y direction displacement of the symmetric surface C is constrained to zero. To simulate the same process in both frames, the displacement of the side surface S in the Lagrangian

analysis is computed based on the velocity results from the Eulerian analysis. In a quasi-steady state process, the streamline is identical to the pathline, therefore the particles in the side surface S will go along the side curve, which consists of the side surface E and the die surface D in the Eulerian strip drawing model shown in Figure 2.11. Using the streamline integration method discussed in Reference [32], the displacement of the particles in the side surface S can be determined. The X and Y displacement of the particle P as a function of time is shown in Figure 2.18.
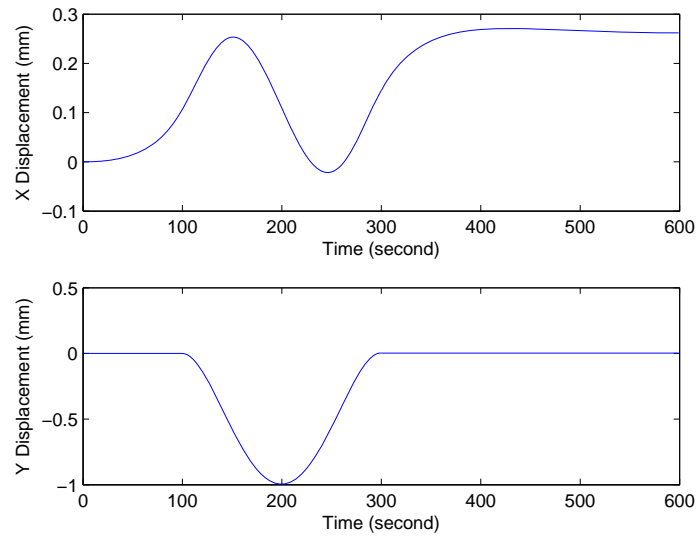
Fig. 2.18. X and Y Displacement of the Particle P

Figures 2.19 and 2.20 show the contour plots of the stress and internal variable results of the Lagrangian analysis. The Lagrangian results are similar to the Eulerian results illustrated in Figures 2.15 and 2.16. Comparison plots of the Mises stress and
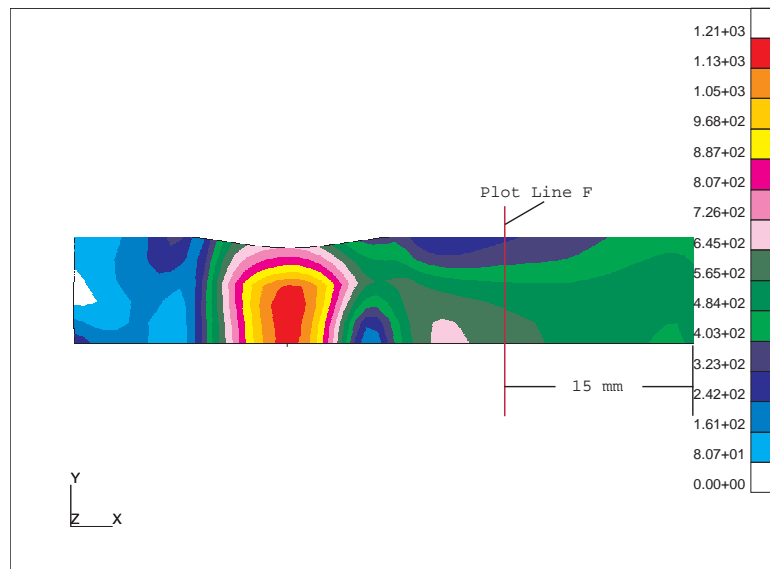
Fig. 2.19.   Von Mises Stress of Lagrangian Analysis (Plastic Case): Unit[MPa]
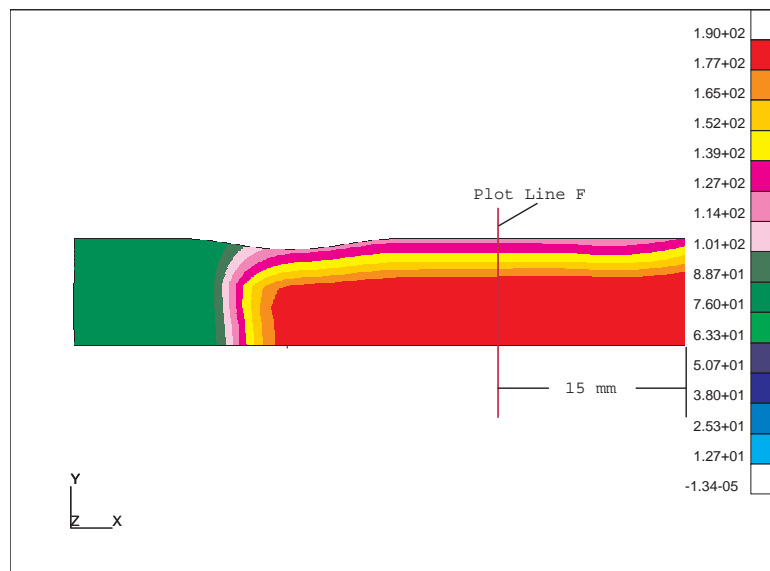
Fig. 2.20.   Internal Variable of Lagrangian Analysis (Plastic Case): Unit[MPa]

internal variable results of both analysis methods along line F, shown in Figure 2.11, are shown in Figures 2.21 and 2.22. From the above plots, we can conclude that the Eulerian elasto-visco-plastic analysis provides almost the same results as the Lagrangian analysis. The Mises stress of the elasto-visco-plastic analysis along line F denotes the residual stress of the strip drawing process. Therefore, the Eulerian elasto-visco-plastic formulation presented in this paper can accurately predict the residual stress of a quasi-steady state process.
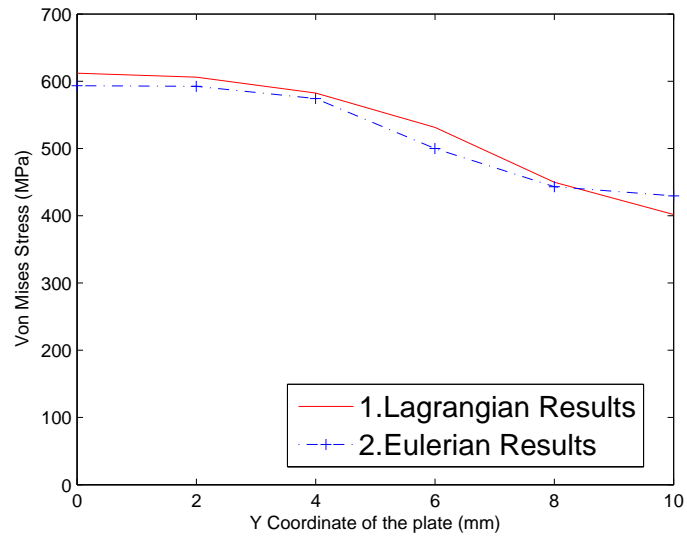
Fig. 2.21. Comparison of Von Mises Stress Results
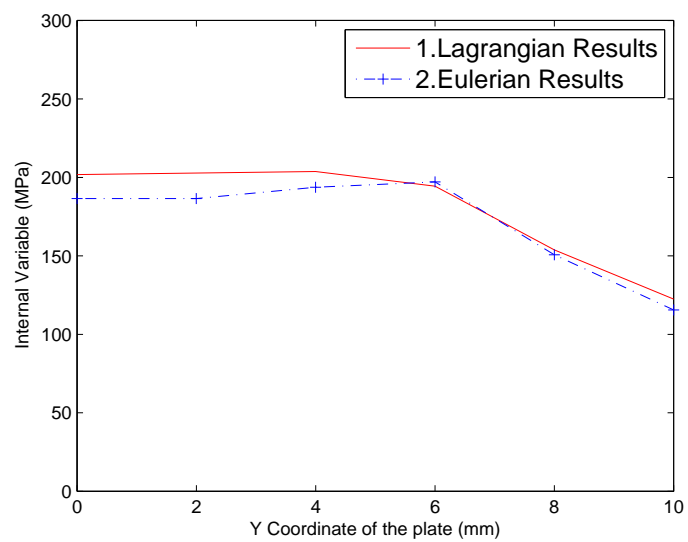
Fig. 2.22.   Comparison of the Internal Variable Results

2.6 Summary

A new four-field (velocity, stress, deformation gradient and internal variable) mixed Eulerian elasto-visco-plastic formulation suitable for modeling deformation, material state, and residual stress in quasi-steady processes has been presented in this paper. The rate-dependent Anand's constitutive equation is implemented allowing a smooth transition from mostly elastic to actively yielding response. A progressively stiffening algorithm of the plasticity rate equation is proposed to compute trial solutions within the convergence radius of the Newton Raphson method.

A radial flow and a strip drawing example are modeled to verify the formulation. The radial flow example demonstrates the effectiveness of the streamline upwind Petrov-Galerkin stabilization method, and the strip drawing example demonstrates the accuracy of the elaso-visco-plastic Eulerian formulation.

Chapter 3

Elasto-Visco-Plastic Analysis of Welding Residual Stress

3.1 Introduction

In thermo-mechanical processes, such as welding, laser forming and cladding, large tensile stresses remain near the pass of the torch, balanced by lower compressive residual stresses elsewhere. Tensile residual stresses may reduce the performance or cause fatigue and brittle failure of manufactured structures. Compressive residual stresses may cause excessive buckling distortion. Therefor, it is important to know the distribution of residual stress of welded structures in detail.

In the past three decades, welding residual stress have been extensively studied by both experimental and numerical methods. Several experimental methods have been developed to measure residual stresses. They include non-destructive methods, such as X-ray diffraction [57], neutron diffraction [58], and destructive methods, for example slicing [59], boring and hole drilling [60]. Numerical methods for the estimation of residual stress have involved performing weakly coupled thermal-mechanical finite element methods [15, 61, 14, 62, 13, 23, 63, 64]. Nearly all researches have assumed rate-independent

elasto-plastic material response, which is most appropriate at low to moderately elevated temperatures. At high temperatures, the material response becomes rate dependent and an elasto-visco-plastic model would be more suitable. However, limited work is published on the effect of rate dependent in residual stress computation [14].

Typically, the residual stress computations are performed on Lagrangian reference frames, as illustrated in Figure 3.1 case A, where the reference frame is stationary and the welding torch travels in time. With the exception of the work of Brown *et al.* [23], most investigors assume that the deformation has very small effect on the temperature distribution. Therefore a heat transfer analysis is performed first, followed by a mechanical analysis using the temperature results as a thermal loading. In Lagrangian reference frames both thermal and mechanical analyses are performed in a time incremental scheme to model the traveling welding torch. For large 3D models the hundreds or thousand of time increments [24] may be required resulting in a very high computational cost.

In 1989, Stuart B. Brown, Kwon H. Kim and L. Anand [37] proposed a rate-dependent constitutive equation to describe the plastic evolution of metals at high temperatures. The model is commonly known as Anand's model and unlike the rate independent elasto-plastic model it does not exhibit a sharp transition from elastic to plastic response. In Anand's model, both elastic and plastic deformation simultaneously evolve at all stress levels. At low stresses compared to an internal variable analogous to the yield stress in elasto-plasticity, the deformation is mostly elastic. As the stress increases the rate of plastic deformation increases following a sinh curve of the ratio of equivalent stress
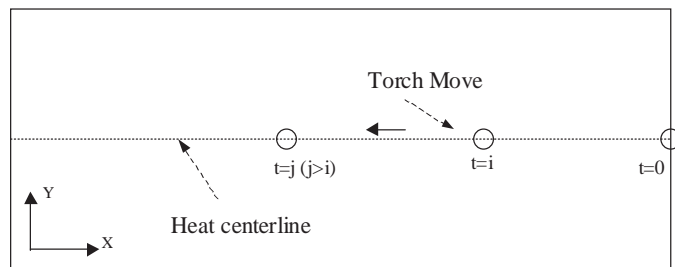
A. Lagrangian Frame
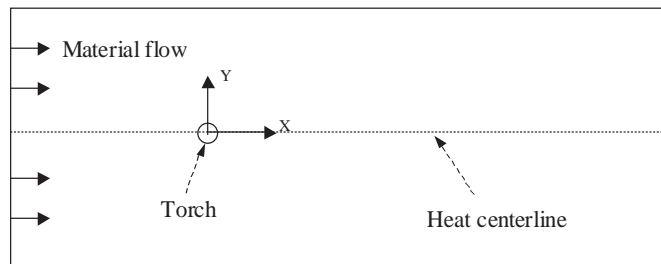
B. Eulerain Frame

Fig. 3.1.   Lagrangian and Eulerian Reference Frame

to internal variable. Weber and Anand also developed a radial return iterative method suitable for a time incremental Lagrangian implementation of their model [49, 50].

Nguyen et al. [25] proposed that several industrial metal forming processes, such as welding, rolling and extrusion can be treated as a quasi-steady state process in an Eulerian frame. As the case B shown in Figure 3.1, an Eulerian frame is attached to the torch and the material is entering the analysis domain through the inlet surface. Application of an Eulerian reference frame in modeling welding residual stress has the potential to reduce computational cost in modeling arc welding processes, since it is a steady state analysis as compared to the common time incremental Lagrangian analyses. An Eulerian reference frame is also more advantageous in modeling material movement in friction stir welding processes, since excessive mesh distortion and re-meshing are no issues as the case of Lagrangian models [65].

Shanghvi and Michaleris [66] developed a displacemnt based Eulerian elasto-plastic model for thermo-mechanical processes. The model was used to compute both distortion and residual stress in laser forming. However, convergence was not stable in modeling welding. Yu and Thompson [35] proposed an Eulerian method using the rate of equilibrium equation which can solve pure elastic cases. However, the model does not consider the plastic material flow during active plasticity. Maniatty et al. [44] developed an elasto-visco-plastic Eulerian method using Anand's model to solve large strain rate problems, such as rolling and extrusion. However, this model does not handle low strain rate problems such as arc welding, and can not compute residual stress. Recently, Qin and Michaleris [34] developed a Galerkin Eulerian formulation with four unknown fields (velocity, stress, deformation gradient and internal variable) to predict residual stress of

elasto-visco-plastic materials using Anand's model. The model has been demonstrated in material rolling applications.

The objective of this work is twofold: 1) evaluate the suitability of Anand's elasto-visco-plastic model in computing welding residual stress and 2) investigate the feasibility of an Eulerian implementation of Anand's model in modeling welding residual stress. A Gas Metal Arc Welding (GMAW) case with available experimental residual stress measurement is used as test case. To address the first objective, a Lagrangian implementation of Anand's elasto-visco-plastic model is performed and the computed residual stress are compared against results from the conventional rate-independent elasto-plastic model implemented in the same Lagrangian reference frame. To address the second objective, the Eulerian implementation of Anand's model as developed in Reference [34] is applied to the same GMAW test case and computed residual stress are compared against results computed by the Lagrangian models of the first objective. Implementation of the Anand's model in modeling friction stir welding is the focuss of current research. Preliminary results are available in Reference [42]. Detailed results will be available in future publications.

3.2 Lagrangian Analysis

In this section, the governing equations for thermal and mechanical analyses using both elasto-plastic and elasto-visco-plastic constitutive models for a Lagrangian implementation are briefly summarized. Detail presentations are available in References [67] and [49].

3.2.1 Thermal Analysis

The thermal analysis in a Lagrangian frame is performed in an incremental scheme. For a stationary reference frame $\mathbf{r}$ fixed to the material at time t, the governing equation for transient heat transfer analysis is:

$$\rho C_p \frac{dT}{dt}(\mathbf{r}, t) = -\frac{\partial q_i(\mathbf{r}, t)}{\partial r_i} + Q_t(\mathbf{r}, t) \tag{3.1}$$

where ρ is the density of the flowing body, C_p is the specific heat capacity, T is the temperature, Q_t is the internal heat generation rate and q_i is the heat flux vector which can be obtained by:

$$q_i = -k\frac{\partial T}{\partial x_i} \tag{3.2}$$

where k is the temperature-dependent thermal conductivity.

The initial temperature field is given by

$$T = T^0 \qquad \text{in the entire volume } V \tag{3.3}$$

where T^0 is the prescribed initial temperature.

The boundary conditions applied on the surface are:

$$T(\mathbf{r}, t) = \bar{T}(\mathbf{r}, t) \qquad \text{on the surface } A_{\mathbf{r}}^T \tag{3.4}$$

$$q^p_i(\mathbf{r}, t) \quad = \quad \bar{q}^p_i(\mathbf{r}, t) \qquad\qquad \text{on the surface } A^q_{\mathbf{r}} \qquad\qquad (3.5)$$

where, $\bar{T}$ and $\bar{q}^p$ represent the prescribed temperature and temperature-dependent surface flux, respectively. The surface flux q^p is evaluated by the projection of the heat flux q_i, normal to the surface,

$$q^p_i(\mathbf{r}, t) = q_i(\mathbf{r}, t) \cdot n_i(\mathbf{r}) \qquad\qquad \text{on any surface } A \qquad\qquad (3.6)$$

where $\mathbf{n}$ is the unit outward normal to the surface A.

3.2.2 Mechanical Analysis

Finite element analysis of manufacturing processes in Lagrangian reference frames has typically used either elasto-plastic [67] or elasto-viscoplastic constitutive models [49, 50]. Both sets of the formulations are presented in this section for comparison purposes.

For each time increment, the following equilibrium equation is solved:

$$\frac{\partial \sigma_{ij}}{\partial x_i} + b_j = 0 \qquad \text{in } V_{\mathbf{r}} \qquad\qquad (3.7)$$

where $\boldsymbol{\sigma}$ is the stress, and $\mathbf{b}$ is the body force. The boundary conditions are:

$$u_i(\mathbf{r}, t) \quad = \quad \bar{u}_i(\mathbf{r}, t) \qquad \text{on surface } A^u_{\mathbf{r}} \qquad\qquad (3.8)$$

$$\sigma_{ij}(\mathbf{r}, t) \cdot n_i(\mathbf{r}, t) \quad = \quad \bar{t}_j(\mathbf{r}, t) \qquad \text{on surface } A^t_{\mathbf{r}} \qquad\qquad (3.9)$$

where, $\bar{u}(\mathbf{r}, t)$ are the prescribed displacements on surface $A_{\mathbf{r}}^{u}$, $\bar{\mathbf{t}}$ are the prescribed tractions on surface $A_{\mathbf{r}}^{t}$, and n is the unit outward normal to the surface $A_{\mathbf{r}}^{t}$.

3.2.2.1 Elasto-Plastic model

The stress strain relationship for the elasto-plastic model is:

$$\sigma_{ij} = C_{ijkl} (E_{kl} - E_{kl}^{p} - E_{kl}^{t}) \tag{3.10}$$

where, C_{ijkl} is the fourth order elasticity tensor, E_{ij}, E_{ij}^{p} and E_{kl}^{t} are the total, plastic and thermal strain, respectively. Using associative J_2 plasticity [68], the yield function f^{yeild} and the evolution equation for equivalent plastic strain $\tilde{\varepsilon}^{p}$ are:

$$f^{yeild} = \tilde{\sigma} - \sigma_{Y} (\tilde{\varepsilon}^{p}, T) \tag{3.11}$$

$$\dot{\tilde{\varepsilon}}^{p} = \sqrt{\frac{2}{3}} \| \dot{E}_{ij}^{p} \| \tag{3.12}$$

where, $\tilde{\sigma}$ and H are the Mises stress and isotropic material hardening, respectively. Active yielding occurs when $f^{yeild} = 0$. The evolution equation for active yielding is

$$\dot{f}^{yeild} = 0 \tag{3.13}$$

3.2.2.2 Anand's Elasto-Viscoplastic model

For Anand's rate-dependent model, the stress evolution equation is:

$$\overset{\nabla}{\sigma}_{ij} = C_{ijkl} (D_{kl} - D^p_{kl} - D^t_{kl}) \tag{3.14}$$

where, D_{ij}, D^p_{ij} and D^t_{ij} are the rate of total, plastic and thermal strain tensor, respectively. The Jaumann derivative of Cauchy stress $\overset{\nabla}{\sigma}_{ij}$, rate of strain tensor D_{ij}, and rate of plastic strain tensor D^p_{ij} can be derived as:

$$\overset{\nabla}{\sigma}_{ij} = \dot{\sigma}_{ij} - W_{ik}\sigma_{kj} + \sigma_{ik}W_{kj} \tag{3.15}$$

$$D_{ij} = \frac{1}{2}\left(L_{ij} + L_{ji} \right) \tag{3.16}$$

$$D^p_{ij} = \sqrt{\frac{3}{2}}\dot{\bar{\varepsilon}}^p N_{ij} \tag{3.17}$$

The velocity gradient tensor L_{ij}, spinning tensor W_{ij} and equivalent plastic strain rate $\dot{\bar{\varepsilon}}^p$ are:

$$L_{ij} = \frac{\partial v_i}{\partial x_j} \tag{3.18}$$

$$W_{ij} = \frac{1}{2}\left(L_{ij} - L_{ji} \right) \tag{3.19}$$

$$\dot{\bar{\varepsilon}}^p = f(\tilde{\sigma}, s) \tag{3.20}$$

The evolution equation for the internal variable s in Equation (3.20) can be expressed as:

$$\dot{s} = g(\tilde{\sigma}, s) \qquad (3.21)$$

Functions $f(\tilde{\sigma}, s)$ and $g(\tilde{\sigma}, s)$ in Equations (3.20) and (3.21) are constitutive functions, which are defined in Section 3.4.1.

3.3 Eulerian Analysis

The Eulerian expressions of the quasi-steady state thermal and elasto-viscoplastic mechanical analysis are summarized in this section. Detailed explanations of these equations are presented in References [53] and [34].

3.3.1 Thermal Analysis

For a quasi-steady state problem, the transient heat transfer analysis of Equation (3.1) reduces to a boundary value problem in an Eulerian frame [69, 70, 71, 72],

$$\rho \, C_p \, v_i \, \frac{\partial T}{\partial x_i} = -\frac{\partial q_i}{\partial r_i} + Q_t \qquad (3.22)$$

along with strongly enforced boundary condition:

$$T = T^0 \qquad \text{On the inlet surface} \qquad (3.23)$$

3.3.2 Mechanical Analysis

A coupled four-field (Velocity $\mathbf{v}$, Stress $\boldsymbol{\sigma}$, Deformation gradient $\mathbf{F}$ and Internal variable s) Eulerian formulation [34] using Anand's model is used to transform the elasto-viscoplastic initial boundary value problem of Section 3.2.2.2 to a static boundary value problem. The governing equations of this method are:

- Rate Equilibrium Equation

$$\frac{d}{dt}\left[\frac{\partial \sigma_{ij}}{\partial x_i}\right] = \frac{\partial P_{ij}}{\partial x_i} = 0 \tag{3.24}$$

- Strain Integration Equation

$$\dot{F}_{ij} = v_k \frac{\partial F_{ij}}{\partial x_k} = L_{ik} F_{kj} \tag{3.25}$$

- Internal Variable Evolution Equation

$$\dot{s} = v_k \frac{\partial s}{\partial x_k} = g(\tilde{\sigma}, s) \tag{3.26}$$

- Stress Strain Relationship

$$\dot{\sigma}_{ij} = v_k \frac{\partial \sigma_{ij}}{\partial x_k} = C_{ijkl} \dot{E}^e_{kl} \tag{3.27}$$

The rate equilibrium Equation (3.24) is presented by Thompson and Yu [35]. σ_{ij} in (3.24) is the Cauchy stress tensor and P_{ij} can be defined by:

$$P_{ij} \equiv v_k \frac{\partial \sigma_{ij}}{\partial x_k} - \frac{\partial v_i}{\partial x_k}\sigma_{kj} + \frac{\partial v_k}{\partial x_k}\sigma_{ij} \qquad (3.28)$$

The tensor F_{ij} in Equation (3.25) is the deformation gradient tensor and the velocity gradient tensor L_{ij} is defined in Equation (3.18). The internal variable evolution Equation (3.26) is proposed in Reference [49]. In Equation (2.8), $\dot{E}^e_{kl}$ is the rate of elastic strain tensor:

The corresponding boundary conditions are:

$$v_i = v_i^p \quad on \ \partial B_v \qquad (3.29)$$

$$n_i \cdot P_{ij} = t_j^p \quad on \ \partial B_P \qquad (3.30)$$

$$\sigma_{ij} = \sigma_{ij}^p \quad on \ \partial B_\sigma \qquad (3.31)$$

$$F_{ij} = F_{ij}^p \quad on \ \partial B_F \qquad (3.32)$$

$$s = s^p \quad on \ \partial B_s \tag{3.33}$$

where, v_i^p, σ_{ij}^p, F_{ij}^p, $\hat{s}_i^p$ and $\dot{t}_i^p$ are the velocity, stress, deformation gradient, internal variable and rate of traction specified on the boundary, respectively; n_i is the unit outward normal vector on the boundary ∂B. For more detail of this method, please refer to Reference [34].

3.4   Gas Metal Arc Welding Model

A single-pass Gas Metal Arc Welding (GMAW) process, which has the same welding conditions as the experimental weld in Reference [6], is modeled under both Eulerian and Lagrangian frames to verify the usability and accuracy of the Eulerian analysis. Two 28×9 inch (711.2×228.6 mm) HSLA-65 steel plates with $1/4$ inch ($6.35mm$) thickness are welded together, as shown in Figure 3.2. The moving velocity of the torch is $2.54 \ mm/s$ along the weld centerline and the heat input of the torch is $28.6 \ KJ/inch$. 2D in-plane models are used for both Lagrangian and Eulerian analyses. To eliminate the end effects, the Lagrangian model is longer ($L = 1300mm$) than the actual plates. The Eulerian model is even longer ($L = 3000mm$) to allow for sufficient cooling. Figures 3.3 and 3.4 show the Lagrangian and Eulerian model, respectively. The Lagrangian GMAW model is discretized into 1500 4-node quadrilateral elements with biased smaller element size at the welding region and the same element size alone the welding direction. The Eulerian GMAW model is discretized into 1776 4-node quadrilateral elements with refined mesh around the welding torch.
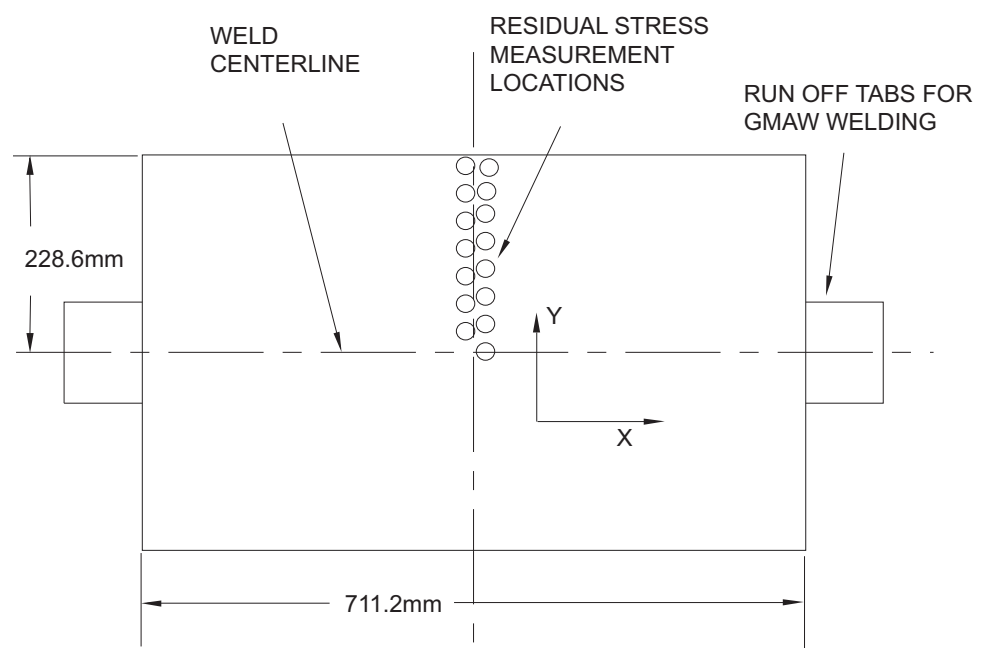
Fig. 3.2. Geometry of measured plate.
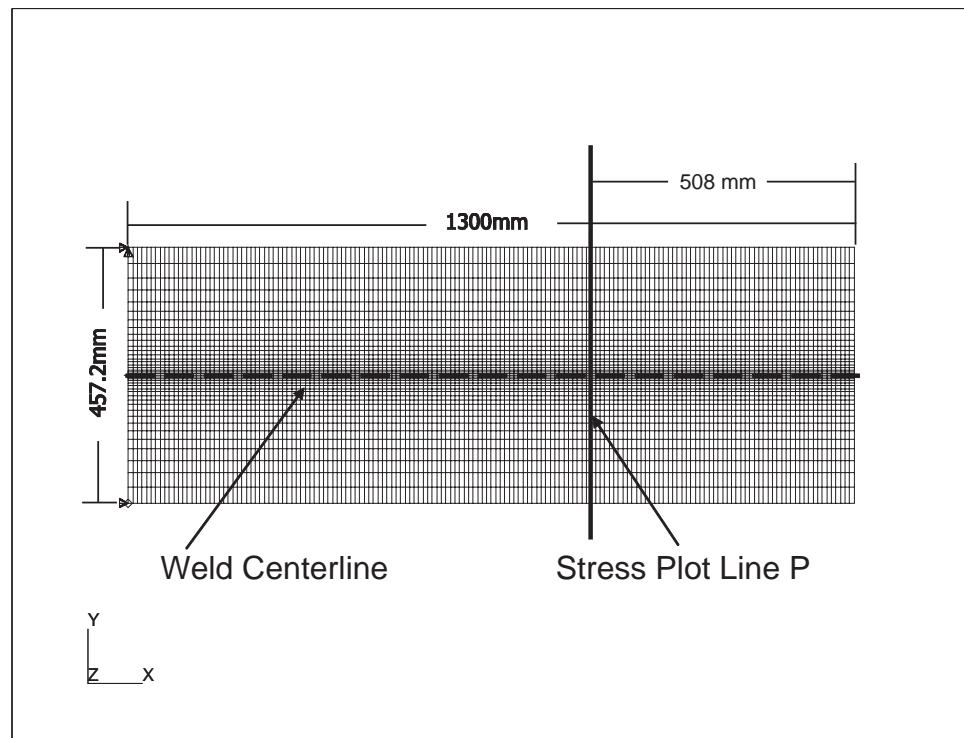
Fig. 3.3.   Gas Metal Arc Welding Model (Lagrangian): Unit[mm]
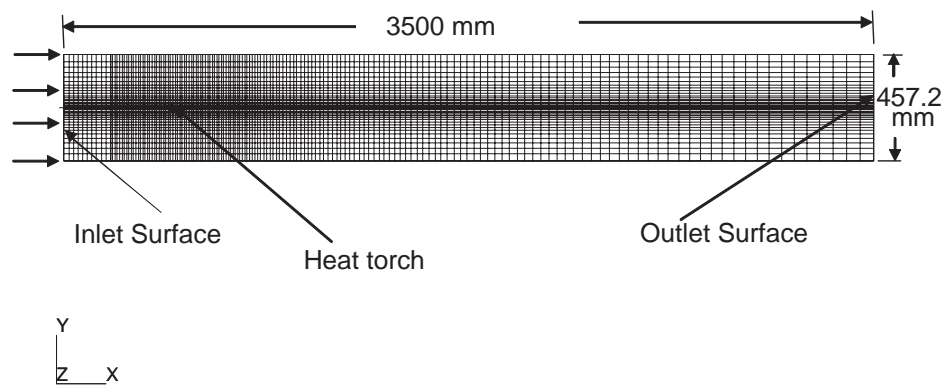
Fig. 3.4.   Gas Metal Arc Welding Model (Eulerian): Unit[mm]

The heat flux distribution of the electric arc is modeled as a Gaussian distribution [62],

$$q = \frac{3\eta Q}{\pi R^2} \left[e^{-3\left((\frac{x}{R})^2 + (\frac{y}{R})^2 \right)} \right] \tag{3.34}$$

where η is the torch efficiency, Q is the input power, R is the torch radius, and x and y are the distances of a point from the center of the laser beam. The radius R is $10mm$ and the torch efficiency η is taken as 0.8.

	Reference Frame	Constitutive law	Elastic Properties
Case 1	Lagrangian	Elasto-plastic	Temperature dependent
Case 2	Lagrangian	Anand's model	Temperature dependent
Case 3	Lagrangian	Anand's model	Constant
Case 4	Eulerian	Anand's model	Constant

Table 3.1. Analysis models for Gas Metal Arc Welding

Four cases of GMAW are simulated in this section, as listed in Table 3.1. Case 1 is the traditional Lagrangian analysis using an elasto-plastic model, which has been very widely used and has been shown to effectively predict residual stress. In case 2, the Anand's elasto-visco-plastic model is implemented in a Lagrangian frame and compared to the elasto-plastic model to evaluate the usability of the model at low strain rates (less then 10^{-3} sec^{-1}). Because the Eulerian analysis assumes that the elastic material properties do not change with temperature, case 3 is a Lagrangian implementation of Anand's model with constant elastic properties to estimate the effect of elastic property

temperature dependence on the residual stress computation. Case 4 is the Eulerian analysis in Anand's elasto-visco-plastic model.

3.4.1   Constitutive Law and Material Properties
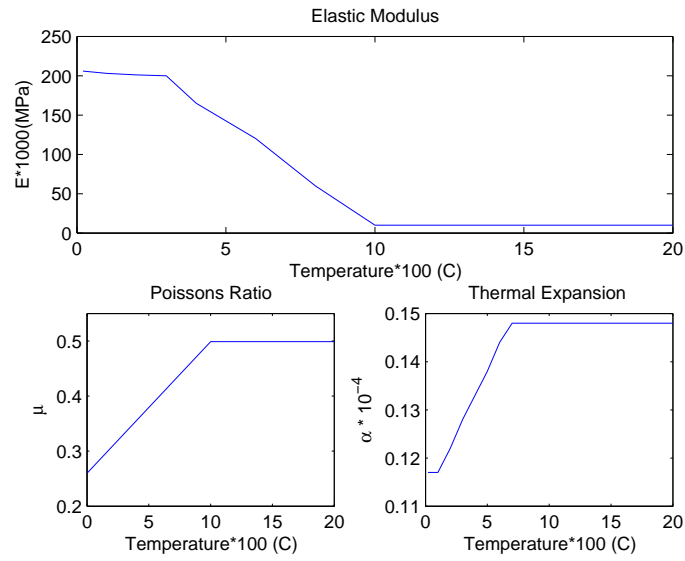
Fig. 3.5.   Material Properties

The material properties of HSLA-65 steel under different temperatures used in case 1 and 2 are plotted in Figure 3.5. In cases 3 and 4, the elastic properties at room temperature $(T = 20^{\circ}C)$ are used. The function $f(\tilde{\sigma}, s)$ in Equation (3.20) is taken to be [37]:

$$f \;=\; A\left(sinh\left(\xi\frac{\tilde{\sigma}}{s}\right)\right)^{\frac{1}{m}} \tag{3.35}$$

where $A = A_0 \cdot exp(-Q/(R*(300 + (T-300)/T^a)))$, Q is the thermal activation energy, R is the ideal gas constant, T is the absolute temperature and T^a is a temperature dependent parameter, which can be expressed as:

$$T^a = \begin{cases} \sqrt{25 - (\frac{T-300}{100})^2} + 1 & T \leq 800K \\ 1 & T > 800K \end{cases} \tag{3.36}$$

The value of material parameters A_0, ξ and m is listed in Table 2.1.

The internal variable evolution equation, defined by the function $g(\tilde{\sigma}, s)$, is [37]:

$$g(\tilde{\sigma}, s) = h_0 \left|\left(1 - \frac{s}{s^*}\right)\right|^a sigh\left(1 - \frac{s}{s^*}\right) \cdot A\left(sinh\left(\xi\frac{\tilde{\sigma}}{s}\right)\right)^{\frac{1}{m}} \tag{3.37}$$

$$s^* = \tilde{s}\left(\frac{\dot{\tilde{\varepsilon}}^{vp}}{A}\right)^n \tag{3.38}$$

where h_0, a, s and n are the material parameters listed in Table 2.1.

Material Parameter	Value	Material Parameter	Value
A_0	$6.34 * 10^{11} sec^{-1}$	Q	352.35 KJ/mole
ξ	3.25	R	8.314
m	0.1956	a	1.5
n	0.06869	$\tilde{s}$	125.1 MPa
s_0	80 MPa	h_0	3093.1 MPa

Table 3.2.   Material Parameters for HSLA-65 steel

The HSLA-65 steel with strain rate between 10^{-3} and 10^{-4} is considered in this work. The material properties listed in Table 2.1 are determined based on the experimental stress-strain plot of the HSLA-65 steel shown in Reference [55]. Using the radial-return algorithm presented in Reference [56], the computed stress-strain relationships of the HSLA-65 under different temperatures using Anand's model are shown in Figure 3.6.

3.4.2   Evaluaton of Anand's model

To compute the residual stress in a Lagrangian frame, the plate should be cooled down to room temperature, therefore a sufficiently long analysis time ($t = 1200s$) is performed. Figures 3.7 and 3.8 show the contour plots of the longitudinal component of the residual stress computed by the elasto-plastic model (Case 1) and Anand's model (Case 2), respectively. The results are very similar. To compare the results more quantitatively, lines 1 and 2 of Figure 3.9 plot the Longitudinal component residual stress of Cases 1 and 2 along line P in Figure 3.3. The difference between the two lines isvery small. The experimental results, which are listed in Reference [6], are also plotted in Figure 3.9. Line 5 shows the top side stress, line 6 plots the bottom side stress, and line 7 plots the average through thickness stress of the plate. The tensile stress of both computational and experimental results decrease sharply from the weld centerline to approximately 62 mm away from the centerline and then become compressive. At the free edge of the plate the computed compressive stress for all cases are close to the measured stress. Because an in-plane 2-D model is used to simulate GMAW, these models can not show the though thickness stress distribution.
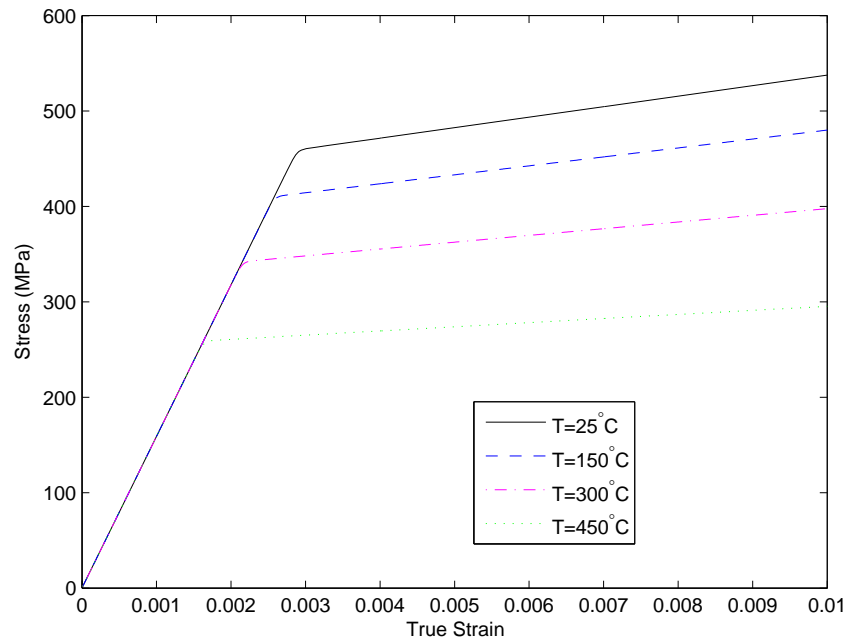
Fig. 3.6.   Stress-Strain Curves of HSLA-65 Steel Under Different Temperature
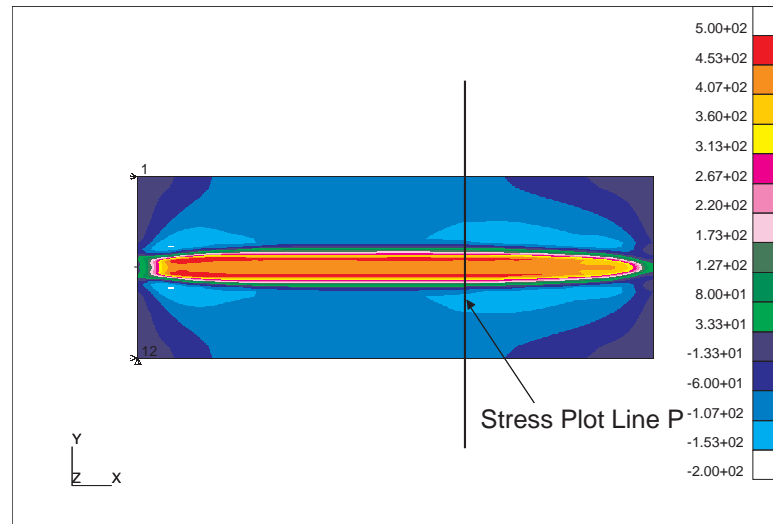
Fig. 3.7.   Lagrangian Longitudinal residual stress for elasto-plastic model (Case 1)
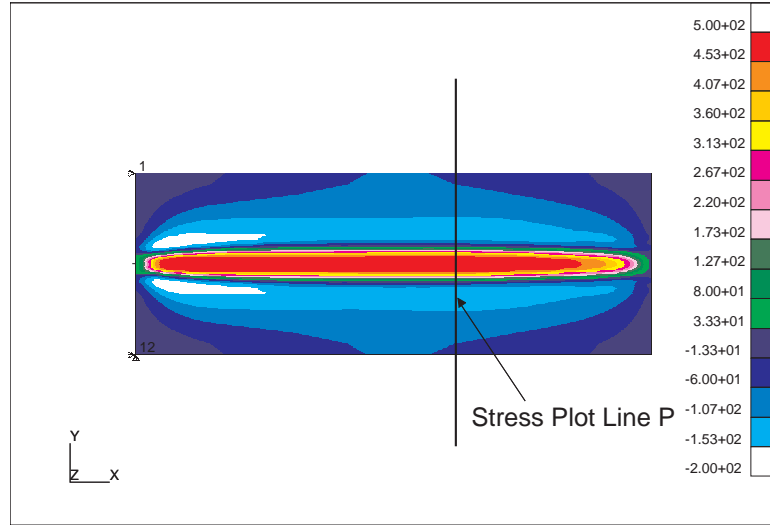
Fig. 3.8.   Lagrangian Longitudinal residual stress for Anand's model (Case 2)

The longitudinal component of the residual stress of Anand's model with constant elastic properties (case 3) is also plotted in Figure 3.9 (line 3). The residual stress computed using constant elastic properties is very close to that computed using temperature dependent elastic properties (line 2). Therefore, the residual stress computed by Anand's model is not sensitive to the temperature variation of the elastic material parameters (α, μ and E).

3.4.3   Evaluation of Mechanical Analysis in Eulerian Frame

Similarly to the Lagrangian analysis, an Eulerian thermal analysis is performed first, and the temperature result is used by the mechanical analysis. To compare the Eulerian analysis with the Lagrangian analysis, the heat torch is located at $2540mm$ from the outlet surface, Thus the distance between the torch and the outlet surface is
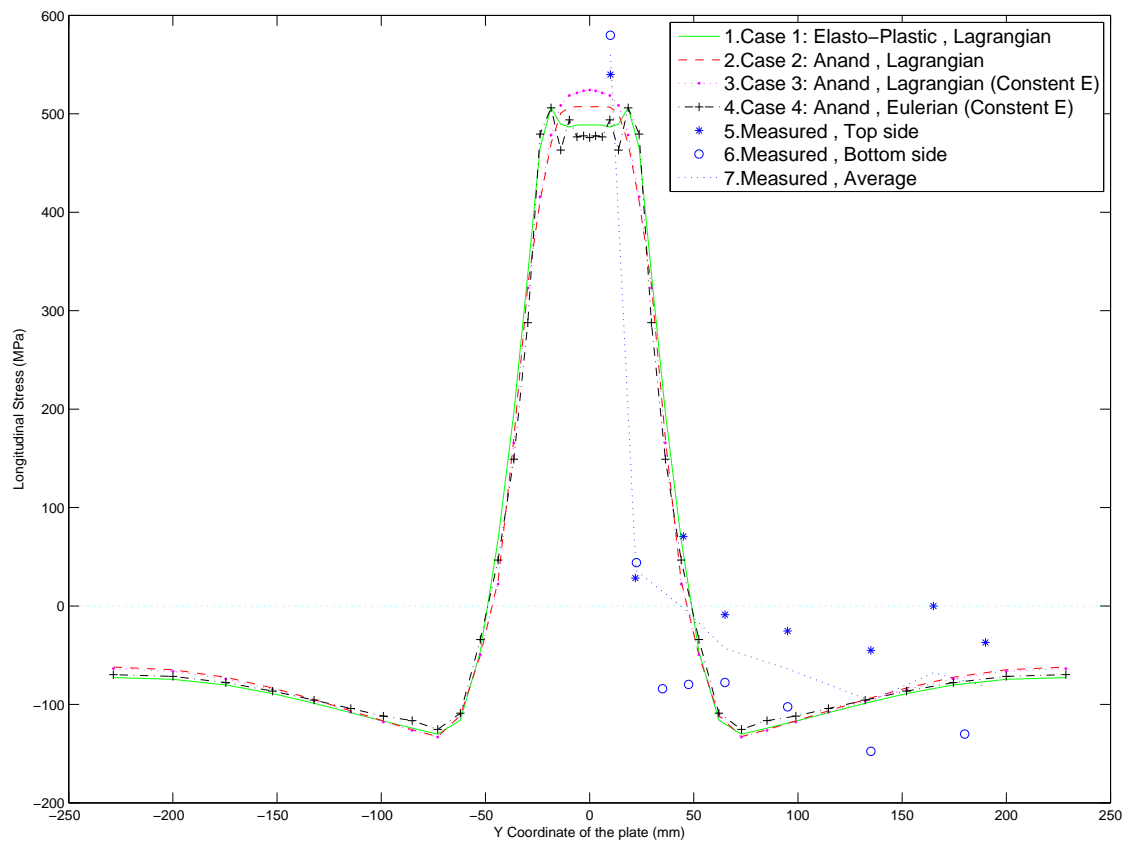
Fig. 3.9.   Comparison of Longitudinal residual stress

the same as the distance between the torch and the plot line P in Lagrangian analysis at $t = 1200s$. As shown in the contour plot of temperature result of Eulerian analysis in Figure 3.10, the temperature at the outlet surface has dropped to room temperature, thus the computed stress at the outlet surface denotes the residual stress of the welded plate.

The following boundary conditions are applied to the inlet surface of the model:

$$v_x = v_{in} = 2.54mm/s \tag{3.39}$$

$$v_y = 0 \tag{3.40}$$

$$\sigma_{ij} = 0 \tag{3.41}$$

$$F_{ij} = \delta_{ij} \tag{3.42}$$

The material properties used in the Eulerian analysis are: Elastic Modulus $E = .206 * 10^6 Mpa$, Poisson's Ratio $\mu = 0.3$ and thermal expansion $\alpha = .117 * 10^{-4}$. The yield stress still varies with temperature, as shown in Figure 3.6. The contour plot of the longitudinal residual stress of the Eulerian analysis is shown in Figure 3.11. The longitudinal residual stress along the outlet surface is also plotted in line 4 of Figure 3.9. The elasto-vsicoplastic Eulerian results (Case 4) show excellent agreement with the results from Lagrangian analysis with both elasto-plastic model (Case 1) and Anand's elasto-vsicoplastic model (Case 2). Only in the small region near the weld center line ($|Y| < 18mm$), the residual stress results have noticeable difference between the Lagrangian analysis (Case 3) and the Eulerian analysis (Case 4). The maximum difference is about 50MPa, which means the relative difference in this region is about 10%. In the
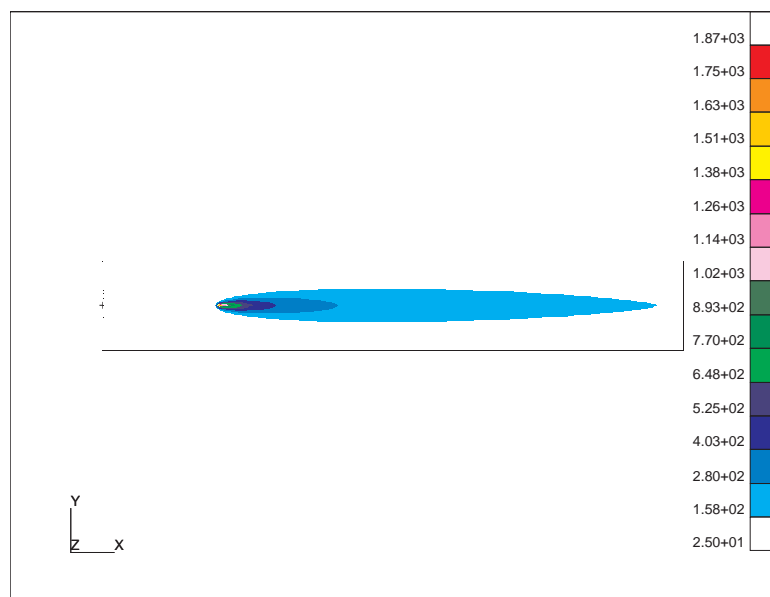
Fig. 3.10.   Temperature Distribution of Gas Metal Arc Welding in an Eulerian Frame

other regions ($18 \leq |Y| \leq 228.6mm$), the relative difference between Lagrangian analysis (Case 3) and the Eulerian analysis (Case 4) is less than 5%.
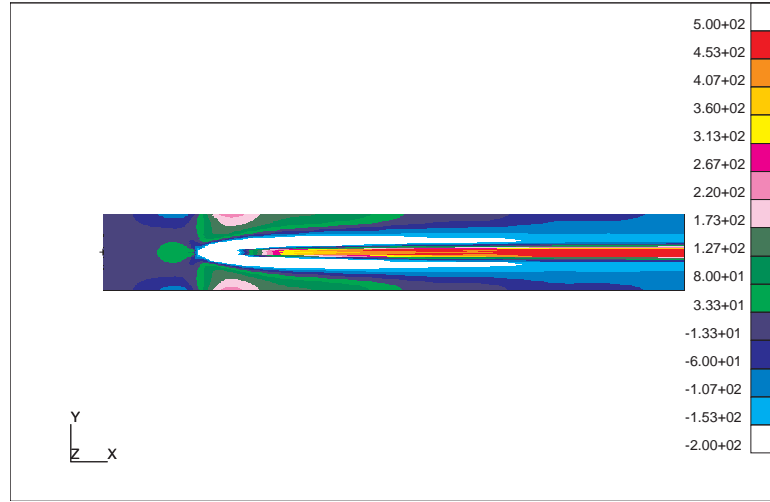
Fig. 3.11. Eulerian Longitudinal residual stress for Anand's model (Case 4)

3.4.4 Computational Cost

Both Lagrangian and Eulerian analyses are performed by an in-house finite element code which is capable to analyze coupled thermo-mechanical problems. The models are tested on an IBM RS/6000 system with 16 Gbs shared memory. The computational costs of cases 1, 2 and 4 are measured according to the CPU running time and listed in Table 3.3.

The Lagrangian implementation of the elasto-plastic and Anand's model require the same the computational time for both thermal and mechanical analysis (about 300

	Case 1	Case 2	Case 4
CPU Time for Thermal Analysis (s)	300.3	300.3	1.5
CPU Time for Mechanical Analysis (s)	236.5	280.2	333.9
Total CPU Time (s)	536.8	580.5	335.4

Table 3.3. Mechanical Analysis CPU Times

seconds). The mechanical analysis in the Eulerian frame does not show a computational advantage. This is because the Eulerian mechanical analysis uses a time consuming progressively stiffening method, which is described in Reference [34], to improve the convergence. Furthermore, the size of the element tangent matrix (44×44) for an Eulerian analysis is larger than the size (8×8) for a Lagrangian analysis. The computational cost of the Eulerian thermal analysis is only 0.5% of the Lagrangian thermal analysis. Therefore, the total computational cost for a combined thermo-mechanical analysis in an Eulerain analysis is about a half of a Lagrangian analysis.

3.5 Conclusions

An elasto-visco-plastic formulation based on Anand's constitutive model has been developed for welding residual stress modeling. The formulation has been implemented in both Lagrangian and Eulerian reference frames. Gas Metal Arc Welding has been used as a test case to verify the formulation by comparing computed residual stress against measurements and simulations using the conventional Lagrangian elasto-plastic formulations.

The proposed elasto-visco-plastic formulation when implemented in an Eulerian reference frame can account for large material deformations without the need for adaptive meshing as would be the case in a Lagrangian implementation. Therefor, it would be applicable to modeling material deformation in Friction Stir Welding. Such as implementation is the focuss of current research.

Chapter 4

Eulerian Elasto-Visco-Plastic Formulations for Residual Stress Prediction in True Equilibrium Equation

4.1 Introduction

In this work, a finite element formulation for quasi steady-state thermo-elasto-viscoplastic material is presented in an Eulerian reference frame to predict residual stress. The finite element method is a valuable tool in the modeling of forming processes, such as welding, rolling, extrusion and cladding. To predict residual stress, coupled thermo-mechanical simulations using the rate independent elasto-plastic constitutive law in Lagrangian reference frames are usually used [13, 14, 15, 16, 17, 18, 19, 20, 21, 22]. Lagrangian analysis has been shown to be accurate in solving small deformation problems with robust convergence. However, it is difficult to model problems with large element distortion, such as friction stir welding. Nguyen et al. [25] pointed out that these manufacturing processes can be treated as quasi-steady state in an Eulerian reference frame. Thus, large deformation problems can also be modeled in an Eulerian reference frame

[32, 33], by assuming the material to be an incompressible fluid flow. However, since these methods neglect the material evolution history, residual stress can not be obtained.

Qin and Michaleris [34] have developed an elasto-viscoplastic Eulerian formulation with four unknown fields (velocity ($\mathbf{V}$), stress ($\boldsymbol{\sigma}$), deformation gradient ($\mathbf{F}$) and internal variable ($\mathbf{s}$)) based on the rate equilibrium equation [35] to predict residual stress out of Eulerian reference frame. This formulation implements Anand's rate dependent constitutive law and introduces evolution equations of deformation gradient and stress to integrate total and viscoplastic strain from velocity field. Because the rate equilibrium is a function of velocity and stress, this formulation is numerically easy to be implemented. The Streamline Upwind Petrov-Galerkin (SUPG) method [38, 39, 40, 41] is used to eliminate nonphysical oscillation results may caused by convection terms in the evolution equations. The rate equilibrium formulation has also been verified to be able to obtain accurate and spatially stable results by comparing against Lagrangian analyses using an elasto-plastic constitutive model in the strip drawing model and gas metal arc welding model [34, 73]. However, the stress evolution equation neglects the $\dot{C}_{ijkl} E^e_{kl}$ term, where C_{ijkl} is the fourth order isotropic elasticity tensor and E^e_{kl} is the elastic strain tensor, because the elastic strain tensor E^e_{kl} can not be obtained from the set of equations. Thus, the rate equilibrium Eulerian method can not account for temperature variation of material properties. Moreover, the application of the traction rate boundary conditions for the rate equilibrium equation is difficult.

In this work, an improved stabilized elasto-viscoplastic Eulerian formulation based on the real equilibrium equation is presented. The velocity ($\mathbf{V}$), deformation gradient

($\mathbf{F}$), viscoplastic part of deformation gradient ($\mathbf{F}^{vp}$) and internal variable ($\mathbf{s}$) are coupled and solved together. The streamline Upwind Petrov-Galerkin (SUPG) method [38, 39, 40, 41] is also introduced to stabilize the convection terms in the evolution equations of the deformation gradient, viscoplastic part of deformation gradient and internal variable. Three numerical examples (disturbed flow, strip drawing and gas metal arc welding) are analyzed to verify the accuracy of the true equilibrium Eulerian method and to show the difference between the true equilibrium method and the rate equilibrium method.

4.2   Eulerian Formulations

Consider an isotropic, homogeneous, elasto-visco-plastic material flows steadily through a two-dimensional domain B with boundary ∂B. In this formulation, a mixed Galerkin method with the true equilibrium equation is developed, where four field variables are solved simultaneously, namely velocity ($\mathbf{V}$), total deformation gradient ($\mathbf{F}$), viscoplastic part of deformation gradient ($\mathbf{F}^{vp}$) and internal variable ($\mathbf{s}$).

4.2.1   Governing Equations

The governing equations for the boundary value problem on B are equilibrium equation, strain integration equation, viscoplastic strain integration equation and internal variable evolution equation, which are listed below.

4.2.1.1 Equilibrium equation

$$\frac{\partial \sigma_{ij}}{\partial x_i} = 0 \tag{4.1}$$

where, σ_{ij} is the Cauchy stress tensor. In this work, we assume that stress in a deformed configuration comes from both elastic deformation and viscoplasic material flow. Therefore, the stress and strain relationship can be written as:

$$\sigma_{ij} = C_{ijkl} E^e_{kl} + 2\mu D_{ij} \tag{4.2}$$

where, C_{ijkl} is the fourth order isotropic elasticity tensor, μ is the viscosity. The elastic strain tensor E^e_{ij} and the strain rate tensor D_{ij} in Equation (4.2) can be derived by:

$$E^e_{ij} = \frac{1}{2}\left(\delta_{ij} - F^{e^{-1}}_{ki} F^{e^{-1}}_{kj}\right) \tag{4.3}$$

$$D_{ij} = \frac{1}{2}\left(L_{ji} + L_{ij}\right) \tag{4.4}$$

with the velocity gradient tensor L_{ij} be:

$$L_{ij} = \frac{\partial v_i}{\partial x_j} \tag{4.5}$$

The elastic deformation gradient tensor F^e_{ij} in Equation (4.3) can be obtained by the decomposition of the total deformation gradient tensor F_{ij} as:

$$F^e_{ij} = F_{ik} F^{\theta-1}_{kl} F^{vp-1}_{lj} \tag{4.6}$$

where, F^θ_{ij} is the thermal part of the deformation gradient tensor and F^{vp}_{ij} is the viscoplastic part of the deformation gradient tensor.

4.2.1.2 Strain integration equation

To compute strain from the velocity field, the deformation gradient tensor is integrated throughout the domain [32]. The evolution equation for the total deformation gradient tensor F_{ij} is:

$$\dot{F}_{ij} = v_k \frac{\partial F_{ij}}{\partial x_k} = L_{ik} F_{kj} \tag{4.7}$$

4.2.1.3 Viscoplastic Strain integration formulation

Similarly, the evolution of viscoplastic part of the deformation gradient tensor can be expressed as:

$$\dot{F}^{vp}_{ij} = v_k \frac{\partial F^{vp}_{ij}}{\partial x_k} = D^{vp}_{ik} F^{vp}_{kj} \tag{4.8}$$

where, the viscoplastic strain rate tensor D^{vp}_{ij} is:

$$D^{vp}_{ij} = \sqrt{\frac{3}{2}}\dot{\bar{\varepsilon}}^{vp} N_{ij} \tag{4.9}$$

in which $\dot{\bar{\varepsilon}}^{vp}$ is the equivalent viscoplastic strain rate defined by the constitutive function $f(\tilde{\sigma}, s)$, which is given in Section 4.4.2, and N_{ij} is the direction of plastic flow tensor derived by:

$$\dot{\bar{\varepsilon}}^{vp} = f(\tilde{\sigma}, s) \tag{4.10}$$

$$N_{ij} = \sqrt{\frac{3}{2}}\frac{\sigma'_{ij}}{\tilde{\sigma}} \tag{4.11}$$

and the equivalent tensile stress $\tilde{\sigma}$ is defined by:

$$\tilde{\sigma} = \sqrt{\frac{3}{2}\sigma'_{ij}\sigma'_{ij}} \tag{4.12}$$

where, the Cauchy stress deviator σ'_{ij} is:

$$\sigma'_{ij} = \sigma_{ij} - \frac{1}{3}\sigma_{kk}\delta_{ij} \tag{4.13}$$

4.2.1.4   Internal variable evolution equation

The internal variable evolution equation is given by [49]:

$$\dot{s} = v_k \frac{\partial s}{\partial x_k} = g(\tilde{\sigma}, s) \tag{4.14}$$

where, s is the internal variable, $g(\tilde{\sigma}, s)$ is a constitutive function defined in Section 4.4.2.

4.3   Weak Formulations

The boundary value problem defined in Section 4.2.1 is solved by expressing the problem in a weak form and then using the finite element method to solve the resulting system. The convection terms in Equations (4.7), (4.8) and (4.14) are known to sometimes become instable and cause spurious node-to-node oscillations in the solution. The cause of this numerical instability is discussed in References [52, 53], and the streamline upwind Petrov-Galerkin method [54] is shown to effectively suppress the oscillation by adding discontinuous weighting functions to the traditional Galerkin weighting functions. In this paper, Equations (4.7), (4.8) and (4.14) are stabilized using Petrov-Galerkin-type formulations. The stabilized weak formulations are:

$$\int_V \frac{\partial \hat{v}_i}{\partial x_j} \sigma_{ij} \, dV - \int_S \hat{v}_i \, t_i^p \, dS = 0 \tag{4.15}$$

$$\int_V \left(v_k \frac{\partial F_{ij}}{\partial x_k} - L_{ik} F_{kj} \right) \left(\hat{F}_{ij} + \tau_e v_k \frac{\partial \hat{F}_{ij}}{\partial x_k} \right) dV = 0 \tag{4.16}$$

$$\int_V \left(v_k \frac{\partial F^{vp}_{ij}}{\partial x_k} - L_{ik} F^{vp}_{kj} \right) \left(\hat{F}^{vp}_{ij} + \tau_e v_k \frac{\partial \hat{F}^{vp}_{ij}}{\partial x_k} \right) dV = 0 \tag{4.17}$$

$$\int_V \left(v_k \frac{\partial s}{\partial x_k} - g(\tilde{\sigma}, s) \right) \left(\hat{s} + \tau_e v_k \frac{\partial \hat{s}}{\partial x_k} \right) dV = 0 \tag{4.18}$$

The stabilization factor τ_e is chosen to be

$$\tau_e = \beta \frac{h_e}{2|\mathbf{v}|} \tag{4.19}$$

where β is a non-dimensional, non-negative stability parameter, h_e is the characteristic element length and $|\mathbf{v}|$ is the norm of velocity.

4.4 Numerical Implementations

The nonlinear Equations (4.15)-(4.18) can be linearized and solved by Newton-Raphson method. A progressively stiffening solution procedure presented in [34] is used to improve the convergence.

4.4.1 Finite Element Formulation

The discretized finite element formulation for Equations (4.15)-(4.18) is obtained in a two dimensional 4-node quadrilateral element. To solve the four unknown fields (velocity $\mathbf{V}$, total deformation gradient $\mathbf{F}$, viscoplastic part of the deformation gradient $\mathbf{F}^{vp}$ and internal variable $\mathbf{s}$) simultaneously, each quadrilateral 4-node element has 48 degrees of freedom, which are shown in Figure 4.1.

Degrees of freedom at each node: Total

$1. V_x, V_y, F_{xx}, F_{xy}, F_{yx}, F_{yy}, F_{xx}^{vp}, F_{xy}^{vp}, F_{yx}^{vp}, F_{yy}^{vp}, F_{zz}^{vp}, S$ 12

$2. V_x, V_y, F_{xx}, F_{xy}, F_{yx}, F_{yy}, F_{xx}^{vp}, F_{xy}^{vp}, F_{yx}^{vp}, F_{yy}^{vp}, F_{zz}^{vp}, S$ 12

$3. V_x, V_y, F_{xx}, F_{xy}, F_{yx}, F_{yy}, F_{xx}^{vp}, F_{xy}^{vp}, F_{yx}^{vp}, F_{yy}^{vp}, F_{zz}^{vp}, S$ 12

$4. V_x, V_y, F_{xx}, F_{xy}, F_{yx}, F_{yy}, F_{xx}^{vp}, F_{xy}^{vp}, F_{yx}^{vp}, F_{yy}^{vp}, F_{zz}^{vp}, S$ 12

48
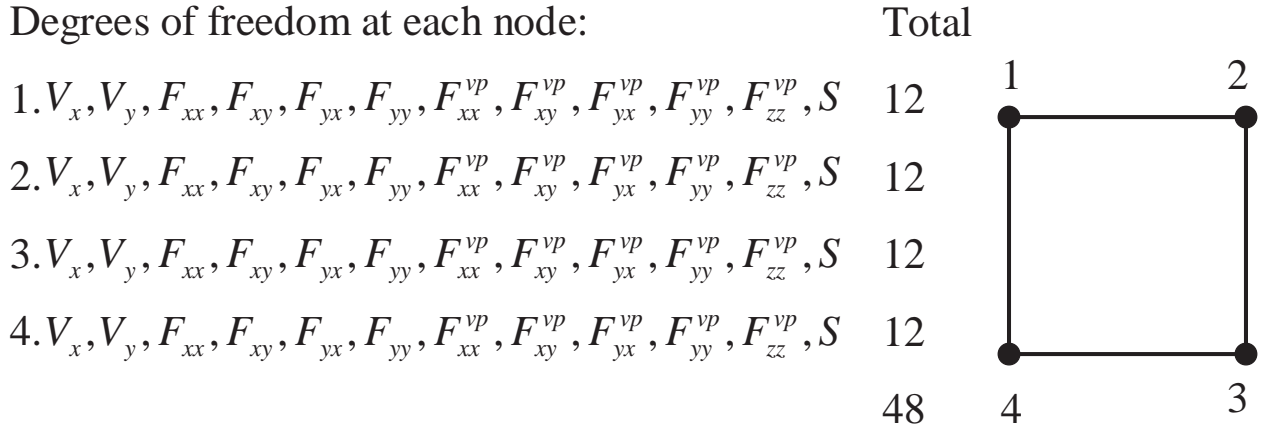
Fig. 4.1. Mixed four-node quadrilateral element for the true equilibrium formulation

4.4.1.1 Matrix Vector Transformation

To derive the expressions for the element residual and the element tangent matrix, variables in tensor formate, such as stress σ_{ij}, elastic strain E_{ij}^{e} and deformation gradient F_{ij}, need to be transformed to vector formate. In this article, two types of tensor-vector

transformation are defined to change symmetric and unsymmetrical tensors to vectors. The bar ($\bar{}$) transformation, which can change symmetric tensors to engineering format vectors, leads to:

$$\bar{\boldsymbol{\sigma}} = \begin{bmatrix} \sigma_{xx} \\ \sigma_{yy} \\ \sigma_{zz} \\ \sigma_{xy} \end{bmatrix} \quad ; \quad \bar{\boldsymbol{\sigma}}' = \begin{bmatrix} \sigma'_{xx} \\ \sigma'_{yy} \\ \sigma'_{zz} \\ \sigma'_{xy} \end{bmatrix} \quad ; \quad \bar{\mathbf{E}}^e = \begin{bmatrix} E^e_{xx} \\ E^e_{yy} \\ E^e_{zz} \\ E^e_{xy} \end{bmatrix} \tag{4.20}$$

The tilde ($\tilde{}$) transformation, which can transform unsymmetrical tensors to their vector form, can be expressed as:

$$\tilde{\mathbf{F}} = \begin{bmatrix} F_{xx} \\ F_{yx} \\ F_{xy} \\ F_{yy} \end{bmatrix} \quad ; \quad \tilde{\mathbf{F}}^e = \begin{bmatrix} F^e_{xx} \\ F^e_{yx} \\ F^e_{xy} \\ F^e_{yy} \\ F^e_{zz} \end{bmatrix} \quad ; \quad \tilde{\mathbf{F}}^{vp} = \begin{bmatrix} F^{vp}_{xx} \\ F^{vp}_{yx} \\ F^{vp}_{xy} \\ F^{vp}_{yy} \\ F^{vp}_{zz} \end{bmatrix} \quad ; \quad \tilde{\mathbf{L}} = \begin{bmatrix} L_{xx} \\ L_{yx} \\ L_{xy} \\ L_{yy} \end{bmatrix} \tag{4.21}$$

The fourth order isotropic elasticity tensor C_{ijkl} can be written in a matrix form as:

$$\bar{\mathbf{C}} = \frac{E}{(1+\nu)(1-2\nu)} \begin{bmatrix} (1-\nu) & \nu & \nu & 0 \\ \nu & (1-\nu) & \nu & 0 \\ \nu & \nu & (1-\nu) & 0 \\ 0 & 0 & 0 & .5-\nu \end{bmatrix} \quad (4.22)$$

To compute the evolution of the total and viscoplastic part of the deformation gradient tensor, the veolcity gradient tensor L_{ij} and viscoplastic strain tensor D^{vp}_{ij} can be organized as the following matrix forms:

$$\mathbf{L}^M = \begin{bmatrix} L_{11} & L_{12} & 0 & 0 \\ L_{21} & L_{22} & 0 & 0 \\ 0 & 0 & L_{11} & L_{12} \\ 0 & 0 & L_{21} & L_{22} \end{bmatrix} \quad (4.23)$$

and,

$$\mathbf{D}^M = \begin{bmatrix} D^{vp}_{11} & D^{vp}_{12} & 0 & 0 & 0 \\ D^{vp}_{21} & D^{vp}_{22} & 0 & 0 & 0 \\ 0 & 0 & D^{vp}_{11} & D^{vp}_{12} & 0 \\ 0 & 0 & D^{vp}_{21} & D^{vp}_{22} & 0 \\ 0 & 0 & 0 & 0 & D^{vp}_{33} \end{bmatrix} \tag{4.24}$$

4.4.1.2 Finite Element Residual Equations

The weak formulation Equations (4.15)-(4.18) are implemented in a four-node quadrilateral element to obtain the expressions for the element residual vector and the element Jacobian matrix. The same first order shape functions are used to interpolate the coordinate, velocity, deformation gradient, viscoplastic part of the deformation gradient and internal variable of a point within the element from these values of nodes. Matrices $\mathbf{N}^{v,\ F,\ F^{vp},\ s}$ and $\mathbf{B}^{v,\ F,\ F^{vp},\ s,\ L}$ are shape functions and gradient interpolators which are developed in Appendix D. w is the Gaussian weighting function. J and j are the volume and area determinant of the Jacobian matrices respectively. The assembly of the element residual vector $\mathbf{R}$ and nodal field vector $\mathbf{U}$ is obtained as follows:

$$\mathbf{R} = \begin{Bmatrix} \mathbf{R}^v \\ \mathbf{R}^F \\ \mathbf{R}^{F^{vp}} \\ \mathbf{R}^s \end{Bmatrix} ; \quad \mathbf{U} = \begin{Bmatrix} \mathbf{U}^v \\ \mathbf{U}^F \\ \mathbf{U}^{F^{vp}} \\ \mathbf{U}^s \end{Bmatrix} \qquad (4.25)$$

The expressions for the components of the element residual are:

$$R_i^v = \sum_{VGaussPoint} \left[B_{ji} \, \bar{\sigma}_j \right] \omega J - \sum_{AtGaussPoint} \left[N_{ji} \, t_j^p \right] \omega j \qquad (4.26)$$

$$R_i^F = \sum_{VGaussPoint} \left[N_{mi}^F + \tau_e \, v_n \, B_{min}^F \right] \left[B_{mjk}^F \, v_k \, U_j^F - L_{ml}^M \, N_{lj}^F \, U_j^F \right] \omega J \qquad (4.27)$$

$$R_i^{F^{vp}} = \sum_{VGaussPoint} \left[N_{mi}^{F^{vp}} + \tau_e \, v_k \, B_{mik}^{F^{vp}} \right] \cdot$$

$$\left[B_{mjk}^{F^{vp}} \, v_k \, U_j^{F^{vp}} - D_{ml}^M \, N_{lj}^{F^{vp}} \, U_j^{F^{vp}} \right] \omega J \qquad (4.28)$$

$$R_i^s = \sum_{VGaussPoint} \left[N_i^s + \tau_e \, v_k \, B_{ki}^s \right] \left[B_{kj}^s \, v_k \, U_j^s - g(\tilde{\sigma}, s) \right] \omega J \qquad (4.29)$$

4.4.1.3   Element Stiffness matrix

Linearization of Equations (4.26)-(4.29) leads to the following element tangent

matrix:

$$\frac{\partial \mathbf{R}}{\partial \mathbf{U}} = \begin{bmatrix} \frac{\partial \mathbf{R}^v}{\partial \mathbf{U}^v} & \frac{\partial \mathbf{R}^v}{\partial \mathbf{U}^F} & \frac{\partial \mathbf{R}^v}{\partial \mathbf{U}^{F^{vp}}} & \frac{\partial \mathbf{R}^v}{\partial \mathbf{U}^s} \\\\ \frac{\partial \mathbf{R}^F}{\partial \mathbf{U}^v} & \frac{\partial \mathbf{R}^F}{\partial \mathbf{U}^F} & \frac{\partial \mathbf{R}^F}{\partial \mathbf{U}^{F^{vp}}} & \frac{\partial \mathbf{R}^F}{\partial \mathbf{U}^s} \\\\ \frac{\partial \mathbf{R}^{F^{vp}}}{\partial \mathbf{U}^v} & \frac{\partial \mathbf{R}^{F^{vp}}}{\partial \mathbf{U}^F} & \frac{\partial \mathbf{R}^{F^{vp}}}{\partial \mathbf{U}^{F^{vp}}} & \frac{\partial \mathbf{R}^{F^{vp}}}{\partial \mathbf{U}^s} \\\\ \frac{\partial \mathbf{R}^s}{\partial \mathbf{U}^v} & \frac{\partial \mathbf{R}^s}{\partial \mathbf{U}^F} & \frac{\partial \mathbf{R}^s}{\partial \mathbf{U}^{F^{vp}}} & \frac{\partial \mathbf{R}^s}{\partial \mathbf{U}^s} \end{bmatrix} \tag{4.30}$$

Where,

$$\frac{\partial R^v_i}{\partial U^v_j} = \sum_{VGaussPoint} B_{ik}\,\mu B_{kj}\,\omega J \tag{4.31}$$

$$\frac{\partial R^v_i}{\partial U^F_j} = \sum_{VGaussPoint} B_{ik}\,\bar{C}_{kl}\,\frac{\partial \bar{E}^e_l}{\partial U^F_j}\omega J \tag{4.32}$$

$$\frac{\partial R^v_i}{\partial U^{F^{vp}}_j} = \sum_{VGaussPoint} B_{ik}\,\bar{C}_{kl}\,\frac{\partial \bar{E}^e_l}{\partial U^{F^{vp}}_j}\omega J \tag{4.33}$$

$$\frac{\partial R^v_i}{\partial U^s_j} = 0 \tag{4.34}$$

$$
\frac{\partial R^F_i}{\partial U^v_p} = \sum_{VGaussPoint} \left[N^F_{mi} B^F_{mjk} N^v_{kp} U^F_j + \right.
$$

$$
\left. \tau_e N^v_{np} B^F_{min} \left(2 B^F_{mjk} v_k U^F_j - L^M_{ml} N^F_{lj} U^F_j \right) \right] \omega J
$$

$$
- \left[(N^F_{mi} + \tau_e v_n B^F_{min}) \cdot B^L_{mlp} N^F_{lj} U^F_j \right] \omega J \tag{4.35}
$$

$$
\frac{\partial R^F_i}{\partial U^F_j} = \sum_{VGaussPoint} \left[N^F_{mi} + \tau_e v_n B^F_{min} \right] \left[B^F_{mjk} v_k - L^M_{ml} N^F_{lj} \right] \omega J \tag{4.36}
$$

$$
\frac{\partial R^F_i}{\partial U^{F^{vp}}_j} = 0 \tag{4.37}
$$

$$
\frac{\partial R^F_i}{\partial U^s_j} = 0 \tag{4.38}
$$

$$
\frac{\partial R^{F^{vp}}_i}{\partial U^v_p} = \sum_{VGaussPoint} \left[N^{F^{vp}}_{mi} B^{F^{vp}}_{mjk} N^v_{kp} U^{F^{vp}}_j + \right.
$$

$$
\left. \tau_e N^v_{np} B^{F^{vp}}_{min} \left(2 B^{F^{vp}}_{mjk} v_k U^{F^{vp}}_j - L^M_{ml} N^{F^{vp}}_{lj} U^{F^{vp}}_j \right) \right] \omega J
$$

$$
- \left[(N^{F^{vp}}_{mi} + \tau_e v_n B^{F^{vp}}_{min}) \cdot \frac{\partial D^M_{ml}}{\partial U^v_p} N^{F^{vp}}_{lj} U^{F^{vp}}_j \right] \omega J \tag{4.39}
$$

$$\frac{\partial R^{F^{vp}}_{i}}{\partial U^{F}_{j}} = \sum_{VGaussPoint} -\left(N^{F^{vp}}_{mi} + \tau_e v_n B^{F^{vp}}_{min}\right) \cdot \frac{\partial D^{M}_{ml}}{\partial U^{F}_{j}} N^{F^{vp}}_{lk} U^{F^{vp}}_{k} \omega J \qquad (4.40)$$

$$\frac{\partial R^{F^{vp}}_{i}}{\partial U^{F^{vp}}_{j}} = \sum_{VGaussPoint} \left[N^{F^{vp}}_{mi} + \tau_e v_n B^{F^{vp}}_{min}\right]$$

$$\left[B^{F^{vp}}_{mjk} v_k - D^{M}_{ml} N^{F^{vp}}_{lj} - \frac{\partial D^{M}_{ml}}{\partial U^{F^{vp}}_{j}} N^{F^{vp}}_{lp} U^{Fvp}_{p}\right] \omega J \qquad (4.41)$$

$$\frac{\partial R^{F^{vp}}_{i}}{\partial U^{s}_{j}} = \sum_{VGaussPoint} -\left(N^{F^{vp}}_{mi} + \tau_e v_n B^{F^{vp}}_{min}\right) \cdot \frac{\partial D^{M}_{ml}}{\partial U^{s}_{j}} N^{F^{vp}}_{lk} U^{F^{vp}}_{k} \omega J \qquad (4.42)$$

$$\frac{\partial R^{s}_{i}}{\partial U^{v}_{p}} = \sum_{VGaussPoint} \left[N^{s}_{i} B^{s}_{kj} N^{v}_{kp} U^{s}_{j}\right] \omega J$$

$$+\tau_e B^{s}_{ki} N^{v}_{kp} \left[2B^{s}_{kj} v_k U^{s}_{j} - g(\tilde{\sigma}, s)\right] \omega J \qquad (4.43)$$

$$\frac{\partial R^{s}_{i}}{\partial U^{F}_{j}} = \sum_{VGaussPoint} \left[N^{s}_{i} + \tau_e v_k B^{s}_{ki}\right] \left[-\frac{\partial g(\tilde{\sigma}, s)}{\partial U^{F}_{j}}\right] \omega J \qquad (4.44)$$

$$\frac{\partial R^{s}_{i}}{\partial U^{F^{vp}}_{j}} = \sum_{VGaussPoint} \left[N^{s}_{i} + \tau_e v_k B^{s}_{ki}\right] \left[-\frac{\partial g(\tilde{\sigma}, s)}{\partial U^{F^{vp}}_{j}}\right] \omega J \qquad (4.45)$$

$$\frac{\partial R^s_i}{\partial U^s_j} = \sum_{VGaussPoint} \left[N^s_i + \tau \, v_e \, B^s_{k \, ki} \right] \left[B^s_{kj} \, v_k - \frac{\partial g(\tilde{\sigma}, s)}{\partial U^s_j} \right] \omega J \tag{4.46}$$

The detail expressions of $\dfrac{\partial \bar{E}^e_i}{\partial U_j}$ in the above equations are shown in Appendix E.

4.4.2 Constitutive Law and Progressively Stiffening Algorithm

The constitutive law implemented in this paper is a rate dependent elasto-visco-plastic model originally presented in Reference [37]. The function $f(\tilde{\sigma}, s)$ in Equation (4.10) is taken to be:

$$\dot{\tilde{\varepsilon}}^{vp} = f(\tilde{\sigma}, s) = A \left(sinh \left(\xi \frac{\tilde{\sigma}}{s} \right) \right)^{\frac{1}{m}} \tag{4.47}$$

where $A = A_0 \cdot exp(-Q/RT)$, Q is the thermal activation energy, R is the ideal gas constant, and T is the absolute temperature. A_0, ξ and m are the material parameters listed in Table 4.1.

The internal variable evolution Equation (4.14), defined by the function g, is chosen to be:

$$g(\tilde{\sigma}, s) = h_0 \left| \left(1 - \frac{s}{s^*} \right) \right|^a sign \left(1 - \frac{s}{s^*} \right) \cdot A \left(sinh \left(\xi \frac{\tilde{\sigma}}{s} \right) \right)^{\frac{1}{m}} \tag{4.48}$$

with,

$$s^* = \tilde{s} \left(\frac{\dot{\tilde{\varepsilon}}^{vp}}{A} \right)^n \tag{4.49}$$

where h_0, a, s and n are the material parameters listed in Table 4.1.

Material Parameter	Value	Material Parameter	Value
A_0	$6.34*10^{11} sec^{-1}$	Q	312.35 KJ/mole
ξ	3.25	R	8.314
m	0.1956	a	1.5
n	0.06869	$\tilde{s}$	125.1 MPa
s_0	80 MPa	h_0	3093.1 MPa

Table 4.1. Material Parameters for HSLA-65 steel

HSLA-65 steel with strain rate between $1*10^{-3}$ and $1*10^{-4}$ is considered in this work. The material properties for Anand's model of the HSLA-65 steel are listed in Table 4.1. These material parameters are determined based on the experimental stress-strain plot of the HSLA-65 steel shown in Reference [55]. Using the radial-return algorithm presented in Reference [56], the computed stress-strain relationships of the HSLA-65 under different temperatures are shown in Figure 4.2.

Because the constitutive laws, specifically the *sinh* function in Equations (4.47) and (4.48), are highly non-linear, obtaining a robust convergence solution is diffuclt. A progressively stiffened algorithm introduced in [34], which is able to obtain a robust convergence, is used in this work. The constitutive relationship begins with a smooth exponential function (f_{begin}) and is made progressively more non-linear in a stepwise manner, until it completely switches to the objective *sinh* function. An automatic stiffening stepping procedure, similar to the automatic time-stepping procedure, is used in
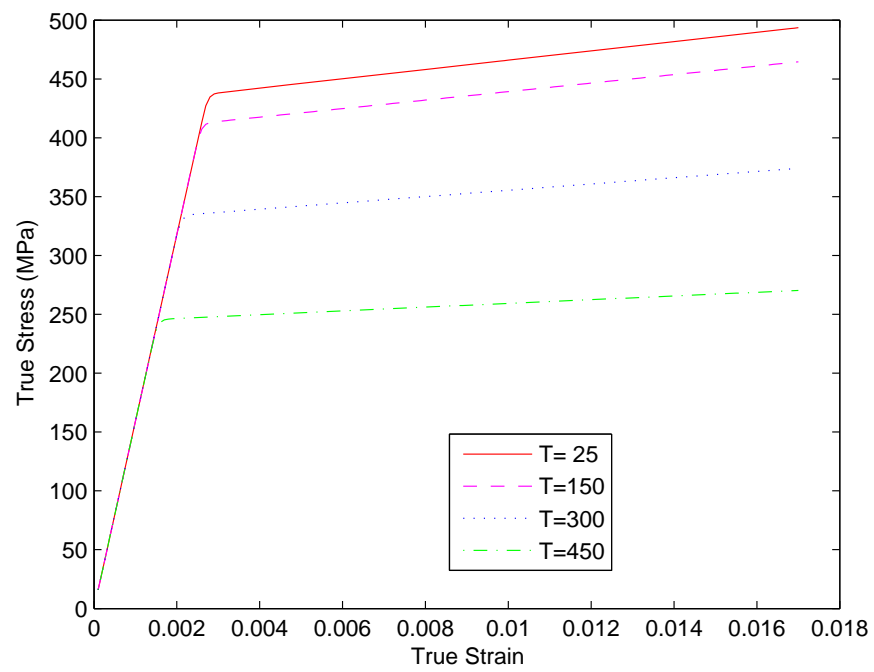
Fig. 4.2.   Stress-Strain Curves of HSLA-65 Steel Under Different Temperature

order to control and optimize the step size. The modified constitutive equation at a stiffening step k is:

$$f_p(k) = f_{begin} * (1 - k) + f \cdot k^3, \quad 0 \leq k \leq 1 \tag{4.50}$$

where, k is a control variable ranging from 0 to 1, $f_p(k)$ is a progressively stiffening function of the visco-plastic strain rate $\dot{\tilde{\varepsilon}}^{vp}$, f_{begin} is the starting function of $\dot{\tilde{\varepsilon}}^{vp}$ defined by:

$$f_{begin} = \left(exp\left(\frac{\tilde{\sigma}}{s}\right) - 1 \right) * \alpha_{begin} \tag{4.51}$$

where the parameter α_{begin} can be determined by:

$$\alpha_{begin} = exp\left(\frac{1}{\xi} \cdot asinh\left(\left(\frac{\beta}{A}\right)^m \right) - 1 \right) \cdot \frac{1}{\beta} \tag{4.52}$$

4.5 Numerical Examples

The above Eulerian formulation is implemented in a 2 dimensional four-node quadrilateral element by an OMP FORTRAN 90 computer code. Three numerical examples are performed to verify the validity of the true equilibrium formulation and to demonstrate the difference between the rate equilibrium and true equilibrium formulation. In a disturbed flow model and a strip drawing model, velocity boundary conditions are applied in the down stream of the inlet surface to test the accuracy and validity of the true equilibrium formulation and the rate equilibrium formulation. The Gas Metal Arc

Welding model with velocity and non-deformed condition only applied on the inlet sur-
face is also simulated to investigate the difference between the true and rate formulation
methods.

4.5.1   Disturbed flow
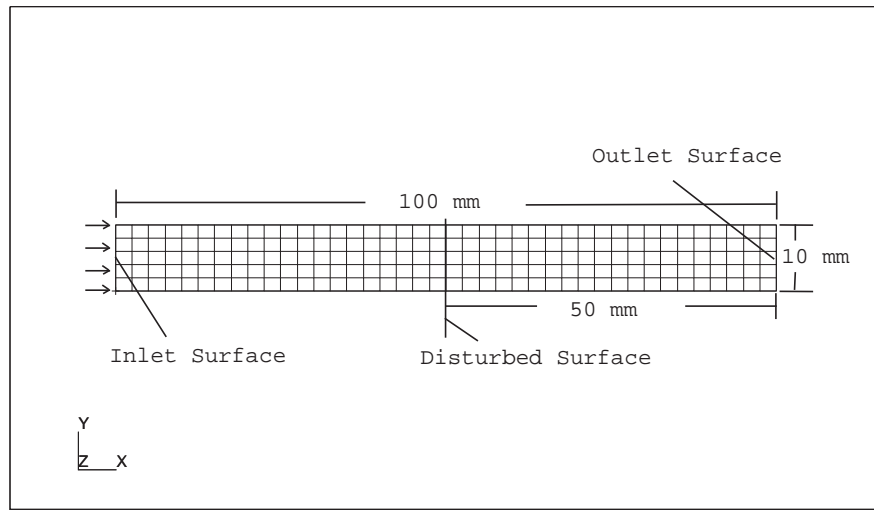
Fig. 4.3.   Disturbed Flow model

Figure 4.3 shows the model of a disturbed flow. A material is flowing in to a
$100 \ mm \ \times \ 10 \ mm$ domain at a speed of $1 \ mm/s$ from the inlet surface. The domain is
discretized into 200 four-node quadrilateral elements. Anand's model is used to represent
the elastic response of the material flow under room temperature. To simulate pure
elastic response, Young's modulus is set to be $E = 1000MPa$, and only the velocity
equation and the deformation gradient equation are activated. The material is disturbed

and the velocity is increased to 1.001 mm/s, while it flows through the disturbed surface.

The boundary conditions are:

- Inlet Surface

$$v_x = v_{in} = 1mm/s \tag{4.53}$$

$$v_y = 0 \tag{4.54}$$

$$F_{ij} = \delta_{ij} \tag{4.55}$$

$$F_{ij}^{vp} = \delta_{ij} \tag{4.56}$$

$$s = s_0 = 80MPa \tag{4.57}$$

$$\tag{4.58}$$

- Disturbed Surface

$$v_x = 1.001 \; mm/s \tag{4.59}$$

$$v_y = 0 \; mm/s \tag{4.60}$$

Both the rate equilibrium and the true equilibrium formulation are performed to simulate the disturbed flow model. The velocity results for the rate and true equilibrium methods are plotted in Figures 4.4 and 4.5, respectively. The norm of the velocity along the center of the plate of these two analysis is plotted in Figure 4.6. The velocity results for the rate equilibrium method remain unchanged at 1.001 mm/s after the material goes through the disturbed surface, while the velocity results at the outlet surface for
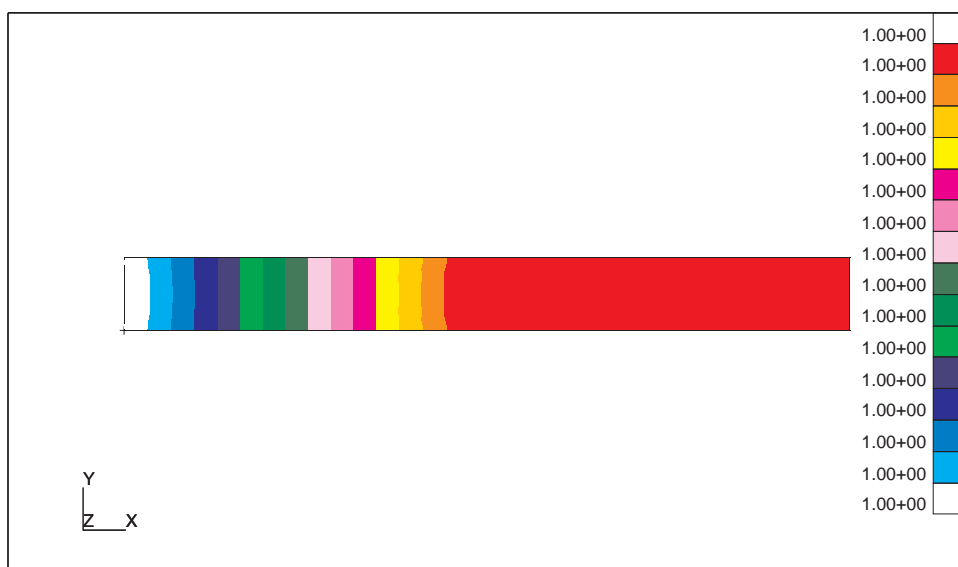
Fig. 4.4.   Velocity for the rate equilibrium equations
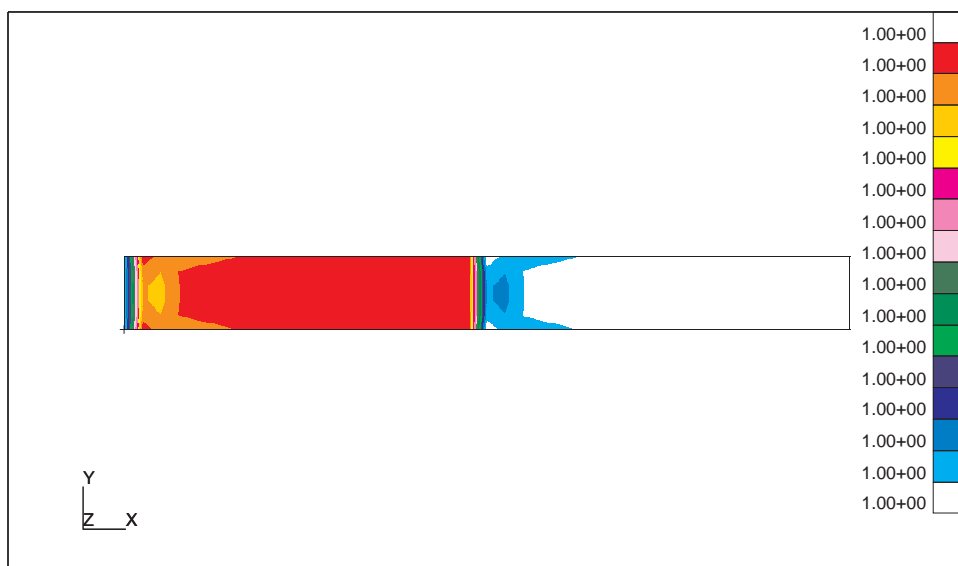
Fig. 4.5.   Velocity for the true equilibrium equations
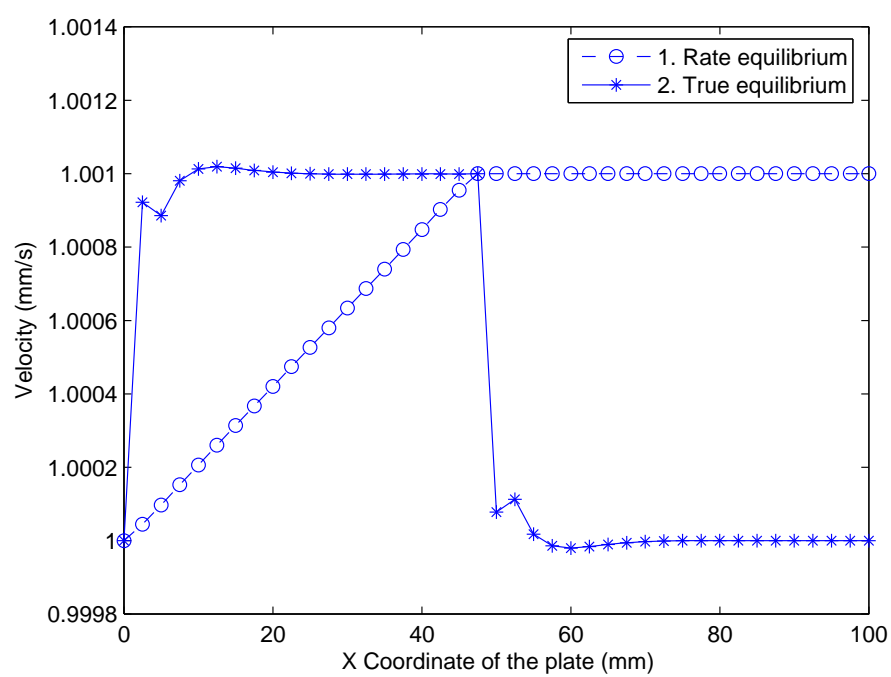
Fig. 4.6.   Compared velocity results

the true equilibrium analysis become the inlet velocity (1 mm/s). The von Mises stress results of these two methods are also plotted in Figures 4.7 and 4.8, respectively. It can also be observed form these plots that, the von Mises stress results of the rate equilibrium formulation do not change in the down stream of the disturbed surface, while the von Mises stress results of the true equilibrium method become zero at the outlet surface. These are because the constant velocity and nonzero stress results satisfy the rate equilibrium condition, while they don't satisfy the true equilibrium condition. This model indicates that the true equilibrium approach is more accurate than the rate equilibrium. To use the results from rate equilibrium approach, the equilibrium condition needs to be check, because adding any constant number to the true equilibrium condition can still satisfy the rate equilibrium equation.
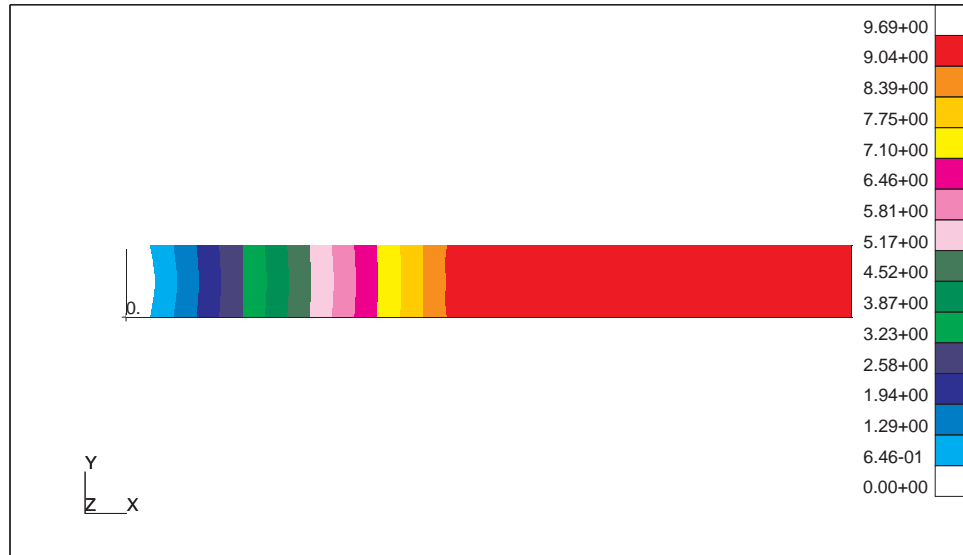
Fig. 4.7.   von Mises stress for the rate equilibrium equations
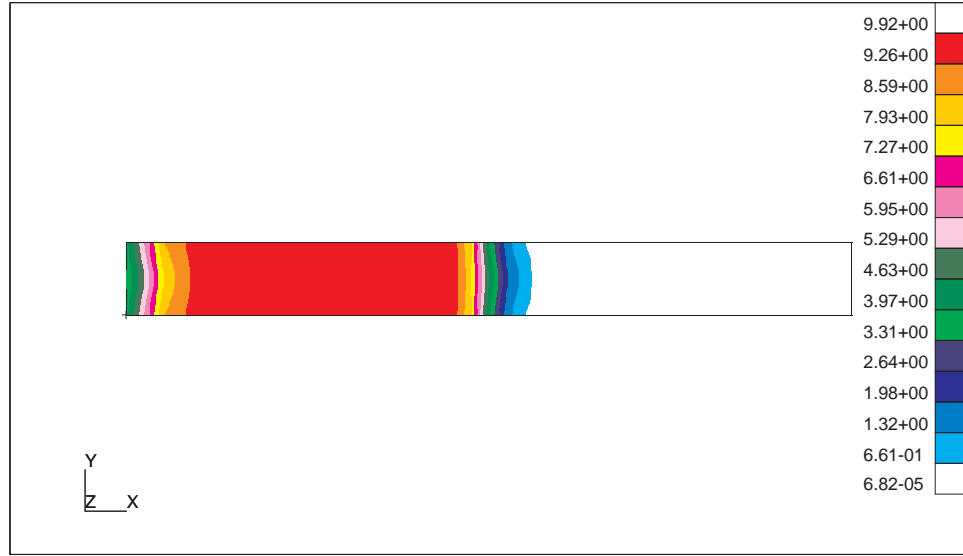
Fig. 4.8.   von Mises stress for the true equilibrium equations

4.5.2   Strip Drawing

A strip drawing through a frictionless die is used to test the true equilibrium formulation and further demonstrate the difference between the rate equilibrium and the true equilibrium methods. Figure 4.9 shows the geometry of the strip drawing example for Eulerian analysis. The model is discretized into 640 mixed four-node quadrilateral elements. Surface A is the inlet surface where the material enters the control volume and surface B is the outlet surface where the material leaves the control volume. Due to symmetry, only a half of the model is considered, the surface C is the symmetric boundary. A fourth order polynomial function is used to describe the die curvature such that the slope is zero at both ends and midpoint of the extrusion surface E. The

material is reduced 10% as it goes thought the die. The temperature is assumed to be 20 $^{\circ}$C everywhere and the Poisson's ratio of this example is 0.3.

Mechanical analysis whit both the true equilibrium and rate equilibrium formulation is simulated in an Eulerian frame. The following boundary conditions are applied to the model for both true and rate analysis:

- Inlet surface A

$$v_x = v_{in} = .1mm/s \tag{4.61}$$

$$v_y = 0 \tag{4.62}$$

$$F_{ij} = \delta_{ij} \tag{4.63}$$

$$F_{ij}^{vp} = \delta_{ij} \quad (For\ true\ equilibrium\ analysis) \tag{4.64}$$

$$\sigma_{ij} = 0 \quad (For\ rate\ equilibrium\ analysis) \tag{4.65}$$

$$s = s_0 = 80MPa \tag{4.66}$$

- Symmetric surface C

$$v_y = 0 \tag{4.67}$$

- Extrusion surface E

$$v_x = v_{in} = .1mm/s \tag{4.68}$$

$$v_y = f' v_x \tag{4.69}$$
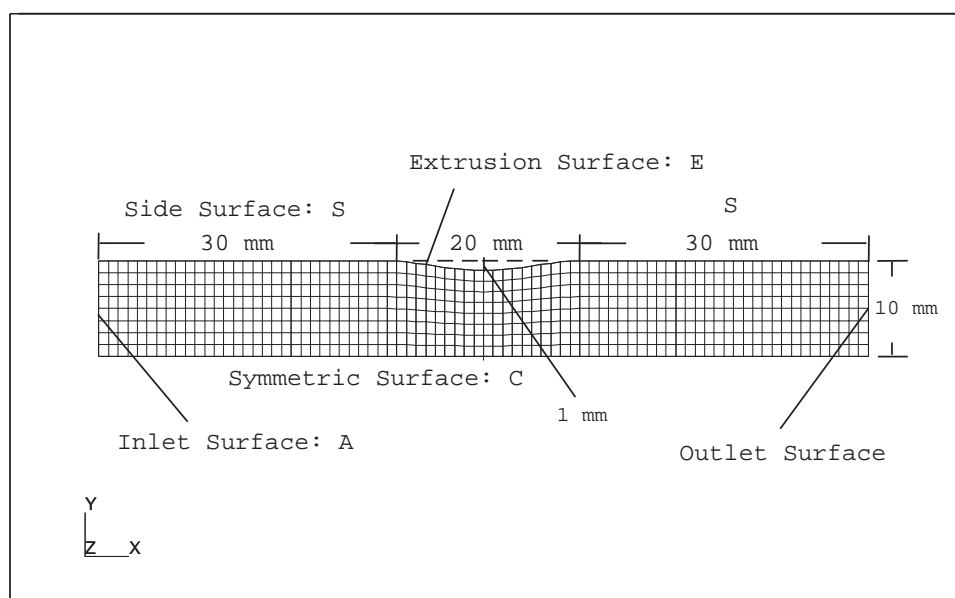
Fig. 4.9.   Strip drawing model - Eulerian

$$(4.70)$$

- Side surface S

$$v_x = v_{in} = .1mm/s \tag{4.71}$$

$$v_y = 0 \tag{4.72}$$

where, f' is the slope of the extrusion surface E.

4.5.2.1 Elastic Case

Pure elastic material response of the strip drawing model is first simulated. Anand's constitutive model with Young's modulus $E = 1000MPa$ is applied to the material. Because the mass and energy are conserved when the elastic material goes through the frictionless die, the velocity and stress states at the outlet boundary should be the same as the inlet boundary.

Figures 4.10 and 4.11 show the contour plots of the velocity results for the rate and true equilibrium methods, respectively. These results are similiar for both analysis methods. At the outlet surface, the velocity results recover to the same value as at the inlet boundary.

Figures 4.14 and 4.15 plot the von Mises contour results for the rate and true equilibrium formulations, respectively. To verify the results in an Eulerian frame, the strip drawing model is also performed by time incremental Lagrangian analysis, which has been shown to be able to effectively simulate elasto-plastic mechanical processes.
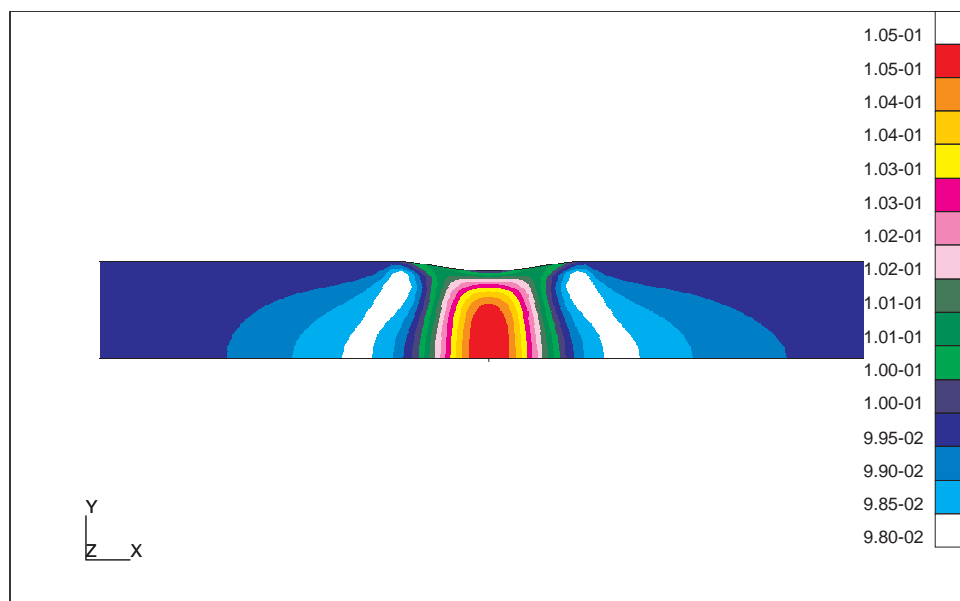
Fig. 4.10.   Velocity results for rate equilibrium equations
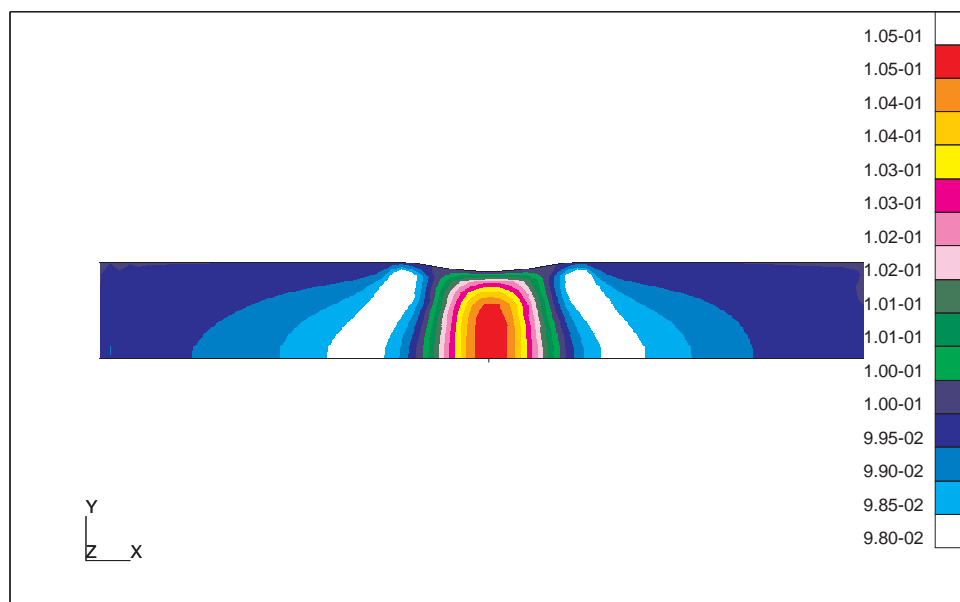
Fig. 4.11.   Velocity results for true equilibrium equations
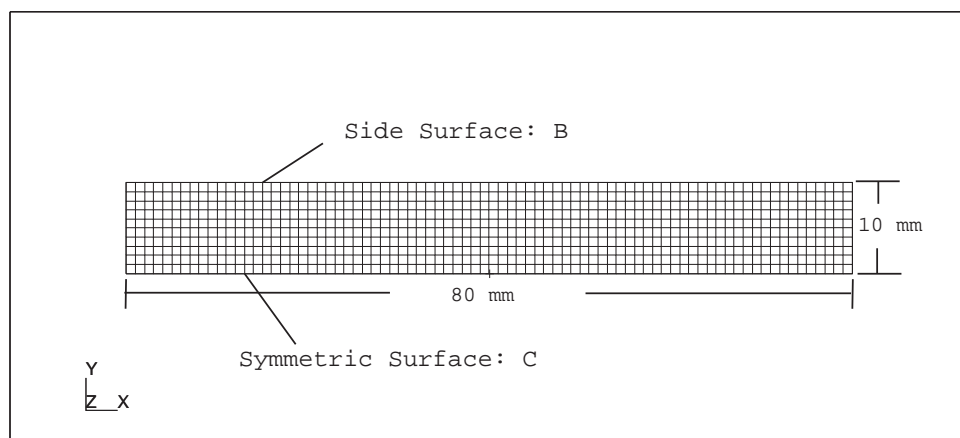
Fig. 4.12.   Strip drawing model - Lagrangian
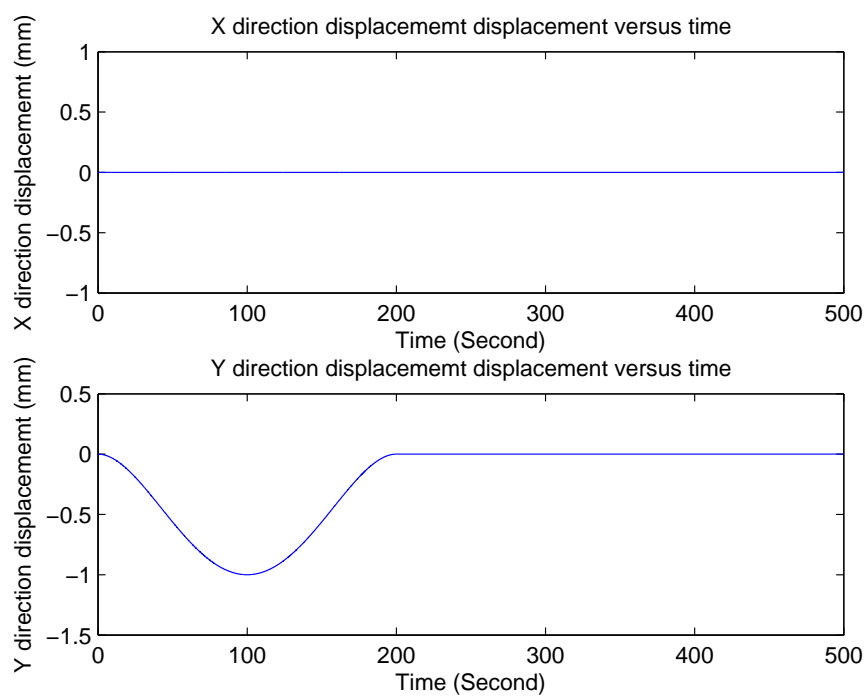
Fig. 4.13.   Boundary Conditions for Lagnrangian

The Lagrangian model is a block, which has the same length, thickness and material properties as in the Eulerian analysis, as shown in Figure 4.12. To simulate the same extrusion process as in Eulerian frames, the extrusion die is moved from the left to the right and the displacement of each node on the side surface **B** at a specific time step can be obtained by integrating the velocity boundary conditions of the Eulerian model. For example, the displacements of the node P at different time are plotted in Figure 4.13. The boundary conditions for the symmetric surface are:

$$u_y \quad = \quad 0 \qquad\qquad (4.73)$$

where, u_y is the Y direction displacement.

The von Mises stress results for the Lagrangian analysis are plotted in Figure 4.16. The true equilibrium Eulerian analysis obtains the similar results as the Lagrangian analysis. Both analysis predict zero stress on the outlet surface. However, the rate equilibrium Eulerian analysis can not get zero residual stress at the outlet surface, because only velocity boundary conditions are applied in this example. As shown in Reference [34], zero residual stress results can be obtained from the rate equilibrium analysis, if both velocity and traction rate boundary conditions are applied on the side and extrusion surface as:

$$v_y \quad = \quad f' v_x \qquad\qquad (4.74)$$

$$\dot{t}_n = \frac{u_t}{\rho} t_n \tag{4.75}$$

4.5.3   Gas Metal Arc Welding Example

In Chapter 3, the authors have simulated Gas metal arc welding (GMAW) by the rate equilibrium Eulerian analysis and Lagrangian analysis. In the work, the same GMAW procedure is simulated by the true equilibrium Eulerian analysis to demonstrate the accuracy of the true equilibrium method in simulating coupled thermo-mechanical analysis. Two 9 inch ($228.6mm$) wide 1/4 inch ($6.35mm$) thick HSLA-65 steel plates are welded together. The moving velocity of the torch is 2.54 mm/s along the weld centerline and the heat input of the torch is 28.6 $KJ/inch$. 2D plane strain models are used for both Lagrangian and Eulerian analyses. To eliminate the end effects, the Lagrangian model is ($L = 1300mm$) long, and the Eulerian model is even longer ($L = 3000mm$) to allow for sufficient cooling. Figures 4.17 and 4.18 show the Lagrangian and Eulerian models, respectively. The Lagrangian GMAW model is discretized into 1500 4-node quadrilateral elements with biased smaller element size at the welding region and the same element size alone the welding direction. The Eulerian GMAW model is discretized into 1776 4-node quadrilateral elements with refined mesh around the welding torch.

The heat flux distribution of the electric arc is modeled as a Gaussian distribution [62],

$$q = \frac{3\eta Q}{\pi R^2} \left[e^{-3\left(\left(\frac{x}{R}\right)^2 + \left(\frac{y}{R}\right)^2 \right)} \right] \tag{4.76}$$
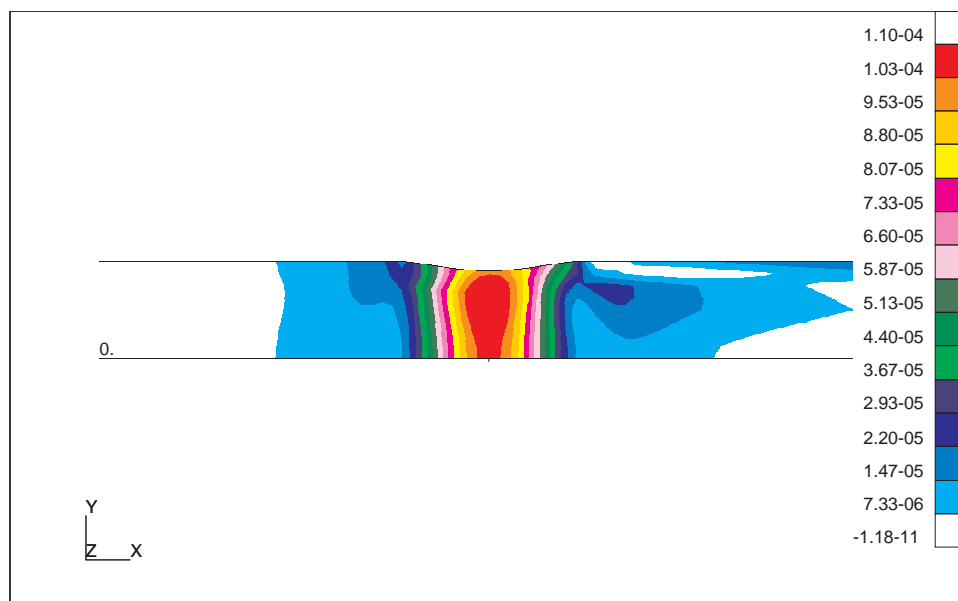
Fig. 4.14.   von Mises stress for Eulerian rate equilibrium analysis
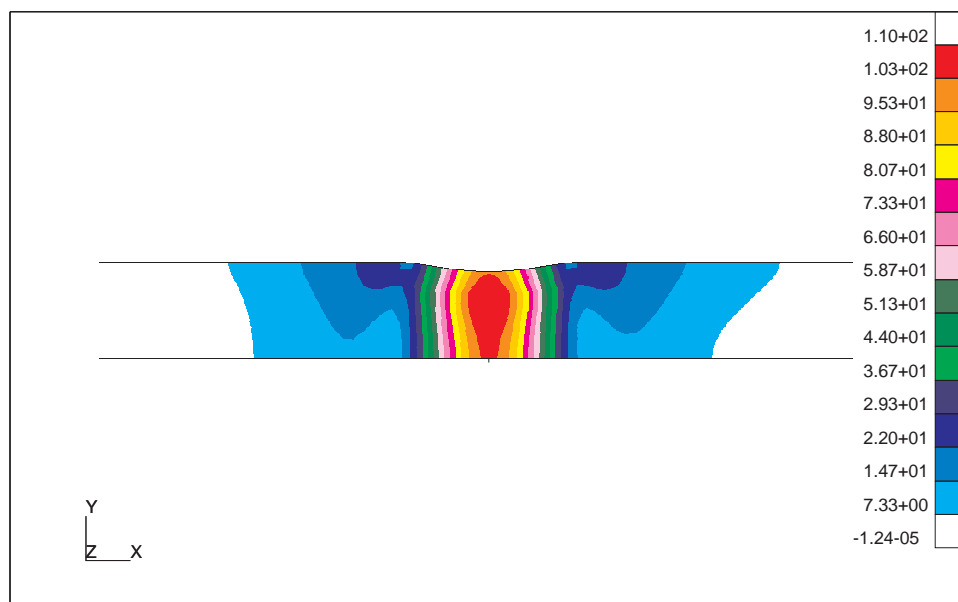
Fig. 4.15.   von Mises stress for Eulerian true equilibrium analysis
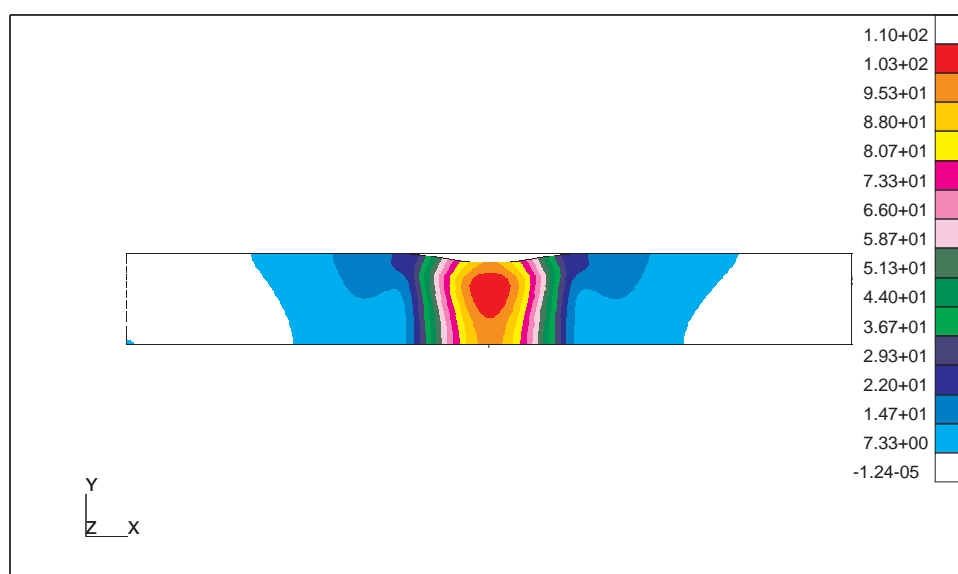
Fig. 4.16.   von Mises stress for Lagrangian analysis
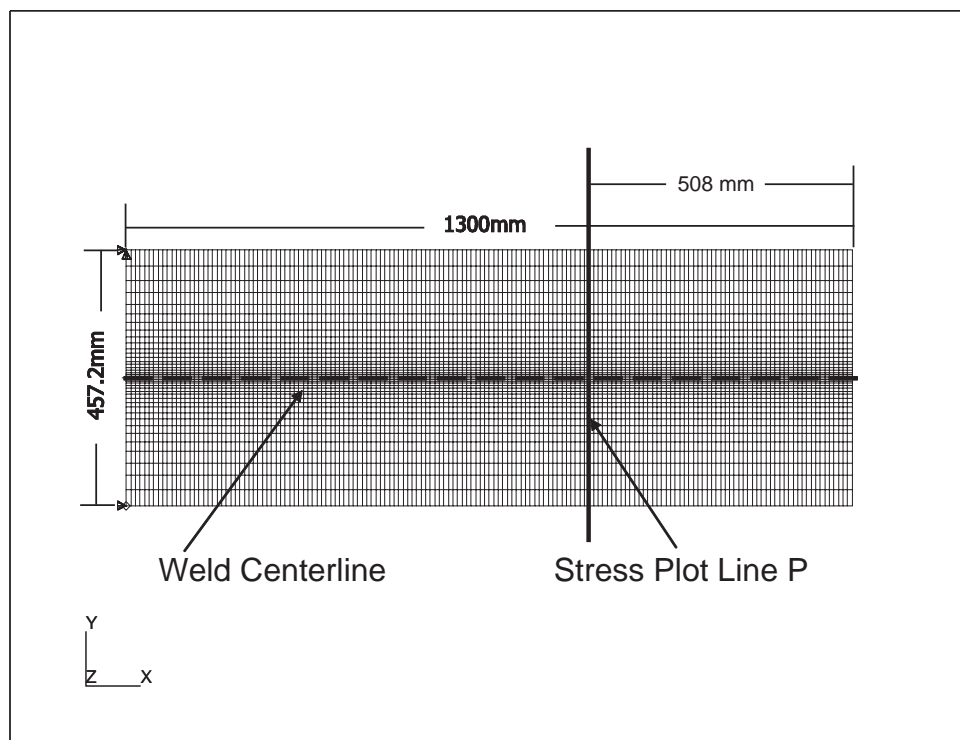
Fig. 4.17.   Lagrangian model
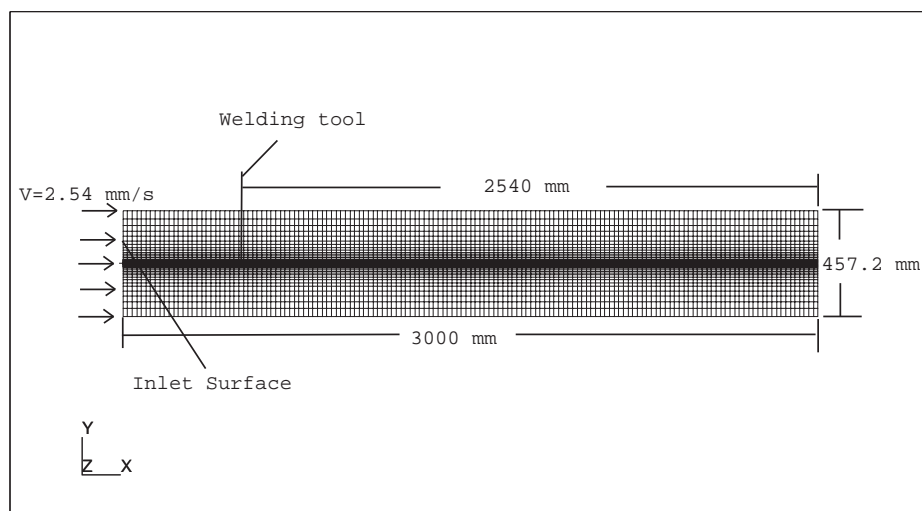
Fig. 4.18.   Eulerian model
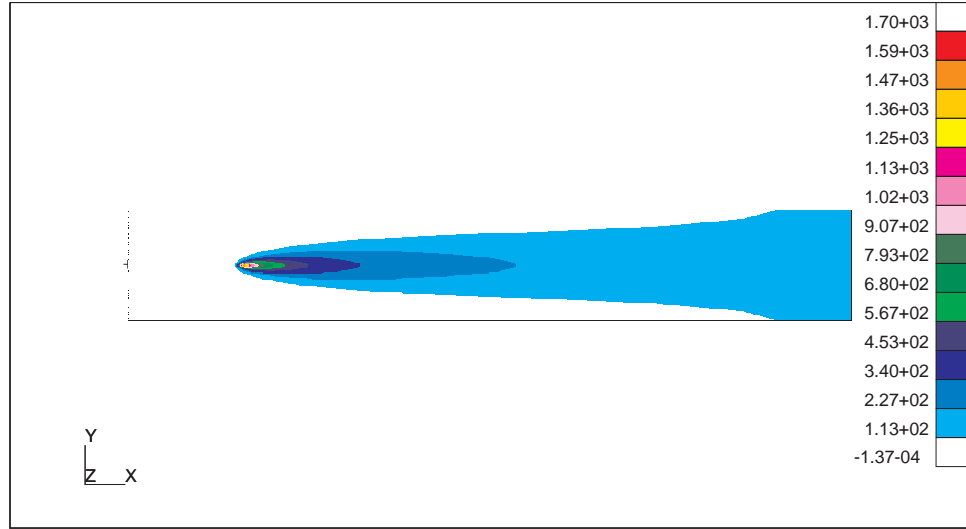
Fig. 4.19.   Eulerian thermal analysis results

where η is the torch efficiency, Q is the input power, R is the torch radius, and x and y are the distances of a point from the center of the laser beam. The radius R is $10mm$ and the torch efficiency η is taken as 0.8. For GMAW process, most investigors assume that the deformation has very small effect on the temperature distribution [23]. Therefore a heat transfer analysis is performed first, followed by a mechanical analysis using the temperature results as a thermal loading. The temperature results for the Eulerian thermal analysis is shown in Figure 4.19.

Following the thermal analysis, four cases of mechanical analyses are performed to simulate GMAW, as listed in Table 4.2. The traditional Lagrangian analysis using an elasto-plastic constitutive model, which has been shown to accurately predict residual stress, is performed in Case 1. In case 2, the Anand's elasto-viscoplastic model is implemented in a Lagrangian frame. Because the rate equilibrium Eulerian formulation is

	Reference Frame	Constitutive law	Elastic Properties
Case 1	Lagrangian	Elasto-plastic	Temperature dependent
Case 2	Lagrangian	Anand's model	Temperature dependent
Case 3	Eulerian (Rate)	Anand's model	Constant
Case 4	Eulerian (true)	Anand's model	Temperature dependent

Table 4.2. Analysis models for Gas Metal Arc Welding

not able to account for the change of material properties with temperature, the GMAW process is simulated by rate equilibrium Eulerian analysis in Anand's elasto-visco-plastic model with material properties in room temperature in case 3. In case 4, the true equilibrium Eulerian analysis is used to model GMAW with temperature dependent material properties, which are plotted in Figure 4.20.

The boundary conditions for the rate and true equilibrium Eulerian mechanical analysis are:

- True equilibrium Eulerian analysis

$$v_x = v_{in} = 2.54 mm/s \tag{4.77}$$

$$v_y = 0 \tag{4.78}$$

$$F_{ij} = \delta_{ij} \tag{4.79}$$

$$F^{vp}_{ij} = \delta_{ij} \tag{4.80}$$

$$s = s_0 = 80 MPa \tag{4.81}$$
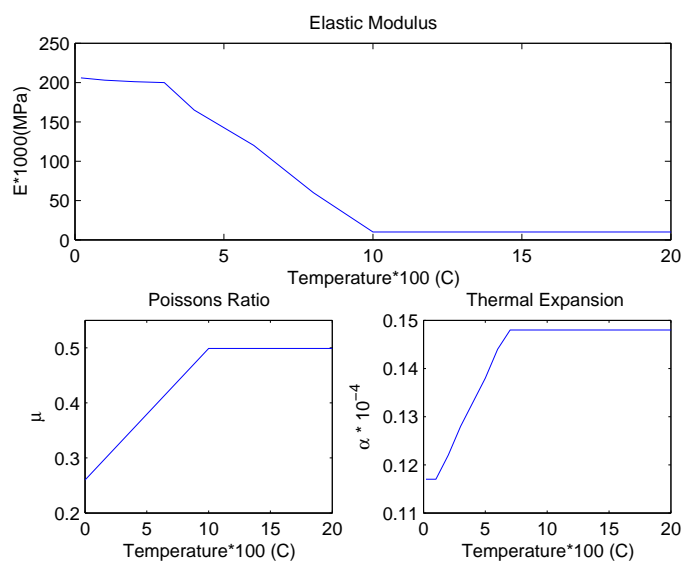
Fig. 4.20.   Material Properties
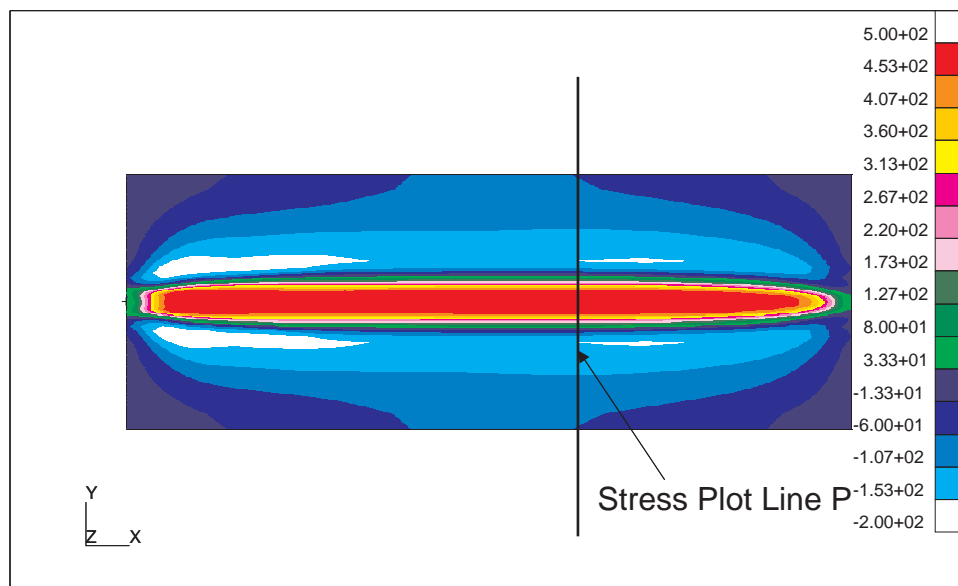
Fig. 4.21.   Longitudinal residual stress for Elasto-plastic model in Lagrangian frame (Case 1)
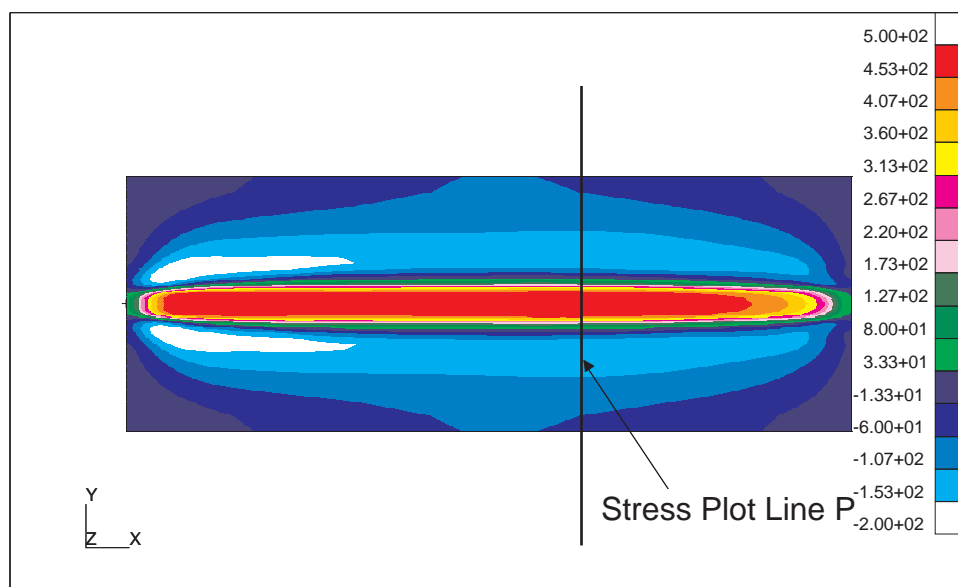
Fig. 4.22. Longitudinal residual stress for Anand model in Lagrangian frame (Case 2)
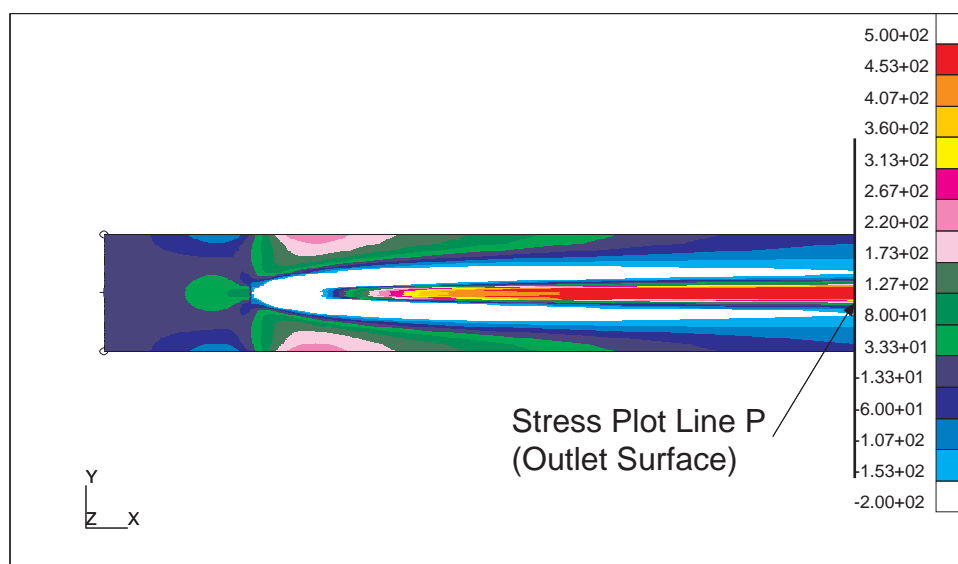
Fig. 4.23. Longitudinal residual stress for rate equilibrium in Eulerian frame (Case 3)
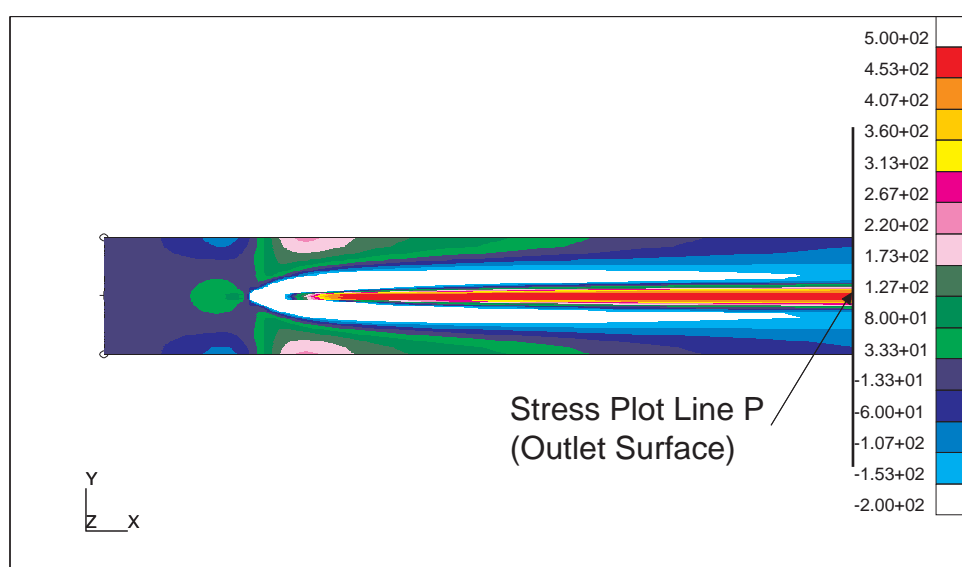
Fig. 4.24.   Longitudinal residual stress for true equilibrium in Eulerian frame (Case 4)

- Rate equilibrium Eulerian analysis

$$v_x = v_{in} = 2.54mm/s \tag{4.82}$$

$$v_y = 0 \tag{4.83}$$

$$\sigma_{ij} = 0 \tag{4.84}$$

$$F_{ij} = \delta_{ij} \tag{4.85}$$

$$s = s_0 = 80MPa \tag{4.86}$$

Figures 4.21 to 4.24 plot the contour results of the longitudinal residual stress for the four cases mechanical analysis. It can be observed from Figures 4.21 and 4.22 that the Anand's model can predict the same residual stress results as the elasto-plastic constitutive model and can be used to simulate residual stress of welding process. The rate and true equilibrium Eulerian mechanical analysis obtain very similar longitudinal residual stress results, as shown in Figures 4.23 and 4.24. To further compare the stress results of different analysis methods, the longitudinal residual stress along plot surface P are plotted in Figure 4.25. The residual stress results for all these four analysis are very close. These indicate that: 1) the true equilibrium Eulerian analysis is accurate in predicting residual stress of coupled thermo-mechanical procedures; 2) the true equilibrium and rate equilibrium can obtain the same residual stress, if there is no velocity boundary conditions applied in the down stream of the inlet surface.
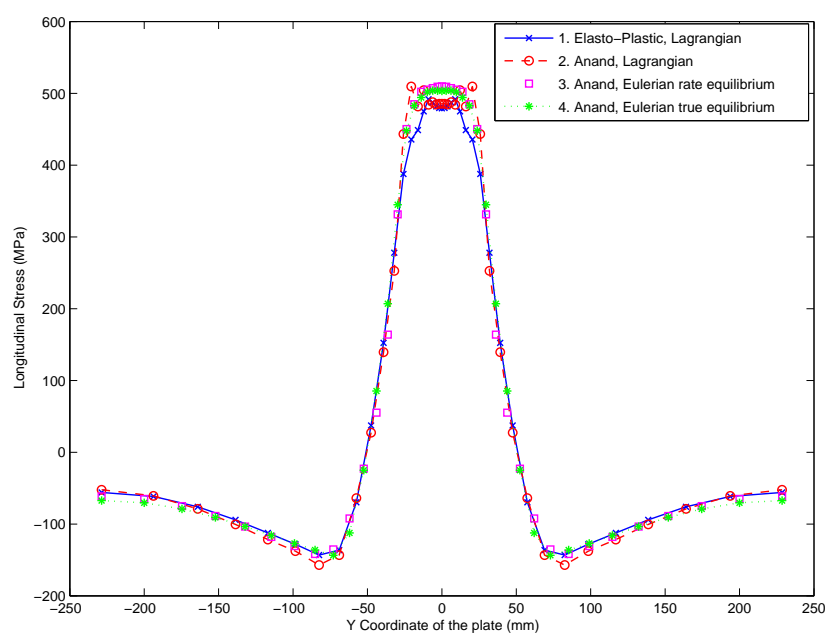
Fig. 4.25.   Compare results

4.6 Conclusions

A new four-field (velocity, total deformation gradient, viscoplastic part of deformation gradient and internal variable) mixed Eulerian elasto-viscoplastic formulation suitable for modeling the deformation, material flow, and residual stress in quasi-steady processes has been presented in this paper. The rate-dependent Anand's constitutive equation is introduced to allow a smooth transition from mostly elastic to actively yielding response. This formulation is stabilized by the Streamline Upwind Petrov-Galerkin (SUPG) method and is implemented in a four node quadrilateral element and can be solved by Newton Raphson method with a progressively stiffening algorithm.

Three numerical models (disturbed flow, strip drawing and Gas metal arc Welding) are performed to demonstrate the accuracy of the true equilibrium method and show the difference between the true equilibrium method and the rate equilibrium method. The disturbed flow and strip drawing models show that the true equilibrium method can obtain more accurate results than rate equilibrium method if there are velocity boundary conditions applied in the down stream of the inlet surface. The Gas metal arc welding model shows that the results from the true and rate equilibrium method are similar, if there is no velocity boundary conditions applied in the down stream of the inlet surface.

Chapter 5

Themo-Elasto-Visco-plastic Modeling

of Friction Stir Welding

5.1 Introduction

Friction stir welding (FSW) is a new solid-state joining process invented in 1991 at The Welding Institute (TWI). A non-consumable rotational cylindrical tool with a pin is used to heat and soften the workpieces. The heat is generated from two sources: (a) the friction between the tool and the workpieces, and (b) the plastic deformation of the workpieces. The tool pin stirs the heated material and joins two plates which are aligned together and clamped using fixtures. In general, it is expected that the residual stress in a FSW welded plate is lower than in a plate welded by traditional welding technology, because the highest temperature in FSW is lower. However, recent publications indicate the residual stress in FSW may be comparable to those of Gas Metal Arc Welding [11, 12]. Therefore, it is important to investigate the residual stress in FSW.

Modeling of FSW poses a considerable challenge due to the very large deformations involved in the process. If a Lagrangian reference frame is implemented, the large deformations result in severe mesh distortion and entanglement, necessitating continuous adaptive re-meshing, which of over time will lead to numerical errors. Typically, for problems exhibiting very large deformations an Arbitrary Lagrangian Eulerian approach is used instead of a pure Lagrangian to minimize the error caused by mesh distortion [65, 74].

Due to the difficulty of dealing with mesh distortion, most investigators using a Lagrangian modeling approach ignore the material flow and instead assume that residual stress and distortion in FSW are caused by thermal expansion only [26, 27, 28, 29, 12, 30]. The temperature distribution is provided by either a pure conduction analysis using a distributed heat input model [26, 27, 28, 29, 12, 30] or a thermal transport analysis [31] which may account for the effect of material flow on temperature distribution. These models are similar to the elasto-plastic models used in modeling residual stress and distortion in arc welding. Their main limitation is that they neglect the contribution of spinning material flow in the residual stress formation which produces an unsymmetric residual stress distribution [11, 12].

The significant material deformation and entanglement in friction stir welding make an Eulerian reference frame a more suitable alternative than a Lagrangian frame since in an Eulerian frame, the material is not attached to the mesh but it rather flows through it. Therefore, there is no issue with mesh entanglement as in a Lagrangian mesh. Early research using Eulerian frames for material processing includes modeling drawing and rolling processes [35, 44]. The constitutive model used in an Eulerian model can

have a significant effect on the modeling effort. If a history dependent response model is used such as an elasto-plastic or elasto-visco-plastic, it is necessary to compute the deformation history of each particle in order to determine stress and strain. This can be accomplished by either computing the streamline of each particle [32] or by computing material evolution in a weak FEA (mixed) formulation [32, 33, 34]. The streamline integration methods for elasto-plastic or elaso-visco-plastic models do not allow for the computation of global algorithmic tangent stiffness leading to convergence difficulties, while the mixed FEA formulations lead to systems with large number of degrees of freedom. Due to these modeling difficulties most investigators neglect history evolution in Eulerian models by assuming visco-plastic material response [33]. Such material models may be sufficient at the high temperatures near the stirring zone. However, they are not appropriate for lower temperatures and result into zero residual stress distortion.

Qin and Michaleris [34, 73, 42] have developed two Eulerian elasto-visco-plastic formulations. The first formulation is based on the rate of equilibrium and the second on the true equilibrium equation. Both formulations have been implemented in a 2D reference frame and have been verified by comparing Lagrangian elasto-plastic and Eulerian elasto-visco-plastic results in arc welding. Although the formulation based on the rate equilibrium equation is easier to implement, the true equilibrium equation uses conventional boundary conditions and accounts for temperature dependent material properties.

In the present study, an Eulerian thermo-elasto-visco-plastic model is developed to compute residual stress in FSW. The model accounts for plasticity caused by both thermal expansion and mechanical deformation due to material spinning. Because the temperature of the material near the tool pin is close to its melting temperature, the

material in this region can be treated as an incompressible visco-plastic flow. Thus, a coupled thermo-visco-plastic analysis is performed in this region to provide thermal and velocity boundary conditions in an elasto-visco-plastic analysis that is performed afterwards. In the region outside the tool shoulder, the material response is treated as elasto-visco-plastic and is modeled by the Anand's constitutive law [37]. The true equilibrium Eulerian elasto-visco-plastic formulation [42] is used in this work to predict the residual stress of FSW by coupling the velocity, deformation gradient, visco-plastic deformation gradient and internal variable together.

5.2 Governing Equations

In this work, two sets of governing equations are used to simulate the Friction Stir Welding process. A coupled thermo-visco-plastic analysis is performed first to compute temperature and material flow around the spinning tool. An elasto-visco-plastic analysis is then performed to predict the residual stress. The governing equations for the coupled thermo-visco-plastic analysis and the elasto-visco-plastic analysis are listed in this section.

5.2.1 Coupled thermo-visco-plastic analysis

Heat transfer and visco-plastic governing equations are coupled to model temperature and material flow in an Eulerian frame.

5.2.1.1   Equilibrium equation

Assuming that the inertia terms and body forces are negligible, the momentum balance equation reduces to the following equilibrium equation:

$$\frac{\partial \sigma_{ij}}{\partial x_i} = 0 \tag{5.1}$$

where, σ_{ij} is the Cauchy stress tensor and $\mathbf{x}$ is the spacial coordinate. The visco-plastic stress-strain relationship can be expressed by:

$$\sigma'_{ij} = 2\mu D_{ij} \tag{5.2}$$

and, μ is the viscosity of the material, and D_{ij} is the strain rate of the material flow, which can be obtained by:

$$D_{ij} = \frac{1}{2}\left(L_{ij} + L_{ji}\right) \tag{5.3}$$

with L_{ij} is the velocity gradient:

$$L_{ij} = \frac{\partial v_i}{\partial x_j} \tag{5.4}$$

where, $\mathbf{v}$ is the velocity.

5.2.1.2   Incompressibility

For incompressibility, the trace of the strain rate tensor is zero:

$$trace(\mathbf{D}) = D_{ii} = 0 \tag{5.5}$$

5.2.1.3   Internal variable evolution

Anand's constitutive model [37] is used to describe the material hardening during the welding process by constitutive functions $g(\tilde{\sigma}, s)$ and $f(\tilde{\sigma}, s)$ described in Section 5.3.1.

$$\dot{s} = g(\tilde{\sigma}, s) \tag{5.6}$$

5.2.1.4   Energy balance equation

For a quasi-steady state problem in an Eulerian frame, the energy balance equation is expressed as [69, 70, 71, 72],

$$\rho C_p \, v_i \frac{\partial T}{\partial x_i} = -\frac{\partial q_i}{\partial x_i} + Q \tag{5.7}$$

where ρ is the density of the material, C_p is the specific heat capacity, T is the temperature, Q is the internal heat generation rate and q_i is the heat flux vector.

5.2.2 Elasto-visco-plastic analysis

The velocity ($\mathbf{v}$), total deformation gradient ($\mathbf{F}$), visco-plastic part of deformation gradient ($\mathbf{F}^{vp}$) and internal variable ($\mathbf{s}$) are solved simultaneously to compute residual stress in the elasto-visco-plastic analysis. The governing equations for these variables are:

5.2.2.1 Equilibrium equation

Similarly to the coupled thermo-visco-plastic analysis the equilibrium equation is

$$\frac{\partial \sigma_{ij}}{\partial x_i} = 0 \tag{5.8}$$

In the elasto-visco-plastic analysis, it is assumed that stress in a deformed material depends on both elastic deformation and viscoplasic material flow. Therefore, the stress and strain relationship is written as:

$$\sigma_{ij} = C_{ijkl} E^e_{kl} + 2\mu D_{ij} \tag{5.9}$$

where, C_{ijkl} is the fourth order isotropic elasticity tensor, μ is the viscosity. The elastic strain tensor E^e_{ij} can be derived by:

$$E^e_{ij} = \frac{1}{2} \left(\delta_{ij} - F^{e-1}_{ki} F^{e-1}_{kj} \right) \tag{5.10}$$

The elastic part of deformation gradient tensor F^e_{ij} in Equation (5.10) can be obtained by the decomposition of the total deformation gradient tensor F_{ij} :

$$F^e_{ij} = F_{ik} \, F^{\theta-1}_{kl} \, F^{vp-1}_{lj} \tag{5.11}$$

in which the thermal deformation gradient tensor can be computed by [75]:

$$F^\theta_{ij} = \upsilon(\theta)\delta_{ij} \tag{5.12}$$

The scalar $\upsilon(\theta)$ is the thermal stretch ratio in any material direction.

5.2.2.2 Deformation gradient integration formulation

The deformation gradient **F** is integrated throughout the domain by:

$$\dot{F}_{ij} = \upsilon_k \frac{\partial F_{ij}}{\partial x_k} = L_{ik} \, F_{kj} \tag{5.13}$$

5.2.2.3 Visco-plastic deformation gradient integration

The visco-plastic portion of the deformation gradient $\mathbf{F}^{vp}$ is integrated throughout the domain by:

$$\dot{F}^{vp}_{ij} = \upsilon_k \frac{\partial F^{vp}_{ij}}{\partial x_k} = D^{vp}_{ik} F^{vp}_{kj} \tag{5.14}$$

where the visco-plastic strain rate tensor D^{vp}_{ij} is:

$$D^{vp}_{ij} = \sqrt{\frac{3}{2}}\dot{\tilde{\varepsilon}}^{vp} N_{ij} \qquad (5.15)$$

in which $\dot{\tilde{\varepsilon}}^{vp}$ is the equivalent visco-plastic strain rate defined by the constitutive function $f(\tilde{\sigma}, s)$. N_{ij} is the direction of plastic flow tensor given by:

$$\dot{\tilde{\varepsilon}}^{vp} = f(\tilde{\sigma}, s) \qquad (5.16)$$

$$N_{ij} = \sqrt{\frac{3}{2}}\frac{\sigma'_{ij}}{\tilde{\sigma}} \qquad (5.17)$$

with the equivalent tensile stress $\tilde{\sigma}$ defined by:

$$\tilde{\sigma} = \sqrt{\frac{3}{2}\sigma'_{ij}\sigma'_{ij}} \qquad (5.18)$$

and, the Cauchy stress deviator σ'_{ij} by:

$$\sigma'_{ij} = \sigma_{ij} - \frac{1}{3}\sigma_{kk}\delta_{ij} \qquad (5.19)$$

5.2.2.4 Internal variable evolution formulation

Similarly to the coupled thermo-visco-plastic analysis the internal variable evolution is

$$\dot{s} = v_k \frac{\partial s}{\partial x_k} = g(\tilde{\sigma}, s) \tag{5.20}$$

5.3 Coupled thermo-mechanical analysis of Friction Stir Welding

5.3.1 Friction Stir Welding Model
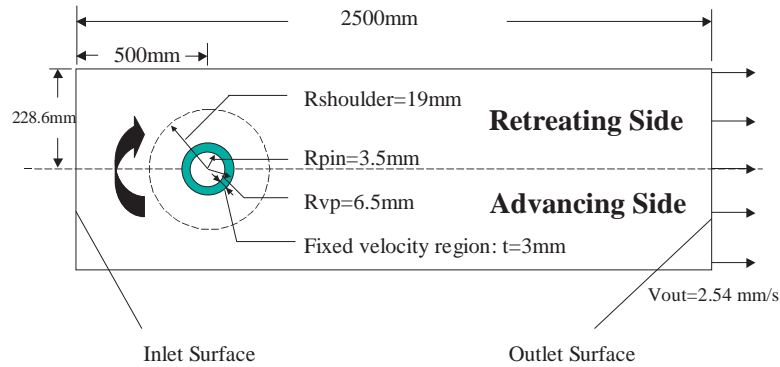

Fig. 5.1. Friction Stir Welding Model

In this work, the FSW process described in Reference [6] is simulated using a 2-dimensional FEA model in an Eulerian reference frame. The material flows through a fixed 2-dimensional spacial domain with an impenetrable circular region, which represents the tool pin. The workpiece enters this domain from the inlet surface at a speed of

$2.54mm/s$, and leaves the domain through the outlet surface. The radii of tool pin and tool shoulder are $R_{pin} = 3.5mm$ and $R_{shoulder} = 19mm$, respectively. The material is assumed to stick with the tool pin and partially stick with the tool shoulder in the region around the tool pin. Thus, a fixed velocity boundary condition is applied around the tool pin. To compute the residual stress, the length of the spatial domain is set to be $2500mm$ to let the temperature to cool down to room temperature at the outlet surface. The tool spins clockwise at a rotational speed of 750 rpm. Therefore, the top half of the region is the retreating side, and the bottom half of the region is the advancing side.

Anand's model [37] can be used to simulate temperature dependent material deformation with both low and high strain rates [76]. Therefore, both visco-plastic and elasto-visco-plastic analysis adopt Anand's model as their constitutive law. The constitutive functions $f(\tilde{\sigma}, s)$ in Equation (2.15) is given by:

$$\dot{\tilde{\varepsilon}}^{vp} = f(\tilde{\sigma}, s) = A \left(sinh \left(\xi \frac{\tilde{\sigma}}{s} \right) \right)^{\frac{1}{m}} \tag{5.21}$$

where $A = A_0 \cdot exp(-Q/RT)$, Q is the thermal activation energy, R is the ideal gas constant, and T is the absolute temperature. A_0, ξ and m are the material parameters listed in Table 2.1.

The internal variable evolution Equation (2.5), defined by the function $g(\tilde{\sigma}, s)$, is chosen to be [37]:

$$g(\tilde{\sigma}, s) = h_0 \left| \left(1 - \frac{s}{s^*} \right) \right|^a sign \left(1 - \frac{s}{s^*} \right)$$

$$\cdot A \left(sinh \left(\xi \frac{\tilde{\sigma}}{s} \right) \right)^{\frac{1}{m}} \tag{5.22}$$

Material Parameter	Value
A_0	$6.34 * 10^{11} s^{-1}$
Q	312.35 KJ/mole
ξ	3.25
R	8.314
m	0.1956
a	1.5
n	0.06869
$\tilde{s}$	125.1 MPa
s_0	80 MPa
h_0	3093.1 MPa

Table 5.1. Material Parameters for HSLA-65 steel

with,

$$s^* \;=\; \tilde{s} \left(\frac{\dot{\bar{\varepsilon}}^{vp}}{A} \right)^n \tag{5.23}$$

5.3.2 Solution Method

An in-house OMP FORTRAN 90 computer program is used to solve the FSW model. To simulate this FSW model, the spacial domain is divided into two subdomains along the VP-EVP boundary (circle **T**) between the fixed velocity region and the tool shoulder, as shown in Figure 5.3. The region between the VP-EVP boundary and the tool pin is the visco-plastic region, and the region outside the VP-EVP boundary is the elasto-visco-plastic region. In this analysis, the following assumptions are introduced in the model:

- The material in the viscoplasic region is considered to be incompressible and has only visco-plastic response. Therefore the elastic deformation gradient $\mathbf{F}^e$ is identity in this region.

- The material in the elasto-plastic region is compressible, and the material properties are temperature dependent. The variation of elastic modulus, Poisson's ratio and thermal expansion by temperature are plotted in Figure 5.2.

- The strain rate of material flow in the elasto-visco-plastic region is assumed to be much smaller than the strain rate in the visco-plastic region. Thus, the effect of elasto-visco-plastic material flow on the results in the visco-plastic region is negligible.
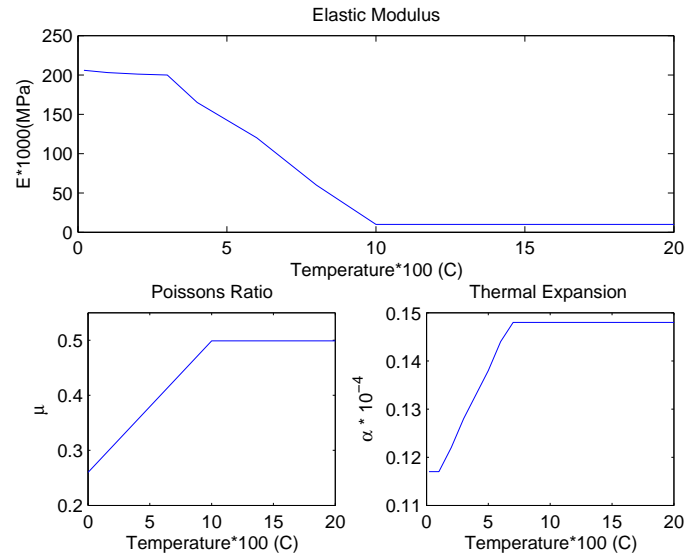
Fig. 5.2. Material Properties

Based on the above assumptions, the thermal analysis need to be coupled with the visco-plastic analysis only, because the heat generated by plastic deformation in elasto-visco-plastic region is negligible. Thus, the FSW model can be solved in the following steps, as shown in Figure 5.3.

- Step 1: Coupled thermo-visco-plastic analysis for the full domain.

  In the first step, the velocity ($\mathbf{v}$), pressure (P), internal variable (s) and temperature (T) are solved in the complete domain using the fully coupled thermo-visco-plastic analysis described in Section 5.2.1.

- Step 1.5: Transition step.

  Since the unknown variables are different between the visco-plastic and elasto-visco-plastic analysis, a transition step is needed to provide the necessary boundary conditions for the elasto-visco-plastic analysis. Because both analysis types solve for velocity and internal variable, the results of these two unknown variables can be transferred from the visco-plastic analysis to the elasto-visco-plastic analysis directly. However the visco-plastic analysis can not provide the boundary conditions for the total deformation gradient $\mathbf{F}$ and visco-plastic deformation gradient $\mathbf{F}^{vp}$. The thermal deformation gradient can be computed from the temperature results by Equation (5.12). Since the elastic deformation gradient $\mathbf{F}^{e}$ is assumed to be identity, the total deformation gradient and visco-plastic deformation gradient on the VP-EVP boundary can be given as:

$$\mathbf{F} = \mathbf{I} \tag{5.24}$$

$$\mathbf{F}^{vp} = \mathbf{F}^{\theta-1} \tag{5.25}$$

- Step 2: Elasto-visco-plastic analysis for the EVP domain.

  The second step is performed to compute the residual stress by solving the velocity($\mathbf{V}$), deformation gradient ($\mathbf{F}$), visco-plastic deformation gradient ($\mathbf{F}^{vp}$) and internal variable ($\mathbf{s}$) equations defined in Section 5.2.2. The temperature results of the first step are used as thermal loads.

5.3.3 Boundary conditions

Since the coupled thermo-visco-plastic and elasto-visco-plastic analysis solve for different unknown fields, their boundary conditions are different.

5.3.3.1 Coupled thermo-visco-plastic analysis

The heat generation of the FSW process consists of two parts: a) the frictional heat generated between the tool and the workpieces, b) the heat generated by plastic deformation. The surface frictional heat flux can be expressed as [77]:

$$q_{frictional} = \eta\mu pv = \frac{2\eta\mu F\omega}{60(R^2_{shoulder} - R^2_{pin})} r$$

$$(R_{pin} \leq r \leq R_{shoulder}) \tag{5.26}$$
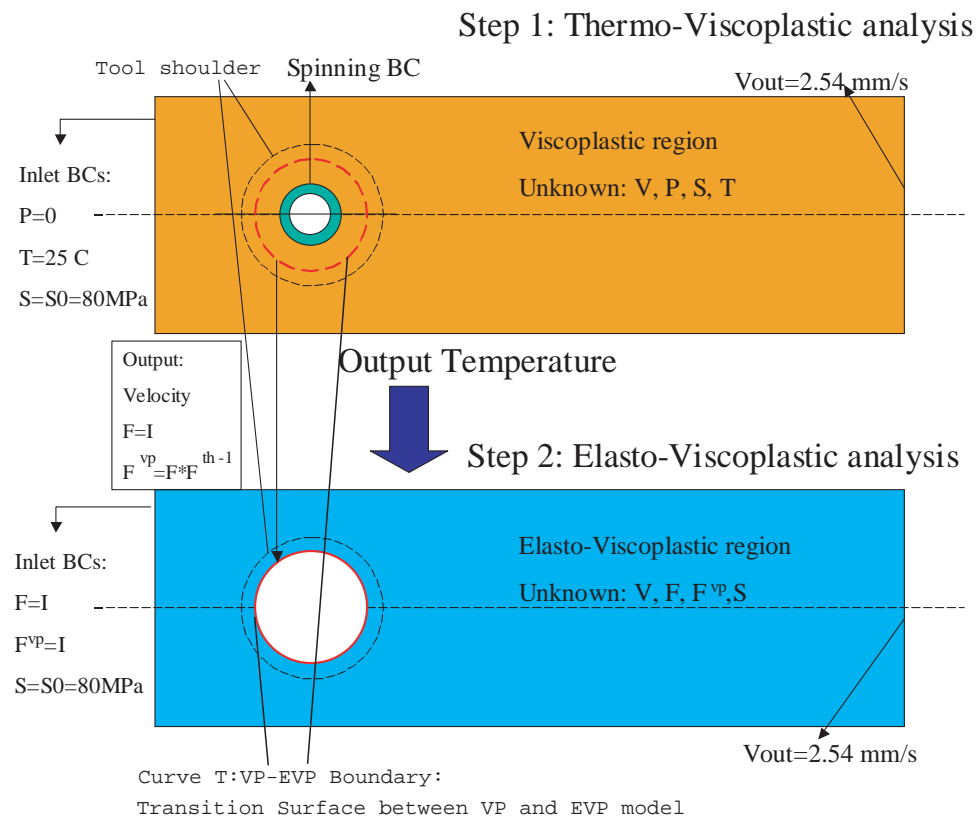
Fig. 5.3.   Solution procedure

where, η is the mechanical efficiency, μ is the friction coefficient, F and p are the force and pressure applied by the tool shoulder. The heat generated by the plastic flow can be calculated by:

$$q_{plastic} = \eta \sigma'_{ij} \dot{\epsilon}^{vp}_{ij} \tag{5.27}$$

The material is assumed to be undeformed on the inlet boundary. Thus the following boundary conditions are applied to the visco-plastic analysis:

- Inlet boundary

$$P = 0 MPa \tag{5.28}$$

$$s = s_0 = 80 MPa \tag{5.29}$$

$$T = 25^\circ C \tag{5.30}$$

- Outlet boundary

$$v_x = v_{weld} = 2.4 mm/s \tag{5.31}$$

$$v_y = 0 \tag{5.32}$$

- Fixed velocity boundary $(R_{pin} \leq r \leq R_{fixed})$

$$v_{fix} = (1 - \delta)wr \tag{5.33}$$

$$v_x = v_{fix} * \sin \alpha \tag{5.34}$$

$$v_y = -v_{fix} * \cos \alpha \tag{5.35}$$

The friction slip parameter δ is [78]:

$$\delta = 1 - \exp(-\frac{1}{\delta_0} \frac{r}{R_{pin}}) \tag{5.36}$$

with $\delta_0 = 0.4$.

5.3.3.2 Elasto-visco-plastic analysis

The temperature results of the coupled thermo-visco-plastic analysis are applied as thermal loading to the elasto-visco-plastic analysis. The boundary conditions for the inlet surface and outlet surface are similar to the visco-plastic analysis, and can be obtained by:

- Inlet boundary

$$\mathbf{F} = \mathbf{I} \tag{5.37}$$

$$\mathbf{F}^{vp} = \mathbf{I} \tag{5.38}$$

$$s = s_0 = 80 MPa \tag{5.39}$$

- Outlet boundary

$$v_x = v_{weld} = 2.4 mm/s \tag{5.40}$$

$$v_y = 0 \tag{5.41}$$

At the VP-EVP boundary (Curve T in Figure 5.3), the velocity $\mathbf{v}$, visco-plastic component of the deformation gradient $\mathbf{F}^{vp}$, and internal variable s computed from the thermo-visco-plastic analysis are applied as boundary conditions to the elasto-visco-plastic analysis. Thus, introducing the mechanical plasticity due to spinning in the residual stress computation.

$$\mathbf{v} = \mathbf{v}^{vp} \qquad (5.42)$$
$$At \ \ node$$
$$\mathbf{F} = \mathbf{I} \qquad (5.43)$$
$$\mathbf{F}^{vp} = \mathbf{F}^{\theta-1} \qquad (5.44)$$
$$s = s^{vp} \qquad (5.45)$$
$$At \ \ node$$

5.3.4 Results and discussion

5.3.4.1 Temperature and velocity from Thermo-visco-plastic analysis

Figure 5.4 shows the enlarged contour plot of the velocity norm around the tool pin. The velocity norm along the plot line P is plotted in Figures 5.5 and 5.6. A finer scale is used in Figure 5.6 to illustrate magnitude of the velocity beyond the tool vicinity. In Reference [4], the authors observed that the thickness of the rotational zone is three times thicker than the distance that the pin moves in one revolution, which is $1.14mm$ in this case. Figure 5.5 shows that the velocity decreases from $233mm/s$ to the weld velocity ($2.54mm/s$) in a very thin region with less than $1.5mm$ thickness. It also noted in Figure 5.6 that the velocity norm in advancing side is smaller than in retreating side.
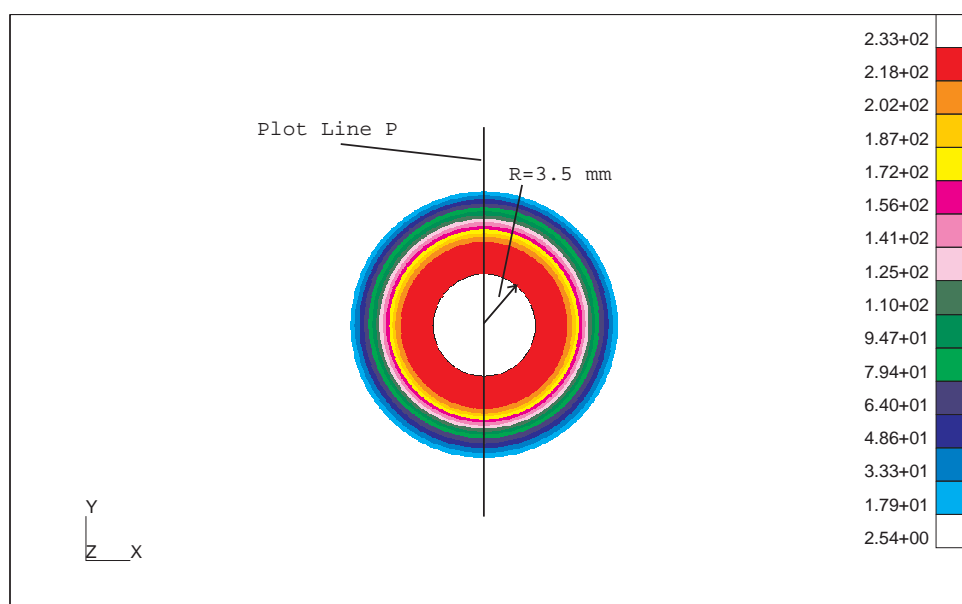
Fig. 5.4. Contour Plot of Velocity (Enlarged Around the Tool Pin)
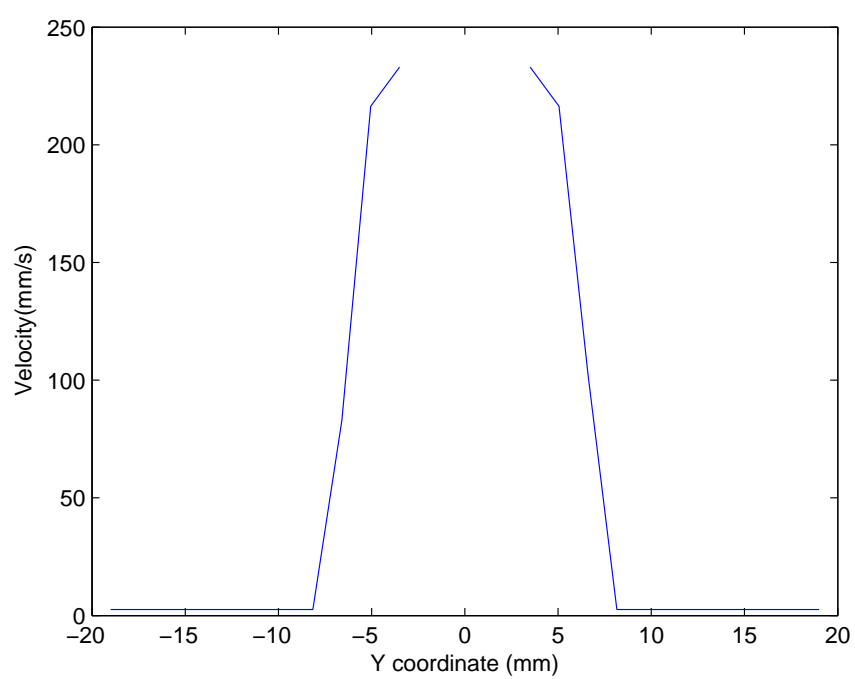
Fig. 5.5.   Plot of Velocity
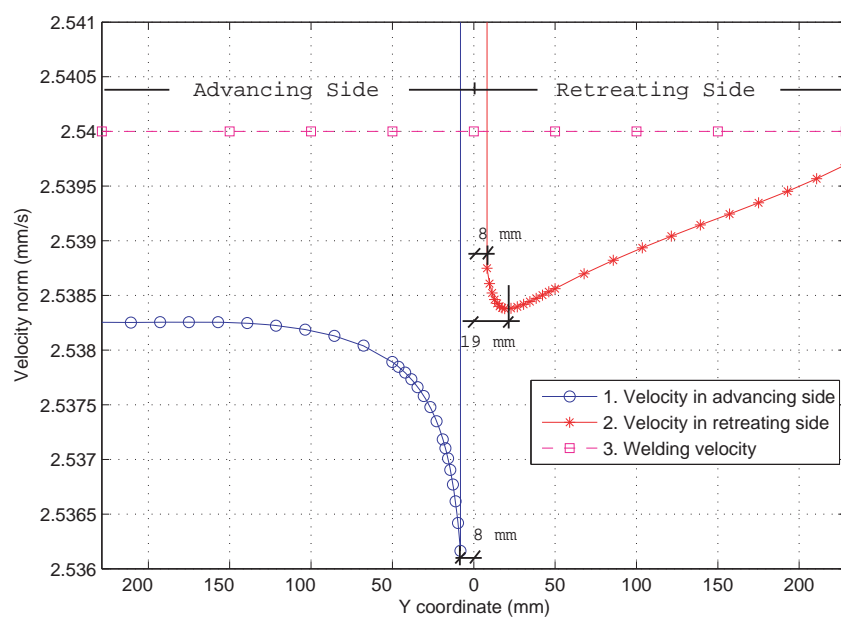
Fig. 5.6.   Plot of Velocity at a fine scale

This due to the fact that the direction of material flow in the advancing side is against the tool spinning direction.

The temperature distribution is also asymmetric. Figure 5.7 shows the contour plot of the temperature results of the coupled thermo-visco-plastic analysis, and Figure 5.8 shows the enlarged temperature distribution around the tool pin. The asymmetry temperature distribution is prominent around the spinning tool, because the velocity change is large in this region. The predicted highest temperature of the FSW model is $935^{\circ}C$ around the tool pin, and is in the advancing side. This indicates that the combined effect of frictional heat and the heat generated by plastic deformation soften the specimens and heat the materials around the tool pin without melting them.

5.3.4.2 Residual Stress

Figure 5.9 shows the contour plot of the longitudinal component (along the weld center line) of the computed stress. The asymmetric distribution of the stress can be observed from the plot. Because the temperature around the outlet surface drops down to the room temperature, the computed stress at the outlet surface can be treated as the residual stress.

The X component residual stress along the outlet surface is plotted in line 1 of Figure 5.10. The non-symmetric distribution of the residual stress along the outlet surface can be observed from this plot. The measured longitudinal stress is also plotted in Figure 5.10. The $'*'$ points and the $'o'$ points are the measured residual stress on the top and bottom surface of the plate, respectively. The averaged residual stress of the measured data is plotted in line 4. By comparing the calculated results and the measured
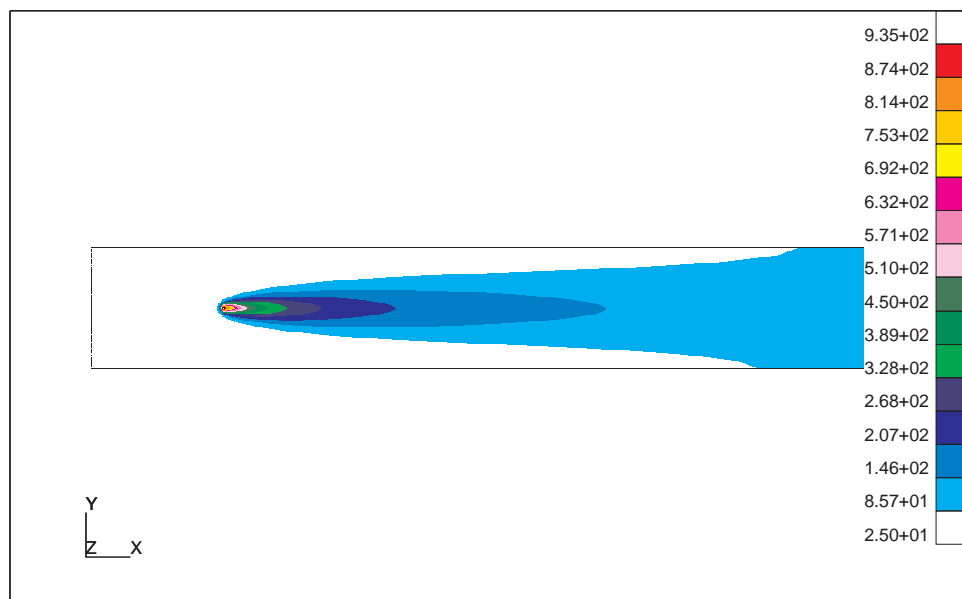
Fig. 5.7.   Contour Plot of Temperature Results
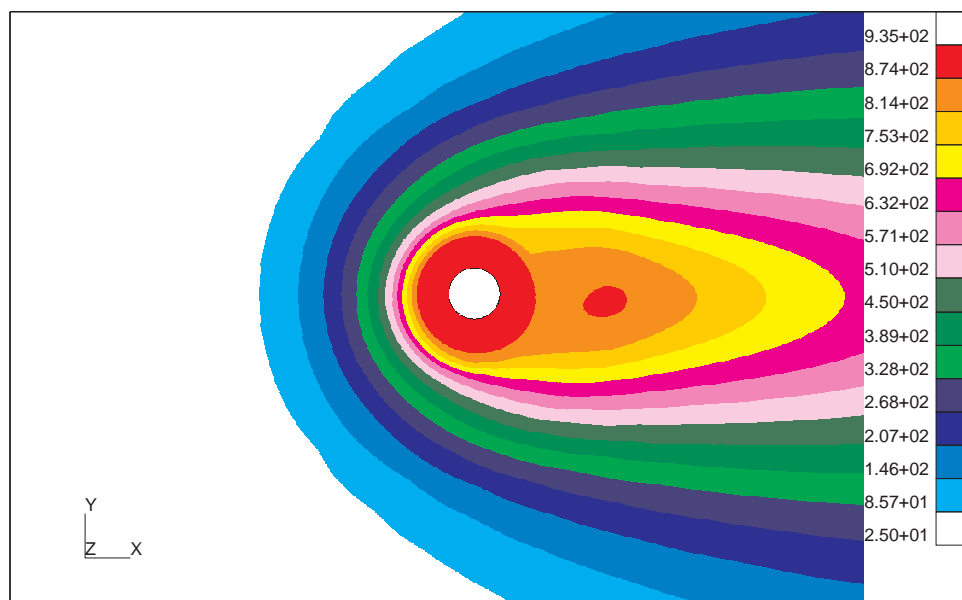

Fig. 5.8.   Contour Plot of Temperature (Enlarged Around the Tool Pin)

data, the following can be concluded: (a) The highest longitudinal residual stress for both computed and measured results of FSW model is in the advancing side. (b) The difference between the highest compression and tensile stress are higher in advancing side than in retreating side. (c) The highest compressive stress in advancing side is $50MPa$ higher than that of the retreating side.

5.3.4.3 Effect of spinning velocity on residual stress

Since this FSW model accounts for plasticity induced by both thermal expansion and mechanical deformation due to material spinning, FSW model is simulated under different spinning velocities to investigate the effect of spinning velocity on the residual stress distribution. Because the spinning velocity can effect the amount of the heat generated by the plastic flow, the heat generated by plastic deformation for the case of $750RPM$ spinning speed is applied to all the other cases to ensure the total heat input is the same among all cases. The FSW model is performed using the following spinning velocities: no spinning (0 RPM), 200 RPM, 400 RPM and 750 RPM. The longitudinal residual stress results along the outlet surface are plotted in Figure 5.11. The asymmetry of the residual stress increases as the spinning speed increasing from zero to $400RPM$. However, the difference between the results with 400 RPM and 750 RPM spinning speed is small. This indicates that spinning of the tool causes the asymmetry in the residual stress distribution. However, once the rotation speed reaches a certain value, the degree of asymmetry does not increase as the spinning speed increase. Reynolds et al. also observed this phenomenon in Reference [79].
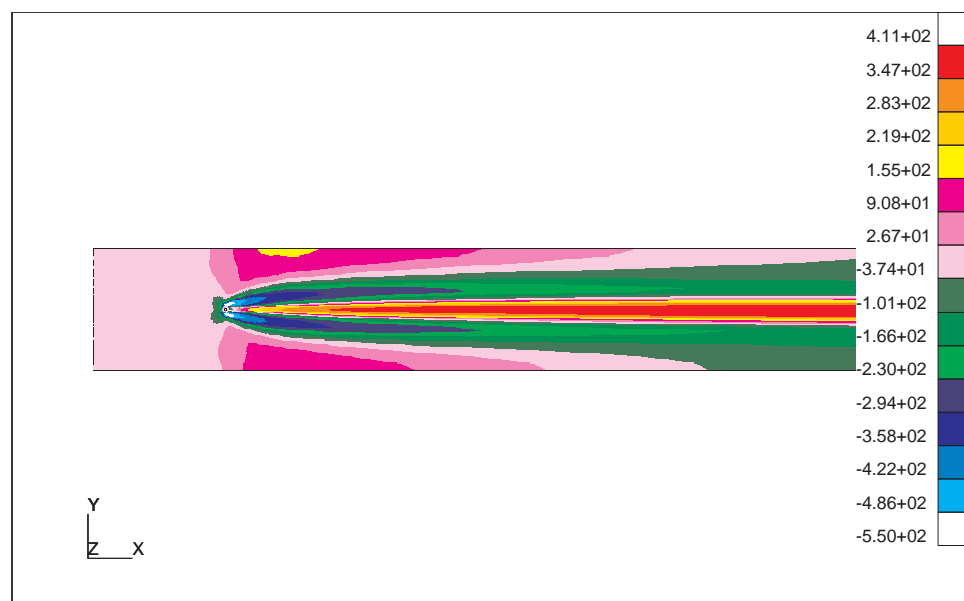
Fig. 5.9.   Contour plot of X Component Stress
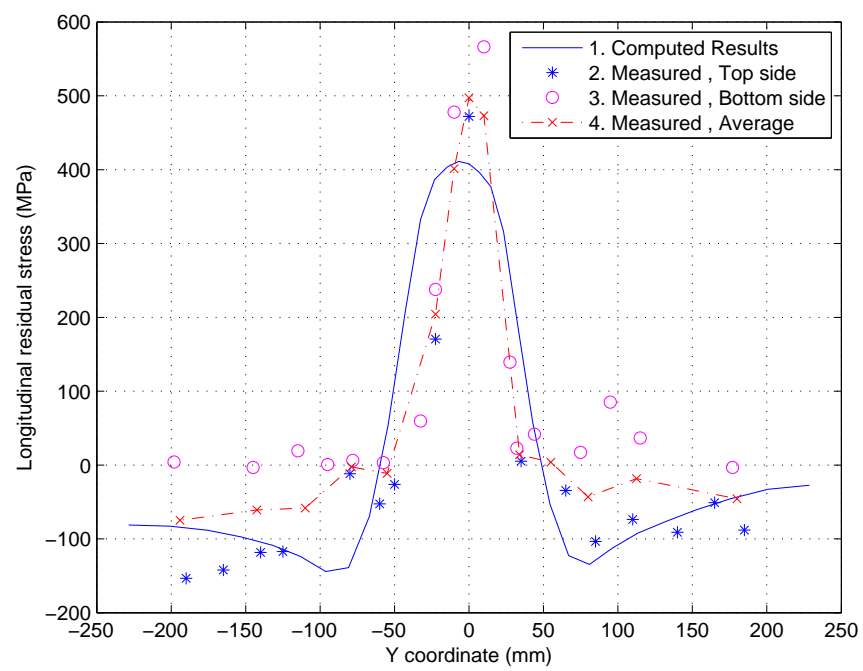
Fig. 5.10.   Longitudinal residual stress
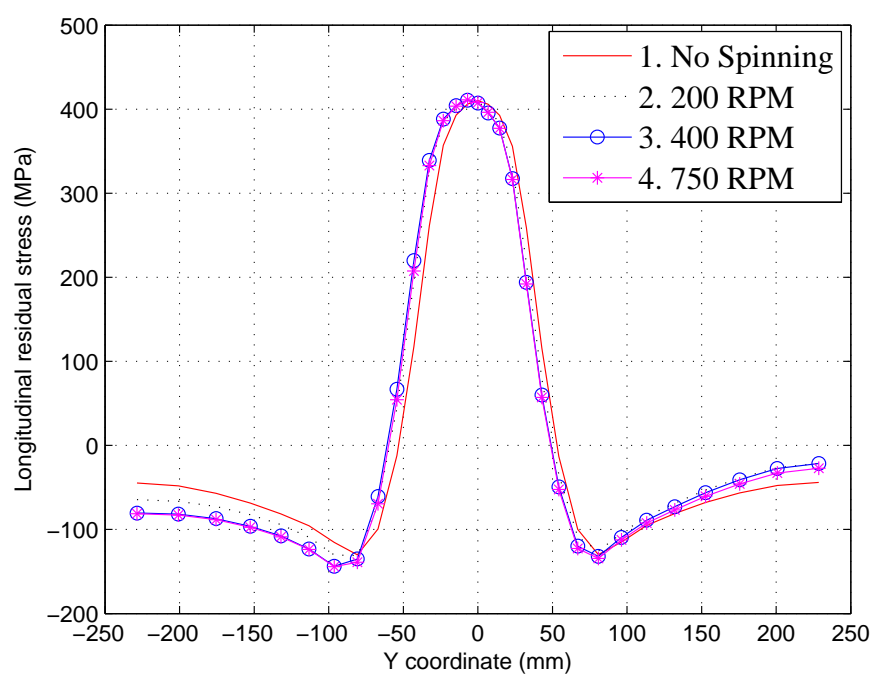
Fig. 5.11.   Effect of Spinning Velocity

5.3.4.4 Effect of visco-plastic zone size

As shown in Figure 5.3, the VP-EVP boundary is randomly selected between the fixed velocity boundary and the tool shoulder. It is necessary to investigate the influence of the selection of the VP-EVP boundary on the residual stress results. The longitudinal residual stress with different sizes of visco-plastic region is plotted in Figure 5.12. As the radius of the visco-plastic region reduces from 22 mm to 11 mm, the difference between the longitudinal residual stress become smaller. The residual stress results with 11 mm (line 1) and 12 mm (line 2) visco-plastic radius are almost the same. Thus, 11 mm can be treated as the convergence radius, which indicates that residual stress results won't change as the visco-plastic radius becomes smaller than 11 mm. In Figure 5.13, the solid lines 1, 3 and 5 plot the residual stress at retreating side points A ($Y = 7$ mm), B ($Y = 96$ mm) and C ($Y = 228$ mm) as the radius of VP-EVP region changes from 11 mm to 22 mm. Similarly, the dashed lines 2, 4 and 6 plot the residual stress at A_1 ($Y = -7$ mm), B_1 ($Y = -96$ mm) and C_1 ($Y = -228$ mm) in the advancing side. It is noted that the advancing side has larger stress gradient than the retreating side. The difference of residual stress between the advancing side and retreating side tends to decrease as the radius of VP-EVP region increases. However the change of the difference is very small within 11 $mm < R_{VP-EVP} < 17$ mm. Thus, reliable residual stress results can be obtained, if the radius of VP-EVP region satisfies:

$$1/2(R_{shoulder} - R_{pin}) < R_{VP-EVP} < 3/4(R_{shoulder} - R_{pin}).$$
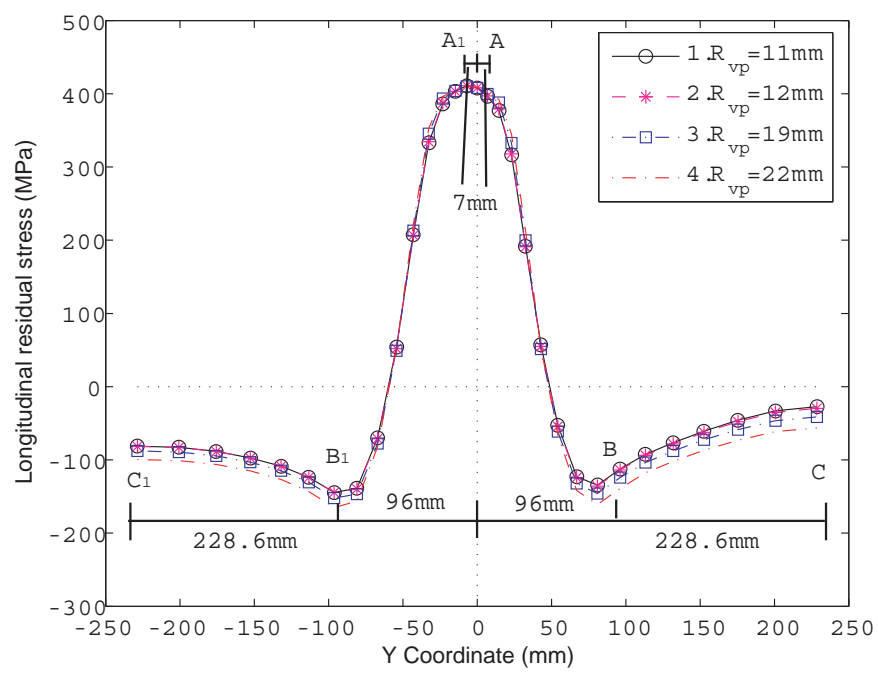
Fig. 5.12.   Residual stress results with different Visco-plastic Zone Size

Fig. 5.13.   Effect of Visco-plastic Zone Size

5.4 Conclusions

A two dimensional coupled thermo-elasto-visco-plastic FSW model has been presented in this paper. Both frictional heat and plastic deformation heat generation are considered in the model. Currently, this is the only known model that is capable of computing residual stress accounting for plasticity caused by both thermal expansion and mechanical deformation due to material spinning. The calculated residual stress results are compared with measured data, and good agreement is obtained. Based on the simulation results, the following conclusions can be drawn:

- The proposed coupled thermo-visco-plastic model can simulate temperature and material flow. The temperature and velocity distribution is non-symmetric. The highest temperature is around the tool pin and in the advancing side.

- The model is able to accurately compute the non-symmetric residual stress distribution of FSW.

- The highest tensile and compressive longitudinal residual stress are in advancing side. Thus the advancing side has higher stress gradient than retreating side.

Since the numerical implementation in this work is 2-dimensional, the though thickness material flow and residual stress distribution can not be computed. Extension of proposed thermo-elasto-visco-plastic method into a 3-dimensional implementation will enable evaluating the effects of tool geometry and through thickness material movement in the residual stress formation in FSW.

Chapter 6

Conclusions

Two sets of Eulerian formulations are introduced in this work to predict residual stress. One is based on the rate equilibrium equation and the other one is based on the true equilibrium equation. The rate equilibrium Eulerian formulation couples velocity ($\mathbf{V}$), stress ($\boldsymbol{\sigma}$) deformation gradient ($\mathbf{F}$) and internal variable ($\mathbf{s}$), while the true equilibrium Eulerian formulation solves for the velocity ($\mathbf{V}$), deformation gradient ($\mathbf{F}$), viscoplastic deformation gradient ($\mathbf{F}^{vp}$) and internal variable ($\mathbf{s}$) simultaneously. Both methods introduce Streamline Upwind Petrov-Galerkin (SUPG) method to stabilize convection terms in their formulation. Both formulations are implemented in a 4-node quadrilateral element and tested by a radial flow model, a disturbed flow model and a strip drawing model to verify their accuracy. The true equilibrium is shown to be able to obtain more accurate results and have simpler boundary conditions than the rate equilibrium. Coupled thermo-mechanical analysis of gas metal arc welding example is also performed by both methods. Their results have a good match with results from a Lagrangian analysis using elasto-plastic model. These indicate that both of these two methods can be used to accurately model thermo-elasto-viscoplastic material flow. The

true equilibrium is more suitable for solving cases with velocity boundary conditions applied in the downstream of the inlet surface.

A two dimensional coupled thermo-elasto-visco-plastic FSW model based on true equilibrium Eulerian formulation has been presented in Chapter 5. Both frictional heat and plastic deformation heat generation are considered in the model. Currently, this is the only known model that is capable of computing residual stress accounting for plasticity caused by both thermal expansion and mechanical deformation due to material spinning. The calculated residual stress results are compared with measured data, and good agreement is obtained. Based on the simulation results, the following conclusions can be drawn:

- The proposed coupled thermo-visco-plastic model can simulate temperature and material flow. The temperature and velocity distribution is non-symmetric. The highest temperature is around the tool pin and in the advancing side.

- The model is able to accurately compute the non-symmetric residual stress distribution of FSW.

- The highest tensile and compressive longitudinal residual stress are in advancing side. Thus the advancing side has higher stress gradient than retreating side.

Since the numerical implementation in this work is 2-dimensional, the though thickness material flow and residual stress distribution can not be computed. Extension of proposed thermo-elasto-visco-plastic method into a 3-dimensional implementation will enable evaluating the effects of tool geometry and through thickness material movement in the residual stress formation in FSW.

Appendix A

Rate of Almansi Strain

Almansi strain is defined as:

$$E^a_{ij} \;=\; \frac{1}{2}\left(I - F^{-1}_{ki}\, F^{-1}_{kj}\right)$$

Therefore, the time derivative of Almansi strain is

$$\dot{E}^a_{ij} \;=\; -\frac{1}{2}\left(\dot{F}^{-1}_{ki}\, F^{-1}_{kj} + F^{-1}_{ki}\, \dot{F}^{-1}_{kj}\right) \tag{A.1}$$

Since,

$$\dot{F}^{-1}_{ij} \;=\; -F^{-1}_{ik}\, \dot{F}_{kl}\, F^{-1}_{lm} \tag{A.2}$$

$$\;=\; -F^{-1}_{ik}\, L_{kj}\, F_{jl}\, F^{-1}_{lm} \tag{A.3}$$

$$\;=\; -F^{-1}_{ik}\, L_{kj} \tag{A.4}$$

Substitution of Equation (A.4) into Equation (A.1) results to the following expression of the rate of Almansi strain:

$$\dot{E}^{a}_{ij} = \frac{1}{2}(L_{ki} F^{-1}_{lk} F^{-1}_{lj} + F^{-1}_{ki} F^{-1}_{kl} L_{lj}) \tag{A.5}$$

Appendix B

FE Discretization

B.1 Field Variable Interpolators

In a 4 node quadrilateral element, the coordinates of a point within the element can be interpolated by the shape functions N_i and the coordinates of nodes x_i and y_i:

$$\left[\begin{array}{c} x \\ y \end{array} \right] = \left[\begin{array}{c} \sum_i N_i x_i \\ \sum_i N_i y_i \end{array} \right] \qquad i = 1, 2, 3, 4 \qquad (B.1)$$

Because the element is isoparametric, the same shape functions can be used to interpolate the velocity, stress, deformation gradient and internal variable:

$$v_i = N^v_{ij} U^v_j \qquad (B.2)$$

$$\vec{\sigma}_i = N^\sigma_{ij} U^\sigma_j \qquad (B.3)$$

$$\vec{F}_i = N^F_{ij} U^F_i \qquad (B.4)$$

$$s_i = N^s_i U^s_j \qquad (B.5)$$

where, U^v_i, U^σ_i, U^F_i and U^s_i are the velocity, stress, deformation gradient and internal variable of the node. N^v_{ij}, N^σ_{ij}, N^F_{ij} and N^s_i are corresponding shape functions defined by:

$$\mathbf{N}^v = [\mathbf{N}^b_1 \ \mathbf{N}^b_2 \ \mathbf{N}^b_3 \ \mathbf{N}^b_4] \qquad (B.6)$$

$$\mathbf{N}^\sigma = [\mathbf{N}^c_1 \ \mathbf{N}^c_2 \ \mathbf{N}^c_3 \ \mathbf{N}^c_4] \qquad (B.7)$$

$$\mathbf{N}^F = [\mathbf{N}^c_1 \ \mathbf{N}^c_2 \ \mathbf{N}^c_3 \ \mathbf{N}^c_4] \qquad (B.8)$$

$$\mathbf{N}^s = [\mathbf{N}^a_1 \ \mathbf{N}^a_2 \ \mathbf{N}^a_3 \ \mathbf{N}^a_4] \qquad (B.9)$$

where $\mathbf{N}^a_i$, $\mathbf{N}^b_i$ and $\mathbf{N}^c_i$ are:

$$\mathbf{N}^a_i = \begin{bmatrix} N_i \end{bmatrix}; \qquad \mathbf{N}^b_i = \begin{bmatrix} N_i & 0 \\ 0 & N_i \end{bmatrix}; \qquad \mathbf{N}^c_i = \begin{bmatrix} N_i & 0 & 0 & 0 \\ 0 & N_i & 0 & 0 \\ 0 & 0 & N_i & 0 \\ 0 & 0 & 0 & N_i \end{bmatrix} \qquad (B.10)$$

B.2 Gradient Interpolators

The spatial derivatives can be evaluated as:

$$\frac{\partial \Phi}{\partial x}_j = J^{-1}_{ij} \frac{\partial \Phi}{\partial r}_j \tag{B.11}$$

The Jacobian $\mathbf{J}$ of the mapping from the global coordinate $\mathbf{X}$ to the reference coordinate $\mathbf{r}$ is evaluated by:

$$J_{ij} = \frac{\partial x_i}{\partial r_j} = \frac{\partial N_{ik}}{\partial r_j} X_k \tag{B.12}$$

In this manner, the gradient interpolator $\mathbf{B}^s$ for the scalar s in a matrix form is:

$$\mathbf{B}^s = \begin{bmatrix} J^{-1}_{11} & J^{-1}_{12} \\ J^{-1}_{21} & J^{-1}_{22} \end{bmatrix} \begin{bmatrix} N_{1,\xi} & N_{2,\xi} & N_{3,\xi} & N_{4,\xi} \\ N_{1,\eta} & N_{2,\eta} & N_{3,\eta} & N_{4,\eta} \end{bmatrix} \tag{B.13}$$

where, ξ and η are the coordinates in the reference frame. The velocity gradient interpolator $\mathbf{B}^{v}$ can be obtained by:

$$
\mathbf{B}^{v} = \begin{bmatrix}
B^{s}_{11} & 0 & B^{s}_{12} & 0 & B^{s}_{13} & 0 & B^{s}_{14} & 0 \\
B^{s}_{21} & 0 & B^{s}_{22} & 0 & B^{s}_{23} & 0 & B^{s}_{24} & 0 \\
0 & B^{s}_{11} & 0 & B^{s}_{12} & 0 & B^{s}_{13} & 0 & B^{s}_{14} \\
0 & B^{s}_{21} & 0 & B^{s}_{22} & 0 & B^{s}_{23} & 0 & B^{s}_{24}
\end{bmatrix}
\tag{B.14}
$$

The gradient interpolators $\mathbf{B}^{\sigma}$ and $\mathbf{B}^{F}$ for stress and deformation gradient are three dimensional matrices, which can be obtained from:

$$
\mathbf{B}^{\sigma} = \mathbf{B}^{F} = \begin{bmatrix} \underline{\mathbf{B}}^{4}_{1} & \underline{\mathbf{B}}^{4}_{2} & \underline{\mathbf{B}}^{4}_{3} & \underline{\mathbf{B}}^{4}_{4} \end{bmatrix}
\tag{B.15}
$$

where, $\underline{\mathbf{B}}^{4}_{i}$ is a $4 \times 4 \times 2$ three dimensional matrix:

$$
\underline{\mathbf{B}}^{4}_{i\,lmn} = \begin{cases} B^{s}_{in} & if \ \ l = m, \\ 0 & if \ \ l \neq m \end{cases}
\tag{B.16}
$$

Furthermore, the gradient interpolators $\mathbf{B}^L$ for the matrix L^M_{ij}, which is defined

in Equation (2.33), is also a three dimensional matrix:

$$
B^L_{ijk} = \begin{cases}
B^L_{11k} = B^L_{33k} = B^v_{1k} \\
B^L_{12k} = B^L_{34k} = B^v_{3k} \\
B^L_{21k} = B^L_{43k} = B^v_{2k} \qquad\qquad k = 1...8 \\
B^L_{22k} = B^L_{44k} = B^v_{4k} \\
B^L_{13k} = B^L_{14k} = B^L_{23k} = B^L_{24k} = B^L_{31k} = B^L_{32k} = B^L_{41k} = B^L_{42k} = 0
\end{cases}
\tag{B.17}
$$

Appendix C

The Jacobian Matrix of the Rate of Elastic Strain

The rate of elastic strain for a two dimensional plain strain problem can be expressed in the vector form as:

$$\dot{\mathbf{E}}^e = \left[\begin{array}{cccc} \dot{\vec{E}}^e & \dot{\vec{E}}^e & \vec{D}^e & \dot{\vec{E}}^e \\ {}_1 & {}_2 & {}_3 & {}_4 \end{array} \right]^T \tag{C.1}$$

where,

$$\dot{\vec{E}}^e_i = T^{L^a}_{ij} \, \tilde{L}^a_j \tag{C.2}$$

with,

$$\mathbf{T}^{L^a} = \left[\begin{array}{cccc} 1 & 0 & 0 & 0 \\ 0 & 0 & 0 & 1 \\ 0 & 0 & 0 & 0 \\ 0 & 1 & 1 & 0 \end{array} \right] \tag{C.3}$$

$$\tilde{\mathbf{L}}^a = \begin{bmatrix} L^a_{xx} & L^a_{yx} & L^a_{xy} & L^a_{yy} \end{bmatrix}^T \tag{C.4}$$

$$L^a_{ij} = F^{-1}_{ki} F^{-1}_{kl} L^e_{lj} \tag{C.5}$$

$$L^e_{ij} = L_{ij} - L^{th}_{ij} - L^{vp}_{ij} \tag{C.6}$$

Therefore, the Jacobian matrix of the rate of elastic strain vector can be obtained as:

$$\frac{\partial \dot{E}^e_i}{\partial U_j} = \begin{cases} \dfrac{\partial \dot{E}^e_i}{\partial U_j} = \dfrac{\partial \dot{\vec{E}}^e_i}{\partial U_j} & i = 1, 2, 4 \\[2ex] \dfrac{\partial \dot{E}^e_i}{\partial U_j} = \dfrac{\partial \dot{\vec{D}}^e_i}{\partial U_j} & i = 3 \end{cases} \tag{C.7}$$

C.1 Expression of $\dfrac{\partial \dot{\vec{E}}^e_i}{\partial U_j}$ in Equation (C.7)

$$\frac{\partial \dot{\vec{E}}^e_i}{\partial U_j} = T^{L^a}_{ij} \frac{\partial \tilde{L}^a_i}{\partial U_j} \tag{C.8}$$

To derive $\dfrac{\partial \tilde{L}^a_i}{\partial U_j}$, the vector $\tilde{L}^e_i$, h and the matrix F^a_{ij} need to be introduced:

$$\tilde{\mathbf{L}}^e = \begin{bmatrix} L^e_{xx} & L^e_{yx} & L^e_{xy} & L^e_{yy} \end{bmatrix}^T \tag{C.9}$$

$$\mathbf{h} \;=\; \begin{bmatrix} 1 & 1 & 1 & 0 \end{bmatrix}^T \tag{C.10}$$

$$\mathbf{F}^a = \begin{bmatrix} f^a_{11} & f^a_{12} & 0 & 0 \\ f^a_{21} & f^a_{22} & 0 & 0 \\ 0 & 0 & f^a_{11} & f^a_{12} \\ 0 & 0 & f^a_{21} & f^a_{22} \end{bmatrix} \tag{C.11}$$

where,

$$f^a_{ij} = F^{-1}_{ki}\, F^{-1}_{kj} \tag{C.12}$$

Thus, $\tilde{L}^a_i$ can be expressed as:

$$\tilde{L}^a_i = F^a_{ij}\, \tilde{L}^e_i \tag{C.13}$$

Hence, the Jacobian matrix of $\tilde{L}^a_i$ can be obtained as:

$$\frac{\partial \tilde{L}^a_i}{\partial U^V_j} \;=\; F^a_{il} \left(B^v_{lj} - \alpha\, h_l\, N^v_{kj}\, \frac{\partial T}{\partial x_k} \right) \tag{C.14}$$

$$\frac{\partial \tilde{L}^a_i}{\partial U^F_j} = \frac{\partial F^a_{ik}}{\partial U^F_j} L^e_k \tag{C.15}$$

$$\frac{\partial \tilde{L}^a_i}{\partial U^\sigma_j} = F^a_{ik} \cdot -\frac{3}{2}\left[\frac{\partial f(\tilde{\sigma},s)}{\partial U^\sigma_j} \frac{G_{kp}\,\bar{\sigma}'_p}{\tilde{\sigma}} \right.$$
$$\left. + f(\tilde{\sigma},s)\left(\frac{M_{kp}\,N^\sigma_{pj}}{\tilde{\sigma}} - \frac{3}{2}\frac{G_{kp}\,\bar{\sigma}'_p}{\tilde{\sigma}^3}N^\sigma_{mj}\, M_{lm}\, Q_{ls}\, G_{st}\, \bar{\sigma}'_t \right)\right] \tag{C.16}$$

$$\frac{\partial \tilde{L}^a_i}{\partial U^s_j} = F^a_{ik} \cdot -\left[\frac{3}{2}\frac{\partial f(\tilde{\sigma},s)}{\partial U^s}\frac{G_{kp}\,\bar{\sigma}'_p}{\tilde{\sigma}}\right]_j \tag{C.17}$$

The term $\dfrac{\partial F^a_{ik}}{\partial U^F_j}$ in Equation (C.15) is computed as:

$$\frac{\partial F^a_{ik}}{\partial U^F_j} = \frac{\partial F^a_{ik}}{\partial \tilde{F}^{-1}_p}\,\frac{\partial \tilde{F}^{-1}_p}{\partial U^F_j} \tag{C.18}$$

where,

$$\tilde{F}^{-1}_i = \frac{1}{\det \mathbf{F}}\, T^{F^{-1}}_{ik}\, \tilde{F}_k \tag{C.19}$$

with,

$$\tilde{\mathbf{F}}^{-1} = \begin{bmatrix} F^{-1}_{xx} \\ F^{-1}_{yx} \\ F^{-1}_{xy} \\ F^{-1}_{yy} \end{bmatrix} \quad ; \quad \tilde{\mathbf{F}} = \begin{bmatrix} F_{xx} \\ F_{yx} \\ F_{xy} \\ F_{yy} \end{bmatrix} \quad ; \quad \mathbf{T}^{F^{-1}}_{ij} = \begin{bmatrix} 0 & 0 & 0 & 1 \\ 0 & -1 & 0 & 0 \\ 0 & 0 & -1 & 0 \\ 1 & 0 & 0 & 0 \end{bmatrix} \tag{C.20}$$

Thus, $\dfrac{\partial \tilde{F}^{-1}_i}{\partial U^F_j}$ in Equation (C.18) can be derived by:

$$\frac{\partial \tilde{F}^{-1}_i}{\partial U^F_j} = -\frac{1}{\det^2 \mathbf{F}} \frac{\partial \det \mathbf{F}}{\partial \tilde{F}_p} N^F_{pj} T^{F^{-1}}_{ik} \tilde{F}_k + \frac{1}{\det \mathbf{F}} T^{F^{-1}}_{ik} N^F_{kj} \tag{C.21}$$

with,

$$\frac{\partial \det \mathbf{F}}{\partial \tilde{F}_p} = \begin{bmatrix} F_{yy} & -F_{xy} & -F_{yx} & F_{xx} \end{bmatrix} \tag{C.22}$$

Since,

$$\frac{\partial f^a_{11}}{\partial \tilde{F}^{-1}_i} = \begin{bmatrix} 2 * F^{-1}_{xx} & 2 * F^{-1}_{yx} & 0 & 0 \end{bmatrix} \tag{C.23}$$

$$\frac{\partial f^a_{12}}{\partial \tilde{F}^{-1}_i} = \frac{\partial f^a_{21}}{\partial \tilde{F}^{-1}_i} = \left[\begin{array}{cccc} F^{-1}_{xy} & F^{-1}_{yy} & F^{-1}_{xx} & F^{-1}_{yx} \end{array} \right] \qquad (C.24)$$

$$\frac{\partial f^a_{22}}{\partial \tilde{F}^{-1}_i} = \left[\begin{array}{cccc} 0 & 0 & 2*F^{-1}_{xy} & 2*F^{-1}_{yy} \end{array} \right] \qquad (C.25)$$

according to Equations (C.23)-(C.25) and (C.11), the three dimensional matrix $\dfrac{\partial F^a_{ij}}{\partial \tilde{F}^{-1}_k}$ in Equation (C.18) can be written as:

$$\frac{\partial F^a_{ij}}{\partial \tilde{F}^{-1}_k} = \begin{cases} \dfrac{\partial F^a_{11}}{\partial \tilde{F}^{-1}_k} = \dfrac{\partial F^a_{33}}{\partial \tilde{F}^{-1}_k} = \dfrac{\partial f^a_{11}}{\partial \tilde{F}^{-1}_k} \\[4mm] \dfrac{\partial F^a_{12}}{\partial \tilde{F}^{-1}_k} = \dfrac{\partial F^a_{34}}{\partial \tilde{F}^{-1}_k} = \dfrac{\partial F^a_{21}}{\partial \tilde{F}^{-1}_k} = \dfrac{\partial F^a_{43}}{\partial \tilde{F}^{-1}_k} = \dfrac{\partial f^a_{12}}{\partial \tilde{F}^{-1}_k} \\[4mm] \dfrac{\partial F^a_{22}}{\partial \tilde{F}^{-1}_k} = \dfrac{\partial F^a_{44}}{\partial \tilde{F}^{-1}_k} = \dfrac{\partial f^a_{22}}{\partial \tilde{F}^{-1}_k} \\[4mm] \dfrac{\partial F^a_{13}}{\partial \tilde{F}^{-1}_k} = \dfrac{\partial F^a_{14}}{\partial \tilde{F}^{-1}_k} = \dfrac{\partial F^a_{23}}{\partial \tilde{F}^{-1}_k} = \dfrac{\partial F^a_{24}}{\partial \tilde{F}^{-1}_k} = \dfrac{\partial F^a_{31}}{\partial \tilde{F}^{-1}_k} = \dfrac{\partial F^a_{32}}{\partial \tilde{F}^{-1}_k} = \dfrac{\partial F^a_{41}}{\partial \tilde{F}^{-1}_k} = \dfrac{\partial F^a_{42}}{\partial \tilde{F}^{-1}_k} = 0 \end{cases} \qquad (C.26)$$

C.2   Expression of $\dfrac{\partial \vec{D}^e_3}{\partial U_j}$ in Equation (C.7)

$$\frac{\partial \vec{D}^e_3}{\partial U^v_j} \; = \; \alpha \, h_3 \, N^v_{kj} \, \frac{\partial T}{\partial x_k} \tag{C.27}$$

$$\frac{\partial \vec{D}^e_3}{\partial U^\sigma_j} \; = \; -\frac{3}{2} \left[\frac{\partial f(\tilde{\sigma}, s)}{\partial U^\sigma_j} \frac{G_{3p} \, \bar{\sigma}'_p}{\tilde{\sigma}} \right]$$

$$+\frac{3}{2} \left[f(\tilde{\sigma}, s) \left(\frac{M_{3p} \, N^\sigma_{pj}}{\tilde{\sigma}} - \frac{3}{2} \frac{G_{3p} \, \bar{\sigma}'_p}{\tilde{\sigma}^3} N^\sigma_{mj} \, M_{lm} \, Q_{ls} \, G_{st} \, \bar{\sigma}'_t \right) \right] \tag{C.28}$$

$$\frac{\partial \vec{D}^e_3}{\partial U^F_j} \; = \; 0 \tag{C.29}$$

$$\frac{\partial \vec{D}^e_3}{\partial U^s_j} \; = \; - \left[\frac{3}{2} \frac{\partial f(\tilde{\sigma}, s)}{\partial U^s_j} \frac{G_{3p} \, \bar{\sigma}'_p}{\tilde{\sigma}} \right] \tag{C.30}$$

Appendix D

FE Discretization

D.1 Field Variable Interpolators

In a 4 node quadrilateral element, the coordinates of a point within the element can be interpolated by the shape functions N_i and the coordinates of nodes x_i and y_i :

$$
\begin{bmatrix} x \\ y \end{bmatrix} = \begin{bmatrix} \sum_i N_i x_i \\ \sum_i N_i y_i \end{bmatrix} \qquad i = 1, 2, 3, 4 \tag{D.1}
$$

Because the element is isoparametric, the same shape functions can be used to interpolate the velocity, stress, deformation gradient and internal variable:

$$
v_i = N^v_{ij} U^v_j \tag{D.2}
$$

$$
\tilde{F}_i = N^F_{ij} U^F_i \tag{D.3}
$$

$$\tilde{F}^{vp}_i = N^{F^{vp}}_{ij} U^{F^{vp}}_i \tag{D.4}$$

$$s_i = N^s_i U^s_j \tag{D.5}$$

where, U^v_i, U^σ_i, U^F_i and U^s_i are the velocity, stress, deformation gradient and internal variable of the node. N^v_{ij}, N^σ_{ij}, N^F_{ij} and N^s_i are corresponding shape functions defined by:

$$\mathbf{N}^v = [\mathbf{N}^b_1 \ \mathbf{N}^b_2 \ \mathbf{N}^b_3 \ \mathbf{N}^b_4] \tag{D.6}$$

$$\mathbf{N}^F = [\mathbf{N}^c_1 \ \mathbf{N}^c_2 \ \mathbf{N}^c_3 \ \mathbf{N}^c_4] \tag{D.7}$$

$$\mathbf{N}^{F^{vp}} = [\mathbf{N}^d_1 \ \mathbf{N}^d_2 \ \mathbf{N}^d_3 \ \mathbf{N}^d_4] \tag{D.8}$$

$$\mathbf{N}^s = [\mathbf{N}^a_1 \ \mathbf{N}^a_2 \ \mathbf{N}^a_3 \ \mathbf{N}^a_4] \tag{D.9}$$

where $\mathbf{N}^a_i$, $\mathbf{N}^b_i$, $\mathbf{N}^c_i$ and $\mathbf{N}^c_i$ are:

$$N^a_{i\,lm} = N_i \delta_{lm} \quad i = 1; \ j = 1 \tag{D.10}$$

$$N^b_{i\,lm} = N_i \delta_{lm} \quad 1 \le i \le 2; \ 1 \le i \le 2 \tag{D.11}$$

$$N^c_{i\,lm} = N_i \delta_{lm} \quad 1 \le i \le 4; \ 1 \le i \le 4 \tag{D.12}$$

$$N^d_{i\,lm} = N_i \delta_{lm} \quad 1 \le i \le 5; \ 1 \le i \le 5 \tag{D.13}$$

D.2 Gradient Interpolators

The spatial derivatives can be evaluated as:

$$\frac{\partial \Phi}{\partial x_j} = J^{-1}_{ij} \frac{\partial \Phi}{\partial r_j} \tag{D.14}$$

The Jacobian $\mathbf{J}$ of the mapping from the global coordinate $\mathbf{X}$ to the reference coordinate $\mathbf{r}$ is evaluated by:

$$J_{ij} = \frac{\partial x_i}{\partial r_j} = \frac{\partial N_{ik}}{\partial r_j} X_k \tag{D.15}$$

In this manner, the gradient interpolator $\mathbf{B}^s$ for the scalar s in a matrix form is:

$$\mathbf{B}^s = \begin{bmatrix} J^{-1}_{11} & J^{-1}_{12} \\ J^{-1}_{21} & J^{-1}_{22} \end{bmatrix} \begin{bmatrix} N_{1,\xi} & N_{2,\xi} & N_{3,\xi} & N_{4,\xi} \\ N_{1,\eta} & N_{2,\eta} & N_{3,\eta} & N_{4,\eta} \end{bmatrix} \tag{D.16}$$

where, ξ and η are the coordinates in the reference frame. The velocity gradient interpolator $\mathbf{B}^v$ can be obtained by:

$$\mathbf{B}^v = \begin{bmatrix} B^s_{11} & 0 & B^s_{12} & 0 & B^s 13 & 0 & B^s_{14} & 0 \\ B^s_{21} & 0 & B^s_{22} & 0 & B^s_{23} & 0 & B^s_{24} & 0 \\ 0 & B^s_{11} & 0 & B^s_{12} & 0 & B^s_{13} & 0 & B^s_{14} \\ 0 & B^s_{21} & 0 & B^s_{22} & 0 & B^s_{23} & 0 & B^s_{24} \end{bmatrix} \tag{D.17}$$

The gradient interpolators $\mathbf{B}^F$ for deformation gradient is a three dimensional matrix, which can be obtained from:

$$\mathbf{B}^F = \begin{bmatrix} \underline{\mathbf{B}}^4 1 & \underline{\mathbf{B}}^4 2 & \underline{\mathbf{B}}^4 3 & \underline{\mathbf{B}}^4 4 \end{bmatrix} \tag{D.18}$$

where, $\underline{\mathbf{B}}^4 i$ is a $4 \times 4 \times 2$ three dimensional matrix:

$$\underline{\mathbf{B}}^4 i_{lmn} = \begin{cases} B^s_{in} & if \ \ l = m, \\ 0 & if \ \ l \neq m \end{cases} \tag{D.19}$$

Similarly, the gradient interpolators $\mathbf{B}^{F^{vp}}$ for viscoplastic deformation gradient can also be obtained as:

$$\mathbf{B}^{F^{vp}} = \left[\begin{array}{cccc} \mathbf{B}^5_{\underline{1}} & \mathbf{B}^5_{\underline{2}} & \mathbf{B}^5_{\underline{3}} & \mathbf{B}^5_{\underline{4}} \end{array} \right] \tag{D.20}$$

where, $\mathbf{B}^5_{\underline{i}}$ is a $5 \times 5 \times 2$ three dimensional matrix:

$$\mathbf{B}^5_{\underline{i}\,lmn} = \begin{cases} B^s_{in} & \quad if \ \ l = m, \\ \\ 0 & \quad if \ \ l \neq m \end{cases} \tag{D.21}$$

Furthermore, the gradient interpolators $\mathbf{B}^L$ for the matrix L^M_{ij}, which is defined

in Equation (2.33), is also a three dimensional matrix:

$$B^L_{ijk} = \begin{cases} B^L_{11k} = B^L_{33k} = B^v_{1k} \\ B^L_{12k} = B^L_{34k} = B^v_{3k} \\ B^L_{21k} = B^L_{43k} = B^v_{2k} \qquad\qquad k = 1...8 \\ B^L_{22k} = B^L_{44k} = B^v_{4k} \\ B^L_{13k} = B^L_{14k} = B^L_{23k} = B^L_{24k} = B^L_{31k} = B^L_{32k} = B^L_{41k} = B^L_{42k} = 0 \end{cases} \tag{D.22}$$

Appendix E

Jacobian Matrix of Elastic Strain $\dfrac{\partial \bar{E}^e_i}{\partial U_j}$

E.1 Jacobian Matrix of Elastic Strain $\dfrac{\partial \bar{E}^e_i}{\partial U_j}$

Elastic strain vector $\bar{E}^e_i$ in engineering format can be expressed as:

$$
\bar{\mathbf{E}}^{\mathbf{e}} =
\begin{bmatrix}
E^e_{xx} \\
E^e_{yy} \\
E^e_{zz} \\
E^e_{xy}
\end{bmatrix}
=
\begin{bmatrix}
\frac{1}{2} - \frac{1}{2}({F^{e^{-1}}_{xx}}^2 + {F^{e^{-1}}_{yx}}^2) \\
\frac{1}{2} - \frac{1}{2}({F^{e^{-1}}_{xx}}^2 + {F^{e^{-1}}_{yx}}^2) \\
\frac{1}{2} - \frac{1}{2}({F^{e^{-1}}_{zz}})^2 \\
-(F^{e^{-1}}_{xx} F^{e^{-1}}_{xy} + F^{e^{-1}}_{yx} F^{e^{-1}}_{yy})
\end{bmatrix}
\tag{E.1}
$$

Because the elastic strain is not a function of velocity, the partial derivative of $\bar{E}^e_i$ with respect to velocity is:

$$\frac{\partial \bar{E}^e_i}{\partial U_j} = \begin{cases} \dfrac{\partial \bar{E}^e_i}{\partial U^v_j} = 0 \\[3em] \dfrac{\partial \bar{E}^e_i}{\partial U^F_j} = \dfrac{\partial \bar{E}^e_i}{\partial \tilde{F}^{e-1}_k} \dfrac{\partial \tilde{F}^{e-1}_k}{\partial \tilde{F}^e_p} \dfrac{\partial \tilde{F}^e_p}{\partial U^F_j} \\[3em] \dfrac{\partial \bar{E}^e_i}{\partial U^{F^{vp}}_j} = \dfrac{\partial \bar{E}^e_i}{\partial \tilde{F}^{e-1}_k} \dfrac{\partial \tilde{F}^{e-1}_k}{\partial \tilde{F}^e_p} \dfrac{\partial \tilde{F}^e_p}{\partial U^{F^{vp}}_j} \\[3em] \dfrac{\partial \bar{E}^e_i}{\partial U^s_j} = 0 \end{cases} \qquad (E.2)$$

where,

$$\frac{\partial \bar{E}^e_i}{\partial \tilde{F}^{e-1}_j} = - \begin{bmatrix} \tilde{F}^{e-1}_1 & \tilde{F}^{e-1}_2 & 0 & 0 & 0 \\ 0 & 0 & \tilde{F}^{e-1}_3 & \tilde{F}^{e-1}_4 & 0 \\ 0 & 0 & 0 & 0 & \tilde{F}^{e-1}_5 \\ \tilde{F}^{e-1}_3 & \tilde{F}^{e-1}_4 & \tilde{F}^{e-1}_1 & \tilde{F}^{e-1}_2 & 0 \end{bmatrix} \qquad (E.3)$$

By defining:

$$
\tilde{\mathbf{F}}_4^{\mathbf{e}^{-1}} = \begin{bmatrix} F_{xx}^{e^{-1}} \\ F_{yx}^{e^{-1}} \\ F_{xy}^{e^{-1}} \\ F_{yy}^{e^{-1}} \end{bmatrix} \;;\quad \tilde{\mathbf{F}}_4^{\mathbf{e}} = \begin{bmatrix} F_{xx}^{e} \\ F_{yx}^{e} \\ F_{xy}^{e} \\ F_{yy}^{e} \end{bmatrix} \;;\quad \mathbf{T}_{ij}^{F} = \begin{bmatrix} 0 & 0 & 0 & 1 \\ 0 & -1 & 0 & 0 \\ 0 & 0 & -1 & 0 \\ 1 & 0 & 0 & 0 \end{bmatrix} \tag{E.4}
$$

$\tilde{F}_i^{e^{-1}}$ can be computed as:

$$
\tilde{F}_{4\,i}^{\;e^{-1}} = -\frac{1}{\det \mathbf{F}_a^{\mathbf{e}}} T_{ij}^{F} \tilde{F}_{4\,j}^{\;e} \tag{E.5}
$$

in which,

$$
\det \mathbf{F}_a^{\mathbf{e}} = F_{xx}^{e}\, F_{yy}^{e} - F_{xy}^{e}\, F_{yx}^{e} \tag{E.6}
$$

$\dfrac{\partial \tilde{F}_{4\,i}^{\;e^{-1}}}{\partial \tilde{F}_{4\,j}^{\;e}}$ can be computed as:

$$
\frac{\partial \tilde{F}_{4\,i}^{\;e^{-1}}}{\partial \tilde{F}_{4\,j}^{\;e}} = -\frac{1}{\det^2 \mathbf{F}_a^{\mathbf{e}}} \frac{\partial \det \mathbf{F}_a^{\mathbf{e}}}{\partial \tilde{F}_{4\,j}^{\;e}} T_{ik}^{F} \tilde{F}_{4\,k}^{\;e} + \frac{1}{\det \mathbf{F}_a^{\mathbf{e}}} T_{ij}^{F} \tag{E.7}
$$

Thus, $\dfrac{\partial \tilde{F}^{e}{}_{i}^{-1}}{\partial \tilde{F}^{e}{}_{j}}$ is calculated by:

$$
\frac{\partial \tilde{F}^{e}{}_{i}^{-1}}{\partial \tilde{F}^{e}{}_{j}} = \begin{bmatrix} \dfrac{\partial \tilde{F}_{4}{}_{i}^{e\,-1}}{\partial \tilde{F}_{4}{}_{j}^{e}} & 0 \\ & \\ 0 & -F^{e}{}_{yy}^{\,-2} \end{bmatrix}
\tag{E.8}
$$

Elastic part of deformation gradient tensor F^{e}_{ij} can be computed from total deformation gradient tensor F_{ij} and viscoplastic part of deformation gradient tensor F^{vp}_{ij}. Their relationship in vector format can be expressed as:

$$
\tilde{F}^{e}_{j} = \begin{bmatrix} \tilde{F}_{4}{}^{e}_{j} \\ F^{vp-1}_{zz} \end{bmatrix}
\tag{E.9}
$$

where,

$$
\tilde{F}_{4}{}^{e}_{i} = F^{M}_{ij}\,\tilde{F}_{4}{}^{vp-1}_{j}
\tag{E.10}
$$

and,

$$
\tilde{\mathbf{F}}^{\mathbf{vp}^{-1}}_{4} = \begin{bmatrix} F^{vp^{-1}}_{xx} \\ F^{vp^{-1}}_{yx} \\ F^{vp^{-1}}_{xy} \\ F^{vp^{-1}}_{yy} \end{bmatrix} \quad ; \quad \mathbf{F}^{M} = \begin{bmatrix} F_{xx} & F_{xy} & 0 & 0 \\ F_{yx} & F_{yy} & 0 & 0 \\ 0 & 0 & F_{xx} & F_{xy} \\ 0 & 0 & F_{yx} & F_{yy} \end{bmatrix} \tag{E.11}
$$

Then, $\dfrac{\partial \tilde{F}^{e}_{i}}{\partial U^{F}_{j}}$ in Equation (E.2) can be computed by:

$$
\frac{\partial \tilde{F}^{e}_{i}}{\partial U^{F}_{j}} = \frac{\partial F^{M}_{ik}}{\partial U^{F}_{j}} \tilde{F}^{vp^{-1}}_{4\,k} \tag{E.12}
$$

$$
\frac{\partial \tilde{F}^{e}_{i}}{\partial U^{F}_{j}} = \begin{bmatrix} \dfrac{\partial \tilde{F}^{e}_{4\,i}}{\partial U^{F}_{j}} \\ 0 \end{bmatrix} = \begin{bmatrix} \dfrac{\partial F^{M}_{ik}}{\partial U^{F}_{j}} \tilde{F}^{vp^{-1}}_{4\,k} \\ 0 \end{bmatrix} \tag{E.13}
$$

where,

$$
\frac{\partial F^M_{ij}}{\partial U^F_k} = \begin{cases} \dfrac{\partial F^M_{11}}{\partial U^F_k} = \dfrac{\partial F^M_{33}}{\partial U^F_k} = N^F_{1k} \\[2ex] \dfrac{\partial F^M_{12}}{\partial U^F_k} = \dfrac{\partial F^M_{34}}{\partial U^F_k} = N^F_{3k} \\[2ex] \dfrac{\partial F^M_{21}}{\partial U^F_k} = \dfrac{\partial F^M_{43}}{\partial U^F_k} = N^F_{2k} \\[2ex] \dfrac{\partial F^M_{22}}{\partial U^F_k} = \dfrac{\partial F^M_{44}}{\partial U^F_k} = N^F_{4k} \\[2ex] \dfrac{\partial F^M_{13}}{\partial U^F_k} = \dfrac{\partial F^M_{14}}{\partial U^F_k} = \dfrac{\partial F^M_{23}}{\partial U^F_k} = \dfrac{\partial F^M_{24}}{\partial U^F_k} = \dfrac{\partial F^M_{31}}{\partial U^F_k} = \dfrac{\partial F^M_{32}}{\partial U^F_k} = \dfrac{\partial F^M_{41}}{\partial U^F_k} = \dfrac{\partial F^M_{42}}{\partial U^F_k} = 0 \end{cases} \quad k = 1...8 \tag{E.14}
$$

Similarly, $\dfrac{\partial \tilde{F}^e_i}{\partial U^{F^{vp}}_j}$ in Equation (E.2) can be obtained by:

$$
\frac{\partial \tilde{F}^e_i}{\partial U^{F^{vp}}_j} = \begin{bmatrix} \dfrac{\partial \tilde{F}^e_{4_i}}{\partial U^{F^{vp}}_j} \\[3ex] \dfrac{\partial \tilde{F}^e_{zz}}{\partial U^{F^{vp}}_j} \end{bmatrix} = \begin{bmatrix} \dfrac{\partial \tilde{F}^e_{4_i}}{\partial \tilde{F}^{vp^{-1}}_{4_k}} \dfrac{\partial \tilde{F}^{vp^{-1}}_{4_k}}{\partial \tilde{F}^{vp}_{4_m}} \dfrac{\partial \tilde{F}^{vp}_{4_m}}{\partial U^{F^{vp}}_j} \\[3ex] -F^{vp^{-2}}_{zz} \dfrac{\partial F^{vp}_{zz}}{\partial U^{F^{vp}}_j} \end{bmatrix} \tag{E.15}
$$

where,

$$
\frac{\partial \tilde{F}^e_{4_i}}{\partial \tilde{F}^{vp^{-1}}_{4_j}} = F^M_{ij} \tag{E.16}
$$

$$\frac{\partial \tilde{F}^{vp}{}^{-1}_{4\,i}}{\partial \tilde{F}^{vp}_{4\,j}} = -\frac{1}{\det^2 \mathbf{F^{vp}}} \frac{\partial \det \mathbf{F^{vp}}_a}{\partial \tilde{F}^{vp}_{4\,j}} T^F_{ik} \tilde{F}^{vp}_{4\,k} + \frac{1}{\det \mathbf{F^{vp}}_a} T^F_{ij}$$

(E.17)

with,

$$\det \mathbf{F^{vp}}_a = F^{vp}_{xx} F^{vp}_{yy} - F^{vp}_{xy} F^{vp}_{yx}$$

(E.18)

and,

$$\frac{\partial \tilde{F}^{vp}_{4\,i}}{\partial U^{F^{vp}}_j} = \mathbf{N}^{F^{vp}}_{4}$$

(E.19)

$$\frac{\partial \tilde{F}^{vp}_{zz}}{\partial U^{F^{vp}}_j} = \mathbf{N}^{F^{vp}}_{zz}$$

(E.20)

References

[1] G. LIU, L. E. MURR, C.-S. NIOU, J. C. MCCLURE, and F. R. VEGA. Microstructural aspects of the friction-stir welding of 6061-t6 aluminum. *Scripta materialia*, 37:355–361, 1997.

[2] W Tang, X Guo, JC McClure, LE Murr, and A Nunes. Heat input and temperature distribution in friction stir welding. *JOURNAL OF MATERIALS PROCESSING AND MANUFACTURING SCIENCE*, 2:163C172, 1998.

[3] Reynolds A.P. Visualization of material flow in an autogenous friction stir weld. *Science and Technology of Welding and Joining*, 5:120–124, 2000.

[4] M. Guerraa, C. Schmidta, J. C. McClurea, L. E. Murra, and A. C. Nunesb. Flow patterns during friction stir welding. *Materials Characterization*, 49:95–101, 2002.

[5] COLLIGAN K. Material flow behavior during friction stir welding of aluminum. *Welding journal*, 78:229–237, 1999.

[6] S. R. Bhide, P. Michaleris, M. Posada, and J. Deloach. Comparison of buckling distortion propensity for saw, gmaw, and fsw. *Welding journal*, 85:189–195, 2006.

[7] X.-L. Wang, Z. Feng, S. A. David, S. Spooner, and C. R. Hubbard. Neutron diffraction study of residual stresses in friction stir welds. *6th Int. Conf. on 'Residual stresses'*, 2:1408–1408, 2002.

[8] M A Sutton, B Yang, A P Reynolds, and R Taylor. Microstructural studies of friction stir welds in 2024-t3 aluminum. *Materials Science and Engineering A*, 323:160–166, 2002.

[9] Peel M., Steuwer A., Preuss M., and Withers P. J. Microstructure, mechanical properties and residual stresses as a function of welding speed in aluminium aa5083 friction stir welds. *Acta materialia*, 51:4791–4801, 2003.

[10] Woo Wanchuck, Choo Hahn, Brown Donald W., Bourke Mark A. M., Feng Zhili, David Stan A., Hubbard Camden R., and Liaw Peter K. Deconvoluting the influences of heat and plastic deformation on internal strains generated by friction stir processing. *Applied Physics Letters*, 86:64C69, 2005.

[11] S.R. Bhide, P. Michaleris, M. Posada, and J. DeLoach. Comparison of Buckling Distortion Propensity for SAW, GMAW, and FSW. *Welding Journal*, 85:189s–195s, 2006.

[12] Z. Feng, X.-L. Wang, S.A. David, and P.S. Sklad. Modeling of residual stress and property distibution in friction stir welds of aluminium ally 6061-T6. *Journal of Science and Technology in Welding and Joining*, 12:348–356, 2007.

[13] P. Tekriwal and J. Mazumder. Transient and Residual Thermal Strain-Stress Analysis of GMAW. *Journal of Engineering Materials and Technology*, 113:336–343, 1991.

[14] J. H. Argyris, J. Szimmat, and K. J. Willam. Computational Aspects of Welding Stress Analysis. *Computer Methods in Applied Mechanics and Engineering*, 33:635–666, 1982.

[15] H. Hibbitt and P. V. Marcal. A Numerical, Thermo-Mechanical Model for the Welding and Subsequent Loading of a Fabricated Structure. *Computers & Structures*, 3(1145-1174):1145–1174, 1973.

[16] H. J. Braudel, M. Abouaf, and J. L. Chenot. An Implicit and Incremental Formulation for the Solution of Elastoplastic Problems by the Finite Element Method. *Computers and Structures*, 22(5):801–814, 1986.

[17] J. M. J. McDill A. S. Oddy and J. A.Goldak. Consistent strain fields in 3d finite element analysis of welds. *ASME Journal of Pressure Vessel Technology*, 112(3):309–311, 1990.

[18] A. S. Oddy, J. A. Goldak, and J. M. J. McDill. numerical analysis of transformation plasticity in 3d finite element analysis of welds. *European journal of mechanics, A/solids*, 9:1–11, 1990.

[19] P. Michaleris and A. DeBiccari. Prediction of Welding Distortion. *Welding Journal*, 76(4):172–180, 1997.

[20] E. F. Rybicki and R. B. Stonesifer. Computation of Residual Stresses due to Multi-pass Welds in Piping Systems. *Journal of Pressure Vessel Technology*, 101:149–154, 1979.

[21] Y. Shim, Z. Feng, S. Lee, D.S. Kim, J. Jaeger, J. C. Paparitan, and C. L. Tsai. Determination of Residual Stress in Thick-Section Weldments. *Welding Journal*, 71:305s–312s, 1992.

[22] L. A. Bertram and A. R Ortega. Automated Thermomechanical Modeling of Welds Using Interface Elements for 3D Metal Deposition. In *Manuscript for Proceedings of ABAQUS User's Conference*, Oxford: Hibbit Karlsson and Sorensen Inc., 1991.

[23] S.B. Brown and H. Song. Implications of Three-Dimensional Numerical Simulations of Welding of Large Structures. *Welding Journal*, 71(2):55s–62s, 1992.

[24] P. Michaleris, L. Zhang, and P. Marugabandhu. Evaluation of applied plastic strain methods for welding distortion prediction. *Journal of Manufacturing Science and Engineering*, 129:1000–1010, 2007.

[25] Q. S. Nguyen and M. Rahimian. Mouvement permanent d'une fissure en milieu elastoplastique. *J. Mec. Appl.*, 5:95–120, 1981.

[26] Y. J. Chao and X. Qi. Thermal and thermo-mechanical modeling of friction stir welding of aluminum alloy 6061-t6. *Journal of Materials Processing and Manufacturing Science*, 7:215–233, 1998.

[27] P. Dong, F. Lu, J.K Hong, and Z Cao. Coupled thermomechanical analysis of friction stir welding process using simplified models. *Science and Technology of Welding and Joining*, 6:281–287, 2001.

[28] X. Deng and S. Xu. Solid mechanics simulation of friction stir welding process. *Trans. NAMRCSME*, 29:631–638, 2001.

[29] S. Xu, X. Deng, A. P. Raynolds, and T. U. Seidel. Finite element simulation of material . ow in friction stir welding. *Sci. Technol. Weld. Joining*, 6:191–193, 2001.

[30] C Chen and R Kovacevic. Thermomechanical modelling and force analysis of friction stir welding by the finite element method. *Journal of Mechanical Engineering Science*, 218:509–519, 2004.

[31] Paul A. Colegrove and Hugh R. Shercliffa. 3-dimensional cfd modelling of flow round a threaded friction stir welding tool profile. *Journal of Materials Processing Technology*, 169:320–327, 2005.

[32] Ajay Agrawal and Paul R. Dawson. A comparison of galerkin and streamline techniques for integration strains from an eulerian flow field. *International Journal for Numerical Methods In Engineering*, 21:853–881, 1985.

[33] Antoinette M. Maniatty and Yong Liu. Stabilized finite element method for viscoplastic flow: Formulation with state variable evolution. *International Journal for Numerical Methods In Engineering*, 56:185–209, 2003.

[34] X. Qin and P. Michaleris. Eulerian Elasto-Visco-Plastic Formulations for Residual Stress Prediction. *International Journal of Numerical Methods in Engineering*, 2008. In print.

[35] Erik G. Thomson and Szu-Wei Yu. A flow formulation for rate equilibrium equations. *International Journal for Numerical Methods in Engineering*, 30:1619–1632, 1990.

[36] J. Shanghvi and Pan. Michaleris. Thermo-elasto-plastic finite element analysis of quasi-state processes in eulerian reference frames. *International Journal for Numerical Methods in Engineering*, 53:1533–1556, 2002.

[37] Stuart B. Brown, Kwon H. Kim, and L.Anand. An internal variable constitutive model for hot working of metals. *International Journal of Plasticity*, 5:95–130, 1989.

[38] J.C. Heinrich and O.C. Zienkiewicz. Quadratic finite element schemes for two dimensional convective-transport problems. *International Journal for Numerical Methods in Engineering*, 11:1831–1844, 1977.

[39] A.N. Brooks and T.J.R. Hughes. Streamline upwind/petrovcgalerkin formulation for convection dominated flows with particular emphasis on the incompressible navierc-stokes equation. *Computer Methods in Applied Mechanics and Engineering*, 32:199–259, 1982.

[40] J. Donea, T. Belytschko, and P. Smolinski. A generalized galerkin method for steady state convectioncdiflusion problems with application to quadratic shape functions. *Computer Methods in Applied Mechanics and Engineering*, 48:25–43, 1985.

[41] T.J.R. Hughes, L.P. Franca, and G.M. Hulbert. A new finite element formulation for computational fluid dynamics: Viii. the galerkin/least-squares methods for advectivecdiflusive equations. *Computer Methods in Applied Mechanics and Engineering*, 73:173–189, 1989.

[42] X. Qin and P. Michaleris. Coupled Thermo-Elasto-Viscoplastic analysis of Friction Stir Welding. In *8th International Conference on Trends In Welding Research*, Pine Mountain, GA, June 2008. ASM.

[43] Guerdoux Simon and Fourment Lionel. Error estimation and accurate mapping based ale formulation for 3d simulation of friction stir welding. *Proceeding of the 9th International Conference on Numerical Methods in Industrial Forming Process*, 2007.

[44] A.M.Maniatty, P.R. Dawson, and G.G.Weber. An eulerian elasto-viscoplastic formulation for steady-state forming processes. *Int J. Mech. Sci.*, 33:361–377, 1991.

[45] P. R. DAWSON. On modeling of mechanical property changes during flat rolling of aluminum. *International journal of solids and structures*, 23:947–968, 1987.

[46] S. Kobayashi, S. Oh, and T. Altan. *Metal Forming and the Finite Element Method*. Oxford University Press, New York, 1989.

[47] A.M. Maniatty and M. Chen. Shape sensitivity analysis for steady metal forming processes. *International Journal for Numerical Methods in Engineering*, 39:1199–1217, 1996.

[48] Antoinette M. Maniatty and Yong Liu. Stabilized finite element method for vis-coplastic flow: formulation with state variable evolution. *International Journal for Numerical Methods in Engineering*, 56:185C–209, 2003.

[49] G G Weber, A M Lush, A Zavaliangos, and L Anand. An objective time-integration procedure for isotropic rate-independent and rate-dependent elastic-plastic constitutive equations. *International Journal of Plasticity*, 6:701–744, 1990.

[50] Gustavo Weber and Lallit Anand. Finite deformation constitutive equations and a time integration procedure for isotropic hyperelastic-viscoplastic solids. *Computer Methods in Applied Mechanics and Engineering*, 79:173–202, 1990.

[51] M.C. Boyce, G.G Weber, and D.M. Parks. On the kinematics of finite strain plasticity. *J. Mech. Phys. Solids*, 37:647–665, 1989.

[52] Ted Belytschko, Wing Kam Liu, and Brian Moran. *Nonlinear Finite Elements for Continua and Structures*. John Wiley and Sons, New York, fourth edition, 2000.

[53] Klaus-Jurgen Bathe. *Finite Element Procedures*. Prentice Hall, New Jersey, 1996.

[54] T.J.R. Hughes and A Brooks. A theoretical framework for petrov-galerkin methods with discontinuous weighting functions: application to the streamline-upwind procedure. *Finite Elements in Fluids*, 4:47–65, 1982.

[55] Sia Nemat-Nasser and Wei-Guo Guo. Thermomechanical response of hsla-65 steel plates: experiments and modeling. *Mechanics of Materials*, 37:379–405, 2003.

[56] A.M.Lush, G. Weber, and L.Anand. An implicit time-integration procedure for a set of internal variable constitutive equations for isotropic elasto-viscoplasticity. *International Journal of Plasticity*, 5:521–549, 1989.

[57] AN Fitch, CRA Catlow, and A Atkinson. Measurement of stress in nickel oxide layers by diffraction of synchrotron radiation. *Journal of Materials Science*, 26:2300–2304, 1991.

[58] PJ Webster. Strain scanning using x-rays and neutrons. *Materials Science Forum*, 228C231:191C200, 1996.

[59] Rosenthal D. and Norton J. T. A method for measuring triaxial residual stresses in plates. *Welding Journal*, 24:295–307, 1945.

[60] Determining residual stresses by the Hole drilling Strain Gage Method. ASTM Standard E837.

[61] E. F. Rybicki, D. W. Schmueser, R. B. Stonesifer, J. J. Groom, and H. W. Mishler. A Finite-Element Model for Residual Stresses and Deflections in Girth-Butt Welded Pipes. *Journal of Pressure Vessel Technology*, 100:256–262, 1978.

[62] J. Goldak, A. Chakravarti, and M. Bibby. A New Finite Element Model for Welding Heat Sources. *Metallurgical Transactions B*, 15B:299–305, 1984.

[63] J. Wang and H. Murakawa. A 3-d fem analysis of buckling distortion during welding in thin plate. In *5th International Conference in Trends in Welding Research*, Pine Mountain, GA, 1998.

[64] C.L. Tsai, S.C. Park, and W.T. Cheng. Welding Distortion of a Thin-Plate Panel Structure. *A.W.S. Welding Journal, Research Supplement*, 78:156s–165s, 1999.

[65] L. Fourment1 and S. Guerdoux. 3D numerical simulation of the three stages of Friction Stir Welding based on friction parameters calibration. *International Journal of Material Forming*, 1:1, 2008.

[66] J. Y. SHANGHVI and P. MICHALERIS. Thermo-elasto-plastic finite element analysis of quasi-state processes in eulerian reference frames. *International journal for numerical methods in engineering*, 53:1533–1556, 2002.

[67] J. C. Simo and R. L. Taylor. Consistent Tangent Operators for Rate-Independent Elasto-Plasticity. *Computer Methods in Applied Mechanics and Engineering*, 48:101–118, 1985.

[68] J. Lubliner. *Plasticity Theory*. Macmillan Publishing Company, New York, 1st edition, 1990.

[69] D. Balagangadhar, G.A. Dorai, and D.A. Tortorelli. A displacement-based eulerian steady-state formulation suitable for thermo-elasto-plastic material models. *International Journal of Solids and Structures*, 36(16):2397–2416, 1999.

[70] J. Goldak M. GU and E. Hughes. Steady State Thermal Analysis of Welds with Filler Metal Addition. *Canadian Metallurgical Quarterly*, 32(1):49–55, 1993.

[71] E. Ohmura, Y. Takamachi, and K. Inoue. Theoretical analysis of laser transformation hardening process of hypoeutectoid steel based on kinetics. *Trans. Japan Soc. of Mech. Eng. (Ser. A)*, 56:1496–1503, 1990.

[72] S. Rajadhyaksha and P. Michaleris. Optimization of Thermal Processes using an Eulerian Formulation and Application in Laser Hardening. *International Journal for Numerical Methods in Engineering*, 47:1807–1823, 2000.

[73] X. Qin and P. Michaleris. Elasto-Visco-Plastic Analysis of Welding Residual Stress. 2008. In preparation.

[74] Simon Guerdoux and Lionel Fourment. Error estimation and accurate mapping based ale formulation for 3d simulation of friction stir welding. *AIP Conference Proceedings*, 908(1):185–190, 2007.

[75] Vlado A Lubarda. Constitutive theories based on the multiplicative decomposition of deformation gradient: Thermoelasticity, elastoplasticity, and biomechanics. *Applied Mechanics Reviews*, 57:95–108, 2004.

[76] Xiaoliang Qin and Pan. Michaleris. Eulerian elasto-visco-plastic formulations for residual stress prediction. *INTERNATIONAL JOURNAL FOR NUMERICAL METHODS IN ENGINEERING*, 2008.

[77] Z. Feng, J.E. Gould, and T.J. Lienert. A heat flow model for friction stir welding of steel. *Proceedings of Hot Deformation of Aluminum Alloys*, pages 149 –158, 1998.

[78] R. Nandan, G.G. Roy, T.J. Linert, and T. Debroy. Three-dimensional heat and material flow during friction stir welding of mild steel. *Acta Materialia*, 55:883–895, 2007.

[79] Reynolds A.P., Tang W., Gnaupel-Herold T., and Prask H. Structure, properties, and residual stress of 304l stainless steel friction stir welds. *Scripta Materialia*, 48:1289–1294, 2003.

Vita

Xiaoliang Qin received his BE degree in Structural Mechanics from the Department of Mechanics and Engineering Science at Beijing University in June 2000. In Aug 2004, he was enrolled in the graduate program in Mechanical Engineering at the Pennsylvania State University and began to pursue his PhD degree. His research interests include solid mechanics, thermal processing, nonlinear finite element analysis, numeric methods, and high performance parallel and distributed computing.